Nickel Oxidation in Solid Oxide Cells:
Modeling and Simulation of Multi-Phase
Electrochemistry and Multi-Scale Transport

Von der Fakultät Energie-, Verfahrens- und Biotechnik der Universität Stuttgart
zur Erlangung der Würde eines Doktor-Ingenieurs (Dr.-Ing.)
genehmigte Abhandlung

Vorgelegt von

Jonathan Philipp Neidhardt

aus Frankfurt am Main

Hauptberichter: Prof. Dr. rer. nat. Wolfgang G. Bessler
Mitberichter: Prof. Dr. rer. nat. K. Andreas Friedrich

Tag der mündlichen Prüfung: 15.11.2013

Institut für Thermodynamik und Wärmetechnik
der Universität Stuttgart
2013

Wir wissen jedoch, dass unsere Sehnsucht nach Energie uns dazu verführt hat, gefährliche Risiken in Kauf zu nehmen. [...] Ein sich veränderndes Klima, ein gescheitertes Wagnis, wie der Bau von Atomreaktoren in küstennahen Verwerfungszonen, dies sind Zeichen dafür, dass der Weg einer ganzen Welt woanders hin führt.

[Alan Weisman, January 2012]

„Die sichere, klimaverträgliche, nachhaltige und kostengünstige Bereitstellung von Energie ist eine der größten Herausforderungen des 21. Jahrhunderts für eine weiterhin wachsende Menschheit.''

[German Academy of Sciences Leopoldina, Energiepolitische und forschungspolitische Empfehlungen nach den Ereignissen in Fukushima, June 2011]

"Change doesn't come from the sky. It comes from human action"

[Tenzin Gyatso, 14th Dalai Lama]

TABLE OF CONTENTS

LIST OF ABBREVIATIONS

1-2-3-D	One-, two-, three-dimensional
AEC	Alkaline electrolysis cell
ASC	Anode supported cell
ASR	Area specific resistance
ASCII	American Standard Code for Information Interchange
CFD	Computational fluid dynamics
CGO	Gadolinia doped ceria
CL	Catalyst layer
CTR	Charge-transfer reaction
CV	Control volume
DAE	Differential algebraic equation
DENIS	Detailed electrochemistry and numerical impedance simulation
DLR	Deutsches Zentrum für Luft- und Raumfahrt e.V. (German Aerospace Center)
DOO	Degree of oxidation
EIS	Electrical impedance spectroscopy
EN	Electrical charge neutrality
ESC	Electrolyte supported cell
FDM	Finite difference method
FEM	Finite elements method
FU	Fuel utilization
FVM	Finite volume method
GDC	Gadolinia doped ceria
HOR	Hydrogen oxidation reaction
LFSR	Local fuel-to-steam ratio
LSCF	Lanthanum strontium cobalt ferrite
LSM	Lanthanum strontium manganite

MEA	Membrane-electrode assembly
Ni	Nickel
NiO	Nickel oxide
OCV	Open circuit voltage
ODE	Ordinary differential equation
ORR	Oxygen reduction reaction
PDE	Partial differential equation
PEFC	Polymer electrolyte fuel cell
POI	Point of interest
SoC	State of charge
SOC	Solid oxide cell
SOEC	Solid oxide electrolysis cell
SOFC	Solid oxide fuel cell
TPB	Triple-phase boundary
YSZ	Yttria stabilized zirconia

LIST OF SYMBOLS

Symbol	Unit	Meaning
a_i	$-$	Activity of species i
A_m^V	$m^2 \cdot m^{-3}$	Volume-specific surface area corresponding to reaction m
A_0^V	$m^2 \cdot m^{-3}$	Initial volume-specific surface area
A^{cha}	m^2	Channel cross-sectional area
A_{dl}	$m^2 \cdot m^{-3}$	Volume-specific contact area between electrode and electrolyte
B	m^2	Permeability of the porous electrode
c_i	$mol \cdot m^{-3}$	Concentration of species i in a bulk phase
c^g	$mol \cdot m^{-3}$	Total gas-phase concentration
C_{dl}	$F \cdot m^{-3}$	Volume-specific double layer capacitance
D_i, D_i^{eff}	$m^2 \cdot s^{-1}$	(Effective) transport coefficient of species i
E_{cell}	V	Cell voltage
E_{local}	V	Local cell voltage
E_f^{act}	$J \cdot mol^{-1}$	Activation energy of forward and reverse reactions
E_{rev}	V	Reversible cell voltage
F	$C \cdot mol^{-1}$	Faraday's constant
G	S	Electrical conductance
G_{cv}	m^3	Control volume
h_i	$J \cdot mol^{-1}$	Molar enthalpy of species i
i	$-$	Index of species and phases
i	$A \cdot m^{-3}$	Current density
i_{dl}	$A \cdot m^{-3}$	Current density due to electrical double layer
i_F	$A \cdot m^{-3}$	Faradaic current density
j_i^{diff}	$kg \cdot m^{-2} \cdot s^{-1}$	Mass diffusion flux of species i
J_i	$mol \cdot m^{-2} \cdot s^{-1}$	Flux of species i

J_i^{flow}	$\text{mol·m}^{-2}\text{·s}^{-1}$	Darcy flux of species i
k_f, k_r	$\text{m}^x\text{·kmol}^{-y}\text{·s}^{-z}$	Forward and backward rate constant (x, y and z depend on the order of the corresponding reaction)
k_0^{f}	$\text{m}^x\text{·kmol}^{-y}\text{·s}^{-z}$	Preexponential factor in Arrhenius equation
$k_{\text{s,cap}}$	s^{-1}	Rate constant in capacitive Ni coarsening model
l_m^{V}	m·m^{-3}	Volume-specific three-phase boundary length of reaction m
l_0^{V}	m·m^{-3}	Initial volume-specific three-phase boundary length
L	m	Geometrical length of the electrode
m	–	Index of chemical reactions and interfaces
M_i	kg·mol^{-1}	Mean molar mass of phase i
$\mathbf{n}$	–	Normal vector
n_i	mol	Absolute amount of species i
p	Pa	Pressure
$P_{\text{chem}}^{\text{cha}}$	m	Electrochemically active channel perimeter
$P_{\text{h}}^{\text{cha}}$	m	Hydrodynamic channel perimeter
r	m	Particle radius
R	$\text{J·K}^{-1}\text{·mol}^{-1}$	Ideal gas constant
R	Ω	Ohmic resistance
R_i	$\text{mol·m}^{-3}\text{·s}^{-1}$	Net rate of production of phase i
s_i	$\text{J·K}^{-1}\text{·mol}^{-1}$	Molar entropy of species i
$\dot{s}_i^{cha}$	$\text{mol·m}^{-2}\text{·s}^{-1}$	Exchange rate of species i between electrode and channel
$\dot{s}_{i,m}$	$\text{mol·m}^{-2}\text{·s}^{-1}$ $\text{mol·m}^{-1}\text{·s}^{-1}$	Chemical production rate of species i in reaction m (per m^{-2} for two-phase reactions and m^{-1} for three-phase reactions)
S_{g}	–	Set of all gas-phase species for Stefan-Maxwell diffusion
t	s	Time
T	K	Temperature
v	m·s^{-1}	Channel flow velocity
V	V	Voltage
W	–	Weight function
x	m	Spatial position in dimension of channel length
X_i	–	Mole fraction of species i
y	m	Spatial position through electrode thickness
Y_i	–	Mass fraction of species i
z	–	Number of electrons transferred in charge-transfer step

12

α	–	Symmetry factor of charge transfer reaction
α_e	–	Evaporation coefficient
β	–	Temperature exponent in Arrhenius equation
δ	m	Film thickness
ΔG	J·mol^{-1}	Gibbs free energy
ΔH	J·mol^{-1}	Reaction enthalpy
ΔS	J·K^{-1}·mol^{-1}	Reaction entropy
ε_i	–	Volume fraction of phase i
ε_0	–	Initial volume fraction
ζ_j	–	Fraction of grid compartment j
η	V	Overpotential
η_act	V	Activation overpotential
η_ohm	V	Ohmic overpotential
η_conc	V	Concentration overpotential
λ	m	Average length of fluid path
μ_g	kg·m^{-1}·s^{-1}	Gas-phase viscosity
μ_i	J·mol^{-1}	Chemical potential of species i
ν_i	–	Stoichiometric coefficient of species i
ξ	–	Fit parameter describing the microstructure of an electrode
ρ	kg·m^{-3}	Density
σ	S·m^{-3}	Solid-phase ionic or electronic conductivity
τ	–	Tortuosity of a porous phase
τ_w	kg·m^{-1}·s^{-2}	Shear-stress factor
ϕ	V	Electric potential

ABSTRACT

Due to their fuel flexibility and high efficiency solid oxide cells (SOC) are a promising technology for energy conversion in a future sustainable energy scenario. However, durability is a major issue for reliable operation of SOC systems. This thesis gives a detailed description of nickel oxide (NiO) formation in the electrodes of SOCs. It is based on the development of a computational modeling framework which incorporates multi-phase electrochemistry as well as multi-scale transport processes. A continuum approach is used for describing the two-dimensional spatiotemporal evolution of gaseous, liquid and solid phases. Formation of NiO is modeled via thermochemical and electrochemical reaction pathways. The feedback between nickel oxidation and cell performance is modeled by taking into account a loss in kinetic performance (via reducing three-phase boundary length) and a reduction in gas-phase diffusivity (via porosity decrease upon solid volume expansion). Irreversible degradation of cell performance is described by loss of active nickel volume. On the microscale, NiO formation is modeled as a growing film layer on top of the nickel phase. Here, the oxidation rate is controlled by transport of species across the film. Simulations allow the quantification of nickel oxide formation over time and its influence on cell performance. Analysis allows, for example, the prediction of 'safe' operating conditions to avoid nickel oxide formation. In addition to providing insight in interpreting experimental observations, this work provides a quantitative predictive capability for improving electrode design and controlling operating conditions of solid oxide cells.

ZUSAMMENFASSUNG

Festoxid-Zellen (solid oxide cell, SOC) sind eine vielversprechende Technologie im Szenario einer nachhaltigen Energieversorgung, da sie sowohl die hocheffiziente Umwandlung von elektrischer in chemische Energie (solid oxide electrolysis cell, SOEC), als auch von chemischer in elektrische Energie (solid oxide fuel cell, SOFC) ermöglichen. Ein wesentliches Hindernis für die Markteinführung stellt jedoch die begrenzte Alterungsbeständigkeit der Zellen dar. Ziel der vorliegenden Dissertation ist die detaillierte Beschreibung von Nickeloxidbildung in den Elektroden von SOCs. Grundlage der Arbeit ist die Entwicklung eines mathematischen Modellierungsgerüstes, das sowohl die numerische Simulation von Multi-phasen-Elektrochemie als auch von Multi-Skalen-Transportprozessen ermöglicht. Die (elektro)-chemischen Wechselwirkungen zwischen beliebigen gasförmigen, flüssigen und festen Phasen, sowie die Rückkopplung auf die Mikrostruktur der Zelle, werden mittels eines Kontinuumansatzes in 2D beschrieben. Die Bildung von Nickeloxid (NiO) ist über einen thermochemischen und einen elektrochemischen Reaktionspfad implementiert. Das Modell berücksichtigt den Einfluss von NiO auf die Zellleistung durch eine Verringerung der Reaktionskinetik (Verkürzung der Dreiphasengrenze) und eine Verlangsamung des Gastransportes durch die poröse Elektrode (Reduktion der Porosität). Irreversible Effekte auf die Leistung der Zelle werden durch eine Reduktion des aktiven Nickelvolumens modelliert. Ein zusätzliches Mikro-Modell ermöglicht die Beschreibung von NiO-Bildung als wachsende Oxidschicht an der Grenzfläche zu metallischem Nickel. Dabei wird die Oxidationsrate durch den Transport von Spezies durch die wachsende Schicht limitiert. Die Simulationsergebnisse ermöglichen die Quantifizierung von Nickeloxidbildung über der Zeit und seine Auswirkungen auf die Leistung der Zelle. Dies ermöglicht, unter anderem, die Vorhersage von sicheren Betriebsbedingungen bezüglich der Bildung von NiO. Zusätzlich zum erweiterten Verständnis von experimentellen Messungen, ermöglicht die vorliegende Arbeit quantitative Vorhersagen zur Verbesserung des Elektrodendesigns und der Betriebsführung von Festoxid-Zellen.

1 INTRODUCTION

In the light of dwindling fossil resources switching to alternative ways of electrical energy generation is a vital requirement. In recent years technologies for harvesting renewable energy have made a substantial step forward. In 2011 already 20 % of Germany's electrical energy demand was produced by renewable sources, which correlates to an energy of 123 TWh [1]. The largest contributions are from wind (8 %), biomass (5 %), photovoltaics (3 %) and hydropower (3 %). The governmental plan foresees an increase up to 80 % by the year 2050. A study by Henning and Palzer [2] shows that even a total of 100 % of heat and power in Germany could come from renewable sources, with costs that do not exceed the price for today's fossil based economy.

The big challenge which arises in switching to 100 % renewable energy is storage of excessive energy in times of high energy production (sunny and windy) and its supply to the grid in times of low production (dark and calm). Solid oxide cells (SOC) are a promising technology which can contribute to achieve these requirements. In electrolysis mode (SOEC) the cells can convert excessive electrical energy from renewable sources, like wind turbines, into fuels (power-to-gas technology). For example, hydrogen ($2\ H_2O$ + energy $\rightleftarrows$ $2\ H_2 + O_2$) or syngas ($H_2O + CO_2$ + energy $\rightleftarrows$ $H_2 + CO + O_2$) can be produced and either stored or, alternatively, fed into the gas grid. In fuel cell mode the reverse processes take place, providing electrical energy. Both technologies are highly efficient with more than 50% fuel-to-electricity efficiency for SOFC [3] and even up to 95 % for high temperature steam electrolysis in SOEC [4]. Figure 1 shows a possible energy scenario for an economy based on energy provided by the sun, developed by Kreuter and Hofmann [5].

However, durability is a major issue for reliable operation of SOC systems. The aim for market access is securing a minimum lifetime of 40,000 hours [6]. But, current SOC components

are not yet suitable for long-term operation. Supported by the high operating temperatures between 600 and 1000 °C, a variety of corrosive processes is causing permanent performance degradation. Additionally, transient operation like thermal cycling can lead to total failure of the cell. Although the phenomena of degradation are widely known, the exact mechanisms are still controversial and not yet studied in sufficient depth. Their experimental investigation is difficult. Because measurement data from inside a closed high-temperature system is difficult to obtain, typically only indirect techniques like electrochemical impedance spectroscopy (EIS) and post-mortem analysis are used to draw conclusions on degradation.

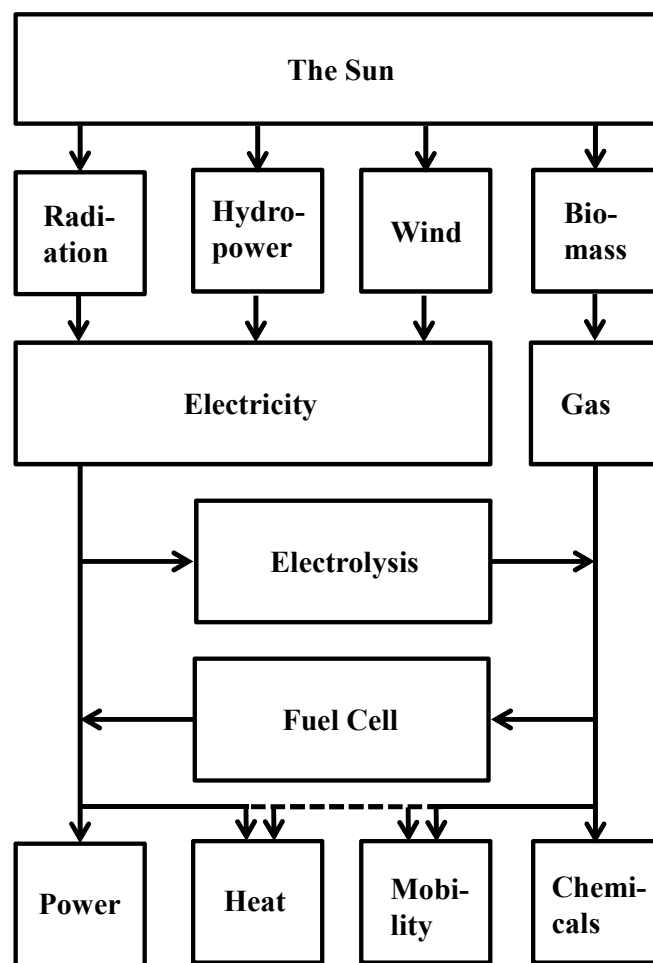Figure 1. The sustainable energy scenario. Modified from [5].

Aim of the present thesis is the development and application of mathematical models that will enable SOC life time prediction using computer simulations. Namely, an existing in-house modeling framework which describes multi-scale transport processes and the complex electrochemistry in electrochemical cells [7] is extended for handling reactions in-between multi-

ple solid, liquid and gaseous phases, including phase formation and dissolution processes [8]. The framework is applied for the detailed analysis of nickel oxide (NiO) formation in solid oxide fuel and electrolyzer cells. This includes the prediction of safe operation conditions [9] and simulation of irreversible degradation, as well as detailed description of a growing NiO film on nano/micro scale [10]. The model provides a quantitative predictive capability for improving electrode design and controlling operating conditions.
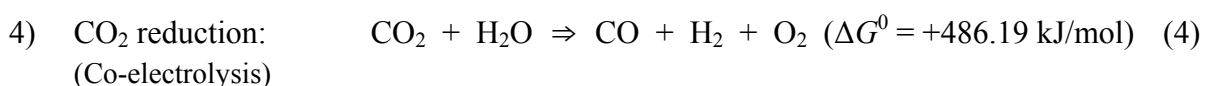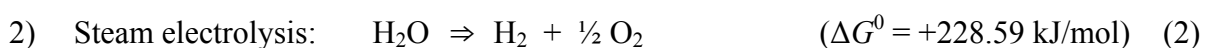
The work is structured as follows. Fundamental knowledge on the working principle of SOCs, including thermodynamics, electrochemistry, transport phenomena and degradation mechanisms occurring at the fuel electrode is given in the *Background* chapter (Chapter 2). It is complemented by a section on numerical modeling. The following chapter describes the developed *Multi-phase modeling and simulation framework* (Chapter 3), which is the basis for all simulations of nickel oxide formation. It is concluded by the presentation of three exemplary models which were used for validation and, simultaneously, for demonstration of the framework's capability to describe secondary phase formation in other types of electrochemical cells. Central part of this work is the chapter on *Nickel oxidation in SOFC and SOEC electrodes* (Chapter 4). It begins with a thermodynamic description of the oxidation of nickel by oxygen or steam from the gas phase (thermochemical pathway) or by oxygen ions from the electrolyte phase (electrochemical pathway), followed by a section on model parameterization based on experimental data from literature. A detailed description of NiO formation in SOFC and SOEC due to different operation conditions is given. This includes the prediction of a hysteresis in the polarization curve caused by NiO formation, a temporally and spatially resolved process analysis, as well as the prediction of safe operation points under local and global aspects. Additionally, the model capability to predict irreversible degradation phenomena is shown by exemplary simulations and a summary of possible modeling errors and limitations is given. For a more detailed analysis the model was enhanced by a description of the growth of a NiO film on micro/nano-scale, which is presented in the chapter *Detailed modeling of nickel oxide film growth* (Chapter 5). The chapter includes a description of the film model, model parameterization by literature data and the presentation and discussion of simulation results. Finally, the chapter *Summary and outlook* (Chapter 6) gives a summary of this thesis, together with suggestions for further research.

2 BACKGROUND

2.1 The solid oxide cell

The term solid oxide cell (SOC) indicates an electrochemical cell for energy conversion which is based on a charge separator made of solid ceramic (oxide) material [11, 12]. Two modes of SOC operation can be distinguished depending on the direction of energy conversion: in fuel cell mode chemical energy is transferred to electrical energy (solid oxide fuel cell, SOFC) and in electrolysis mode the reverse process can convert electrical energy into chemical energy, like synthetic fuels (solid oxide electrolysis cell, SOEC). The working principle is illustrated in Figure 2: Major components of the cell are two porous electrodes and the solid electrolyte. Reactants are typically gaseous and fed to the cell by flow channels. At the cathode side oxygen containing reactants are reduced, which releases oxygen ions (O^{2-}). They migrate through the ionic conducting electrolyte and act as oxidant for the fuel gas at the anode. Electrons cannot pass the electrolyte. They are conducted through an external circuit which is connected to a load or source.

The amount of released or consumed energy is given by the thermodynamics of the respective reactions. The four main reaction mechanisms in global kinetic formulation are [11−14]:

1) Hydrogen oxidation: $H_2 + \frac{1}{2} O_2 \Rightarrow H_2O$ $\quad\quad\quad\quad\quad (\Delta G^0 = -228.59 \text{ kJ/mol})$ (1)

2) Steam electrolysis: $H_2O \Rightarrow H_2 + \frac{1}{2} O_2$ $\quad\quad\quad\quad\quad (\Delta G^0 = +228.59 \text{ kJ/mol})$ (2)

3) Methane oxidation: $CH_4 + 2 O_2 \Rightarrow 2 H_2O + CO_2$ $\quad (\Delta G^0 = -800.68 \text{ kJ/mol})$ (3)

4) CO_2 reduction: $CO_2 + H_2O \Rightarrow CO + H_2 + O_2$ $(\Delta G^0 = +486.19 \text{ kJ/mol})$ (4)
   (Co-electrolysis)

Here, ΔG^0 is the standard-state Gibbs free energy of the reactions (25 °C, 1 bar). Negative values indicate a net release of electric energy. In electrolysis mode the required Gibbs energy has to be applied by an external source.
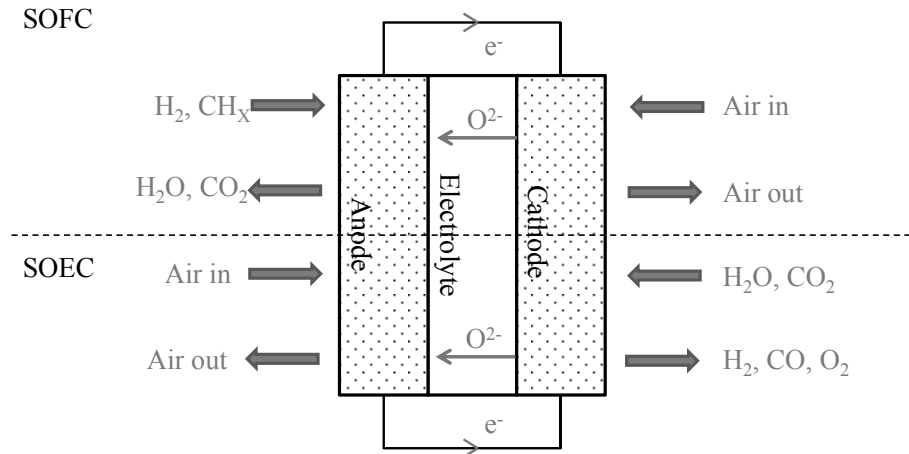
Figure 2. Cross-section of a solid oxide cell illustrating the differences of operation in fuel cell mode (SOFC) and in electrolysis mode (SOEC).

Materials for SOC components have to be chosen with respect to three main requirements: conductivity (ionic and electronic), catalytic activity (for the respective reaction) and structural stability (mechanical and chemical) [15]. Table 1 gives an overview of the most common materials and their specific properties.

Table 1. Common materials for SOC components [16–18].

Material	Name	Properties	Component
Ni	Nickel	Electronic conductor, catalyst for H_2 oxidation reaction (HOR) and for hydrocarbon reforming	Fuel electrode
$ZrO_2(Y_2O_3)$	Yttria stabilized zirconia (YSZ)	Ionic conductor, high mechanical and chemical stability	Fuel electrode, electrolyte
CeO_2	Gadolinia doped ceria (GDC or CGO)	Mixed ionic and electronic conductor, catalyst for CH_4 oxidation	Electrolyte, diffusion barrier in oxygen electrode, fuel electrode of SOFC
$LaMnO_3$	Lanthanum strontium manganite (LSM)	Ionic conductor, catalyst for oxygen reduction reaction (ORR)	Oxygen electrode
$LaSrCoFeO_3$	Lanthanum strontium cobalt ferrite (LSCF)	Mixed ionic and electronic conductor, catalyst for oxygen reduction reaction	Oxygen electrode

Crucial for SOC performance is a high ionic conductivity of the electrolyte material. With current electrolytes, like YSZ, a reasonable conductivity can only be achieved for a temperature ≥ 800 °C. Therefore typical operation temperatures of solid oxide cells vary between 800

and 1000 °C [11]. In comparison to competitive systems like proton-exchange membrane fuel cells (PEFC) or alkaline electrolysis cells (AEC), which run at temperatures between 50 and 220 °C, high temperature operation brings several advantages:

1) With increasing temperature the kinetics of chemical reactions increase, which decreases polarization losses and increases efficiency.

   a. For SOFC the chemical to electrical energy conversion efficiency is 45 to 65 %, which is about twice that of an internal combustion engine. In combined use of power and heat, efficiency is increased further up to more than 85 % [19].

   b. For SOEC an electricity to H_2 efficiency of more than 95 % can be achieved [4].

2) At higher operation temperature less electrical energy is needed for electrolysis, because a substantial part of energy demanded by the endothermic reaction is provided thermally. Especially if excess heat from external sources, e.g., from industrial processes, is used system efficiency can be further increased [20].

3) Due to internal reforming SOFC can be operated on a broad variety of fuels including natural gas and gases obtained from biomass or municipal waste [21].

Unfortunately the drawbacks of high operation temperature cannot be neglected:

1) System start-up and shutdown can take up to several hours, which is a challenge for mobile applications, like portable power and transportation.

2) Due to thermally insulating housing, SOC systems are typically big and have higher investment costs than low-temperature cells.

3) High temperatures cause a high stress on the used materials. Especially regarding long-term operation material degradation is a major issue currently impeding the market entry of SOFC and SOEC systems [4, 6].

Details about thermodynamics, the fundamental processes inside the electrodes, and degradation mechanisms will be presented in the following sections.

2.2   *Predicting the performance of an SOC*

The performance of an electrochemical system is measured by its cell voltage (E_{cell}) versus current density (*i*) characteristics. In cell operation current is typically given as external input (demand of a load or output of a source), while the voltage is a result of the cell response on that current. Thus mathematically formulated we are looking for a function

$$E_{cell} = f(i)$$ (5)

.

Three main mechanisms are governing the voltage under cell operation: (1) thermodynamics, (2) electrochemistry and (3) transport phenomena. Fundamental aspects of each mechanism, with focus on prediction of the performance of SOCs, will be summarized in the following subsections. For more detailed derivations please refer to common text books [11, 22, 23].

2.2.1   *Thermodynamics*

Thermodynamics describes the conversion of energy from one form into another. Basis for many thermodynamic considerations is the Gibbs-Helmholtz equation,

$$\Delta G = \Delta H - T\Delta S$$ (6)

,

where ΔG is the Gibbs free energy, ΔH the reaction enthalpy and ΔS the entropy of the reaction. Regarding solid oxide cells thermodynamics can be applied, for example, to predict the direction of (electro-)chemical reactions, as well as the energy and heat produced or consumed by these reactions. While ΔH describes the maximum amount of total energy that can be gained from a system, ΔG can be associated with the maximum electrical energy and ΔS with the heat energy which is released by an electrochemical reaction.

Under presumption that the total energy released by the reaction is transformed into electrical energy (ideal cell), thermodynamics can be used to calculate the voltage of an electrochemical cell at open circuit (OCV, $i = 0$),

$$E_{rev}^0 = -\frac{\Delta G^0}{zF}$$ (7)

,

where E_{rev}^0 is the standard-state (STP) reversible voltage, *z* the number of electrons transferred and *F* Faraday´s constant. If more than one reactive species is present at each electrode, Eq. 7 has to be extended by an additional term, which leads to the Nernst equation [11],

$$E_{\text{rev}} = -\frac{\Delta G^0}{zF} - \frac{RT}{zF} \ln \frac{\prod a_{\text{products}}^{v_i}}{\prod a_{\text{reactants}}^{v_i}} \qquad (8)$$

where a is the activity and v_i the stoichiometric coefficient of each species participating in the reaction. The activity depends on the type of each species. For gas-phase and dissolved species it is equal to partial pressure or concentration (c_i/c_0 or p_i/p_0), for surface adsorbates it equal to coverage (θ), and for solid bulk phases it is unity. By replacing the standard-state Gibbs energy ΔG by its value corresponding to different temperatures, the OCV for arbitrary operation conditions can be predicted.

Requirement for thermodynamic calculations is the knowledge of thermodynamic data, that is enthalpies and entropies for all species involved. An extensive database is provided, e.g., by McBride and co-workers [24]. A collection of data for the most prominent species used in SOC application is summarized in [11].

2.2.2 Electrochemistry

The current produced or consumed by an SOC depends on the rate of the proceeding electrochemical reaction(s). For an electrochemical reaction with a transfer of z electrons the resulting Faradaic current density is,

$$i_{\text{F}} = zF\dot{s} \qquad (9)$$

where $\dot{s}$ is the rate of the electrochemical reaction. According to mass-action kinetics [25] the net production rate of a species i is given by,

$$\dot{s}_i = v_i \left(k_{\text{f}} \prod_m a_j^{v_j'} - k_{\text{r}} \prod_m a_j^{v_j''} \right) \qquad (10)$$

where k_f and k_r are the forward and backward rate constants, v_i denotes the stoichiometric coefficient of species i, a_j the activities, and v' and v'' represent the positive stoichiometric coefficients for all reactants of the forward and backward reaction, respectively.

The forward rate constant is given by a modified Arrhenius expression [8],

$$k_{\text{f}} = k_0^{\text{f}} T^\beta \exp\left(-\frac{E_{\text{f}}^{\text{act}}}{RT} \right) \exp\left(-\frac{\alpha zF}{RT} \Delta\phi \right) \qquad (11)$$

where k_0^{f} is the pre-exponential factor, T the temperature, $E_{\text{f}}^{\text{act}}$ the activation energy, β a temperature exponent, and R the ideal gas constant. In case of a charge-transfer reaction, the last

exponential term represents the influence of the electric potential difference $\Delta\phi$, with a net transfer of z electrons, the Faraday's constant F and a symmetry factor α. For thermochemical reactions (no charges involved, therefore $z = 0$) Eq. 11 reduces to the standard Arrhenius equation [25]. Note, that the combination of Eqs. 9−11 allows for deviation of the well-known Butler-Volmer equation [22].

The reverse rate constant follows from thermodynamic consistency using thermodynamic data,

$$\frac{k_\text{f}}{k_\text{r}} = \exp\left(-\frac{\Delta G}{RT}\right) \quad . \tag{12}$$

In contrast to the globally formulated reactions given in the previous section (Eqs. 1−4) the actual reactions taking place during SOC operation are complex. Work in the recent years has revealed multiple elementary reaction steps which are involved [26–29]. Exemplarily the main reaction mechanism occurring at the anode of an SOFC will be presented in the following.

At the anode of hydrogen fuelled SOFCs the gaseous H_2 reacts with oxygen ions (O^{2-}) to steam, releasing two free electrons,

$$H_2 + O^{2-} \rightleftarrows H_2O + 2\,e^- \quad . \tag{13}$$
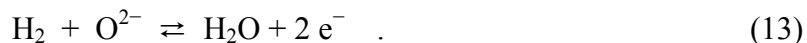
A more detailed reaction pathway can be developed by analysis of the involved surface reactions (elementary kinetic approach). This includes surface-surface-reactions (Langmuir-Hinshelwood type mechanism), charge transfer, adsorption and desorption, as well as bulk-surface reactions (Eley-Rideal type mechanisms) [30]. Taking into account these reactions we can derive a complete mechanism consisting of nine elementary reaction steps, which is shown in Figure 3 [26, 27]. Kinetics of the elementary reactions can be determined either by experiments like temperature-programmed desorption (TPD) [28] or by mechanistic calculations based on DFT (density-functional theory) [31, 32].

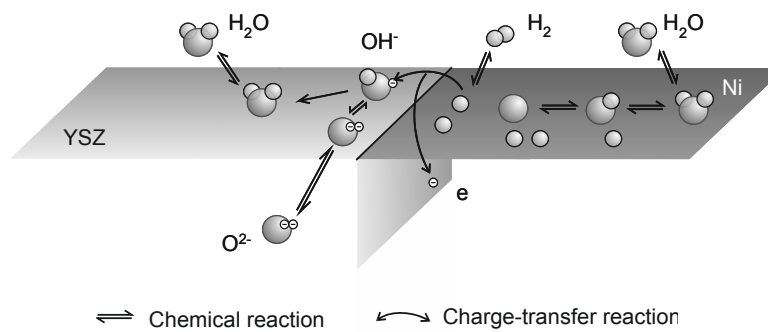| Interface	Reaction
Nickel surface	$H_2 + (Ni) + (Ni) \rightleftarrows H(Ni) + H(Ni)$
	$H_2O + (Ni) \rightleftarrows H_2O(Ni)$
	$H(Ni) + O(Ni) \rightleftarrows OH(Ni) + (Ni)$
	$H(Ni) + OH(Ni) \rightleftarrows H_2O(Ni) + (Ni)$
	$H_2O(Ni) + O(Ni) \rightleftarrows OH(Ni) + OH(Ni)$
YSZ surface	$(YSZ) + O^{2-}_{YSZ} \rightleftarrows O^{2-}(YSZ) + V_{YSZ}$
	$H_2O + (YSZ) \rightleftarrows H_2O(YSZ)$
	$H_2O(YSZ) + O^{2-}(YSZ) \rightleftarrows OH^-(YSZ) + OH^-(YSZ)$
Three-phase boundary	$H(Ni) + OH^-(YSZ) \rightleftarrows H_2O(YSZ) + (Ni) + e^-$

Figure 3. Elementary reaction steps at the three-phase boundary (TPB) of a hydrogen fueled SOFC anode [27].

2.2.3 Transport phenomena

In an SOC three main regimes of transport can be distinguished, as illustrated in Figure 4: (1) gas transport inside the porous electrodes, (2) transport of gaseous species to and away from the electrodes and (3) charge transport through the electronic and ionic conducting phases. On atomic scale additional transport processes can be relevant. This includes, e.g., diffusion of species sticking to a surface or the diffusion of species inside a solid bulk material.

(1) The electrodes of solid oxide cells are usually porous structures with average pore sizes between 5 μm (supporting layer) and 100 nm (active layer). Here, the main transport mechanism is diffusion driven by concentration gradients. For a binary mixture the molar flux J of a species can be described by Fickian Diffusion,

$$J_i = -D_i \frac{\partial c_i}{\partial x} \quad , \tag{14}$$

where D_i is the diffusion coefficient and c_i the concentration of a species i. For a gas phase

containing more than two species the diffusion is more complex, because the flux depends on the concentration gradient of all species [23]. In this case the Stefan-Maxwell equations for multi-component mixtures have to be applied,

$$\frac{\partial(c^g X_i)}{\partial x} = \sum_{j \in S_g} \frac{X_i J_j - X_j J_i}{D_{ij}^{\text{eff}}} \quad , \tag{15}$$

where c^g is the total gas-phase concentration, S_g is the set of all gas-phase species, X specifies the molar fraction of a species and D^{eff} is the effective diffusion coefficient.
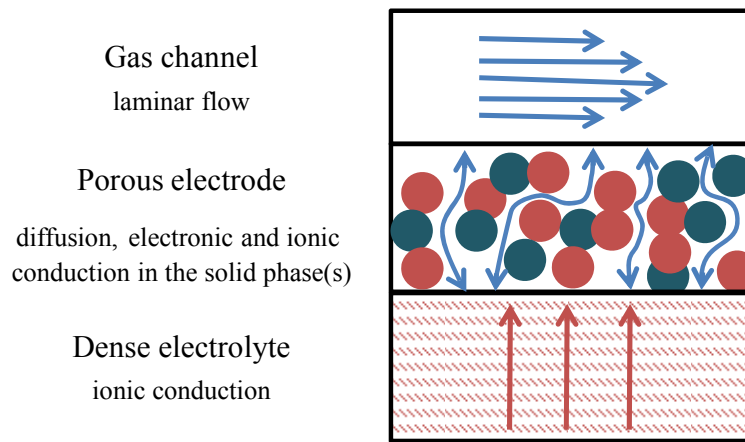
Figure 4. Schematic of the different transport mechanisms within a solid oxide cell.

A common method for modeling transport in porous media is the homogenization approach [33]. It is applied to describe a complex geometrical structure by means of effective transport properties. Important properties are porosity ε and tortuosity τ which describe the geometry of the system. Porosity is defined as the ratio of free pore space over total volume, while tortuosity is a dimensionless parameter. It describes the deviation between the actual, winding, diffusion path against straight and parallel streamlines [34],

$$\tau = \frac{\lambda}{L} \geq 1 \quad , \tag{16}$$

where λ is the average length of the fluid paths and L is the geometrical length of the sample. The effective diffusion coefficient follows as [35],

$$D_i^{\text{eff}} = \frac{\varepsilon_i}{\tau_i^2} D_i \quad . \tag{17}$$

(2) Transport in the gas channels above the electrodes is typically described as laminar flow. In this flow regime the main forces acting on the fluid are its inertia and the friction at the channel walls. For flow through a circular channel the resulting pressure drop can be derived by the simplified equation [11],

$$\frac{dp}{dx} = \frac{32\bar{v}}{d^2} \quad , \tag{18}$$

where $\bar{v}$ is the mean flow velocity and d the channel diameter. A much more accurate and universally valid solution for the flow of a fluid is given by the Navier-Stokes equations (NSE). The NSE are a set of partial differential equations which describe mass, momentum and energy conservation for a fluid in a given space. In one-dimensional formulation for an incompressible fluid (valid for flow velocities < 0.3 Ma) they read as follows [7],

$$\frac{\partial \rho}{\partial t} = -\frac{\partial(\rho v)}{\partial x} + \frac{P_{\text{chem}}^{\text{cha}}}{A^{\text{cha}}} \sum \dot{s}_i^{\text{cha}} M_i \quad , \tag{19}$$

$$\frac{\partial(\rho v)}{\partial t} = -\frac{\partial(\rho v v)}{\partial x} - \frac{\partial p}{\partial x} - \frac{P_{\text{h}}^{\text{cha}}}{A^{\text{cha}}} \tau_{\text{w}} \quad , \tag{20}$$

$$\frac{\partial(\rho Y_i)}{\partial t} = -\frac{\partial(\rho v Y_i)}{\partial x} - \frac{\partial j_i^{\text{diff}}}{\partial x} + \frac{P_{\text{chem}}^{\text{cha}}}{A^{\text{cha}}} \dot{s}_i^{\text{cha}} M_i \quad , \tag{21}$$

where ρ is the density and v the viscosity of the fluid (here: gas), $P_{\text{chem}}^{\text{cha}}$ and $P_{\text{h}}^{\text{cha}}$ are electrochemically active and hydraulic channel diameter, A^{cha} the channel cross-sectional area, $\dot{s}_i^{\text{cha}}$ is the exchange rate between channel and porous electrode, M the molar mass of the species and τ_{w} the shear-stress factor.

(3) Charge transport occurs inside the electronically and ionically conducting phases. It depends on the conductivity σ, which is a measure for the charge transport properties of a material. The classical way to describe charge transport is by Ohm´s law,

$$V = IR = \frac{I}{G} \quad , \tag{22}$$

which quotes, that voltage V follows the product of current I and resistance R or the quotient of current and conductance G, respectively. This can be applied to calculate the voltage loss caused by the solid electrolyte of an SOC ($\eta_{\text{electrolyte}}$),

$$\eta_{\text{electrolyte}} = \frac{i}{\sigma_{\text{electrolyte}}} \quad , \tag{23}$$

where i and $\sigma_{\text{electrolyte}}$ indicate the volume specific measures for cell current and electrolyte

conductivity.

Applied to the conducting phases inside a porous electrode the conductivity of the material has to be corrected by its porosity and tortuosity, which gives the effective conductivity [8],

$$\sigma_i^{\text{eff}} = \frac{\varepsilon_i}{\tau_i^2} \sigma_i \qquad (24)$$

.

2.2.4 Polarization curve

If reaction steps, reaction kinetics transport properties and geometrical data are known, the prediction of current and voltage of the system is possible. The plot of the function $E_{\text{cell}} = f(i)$ (Eq. 5) is called polarization curve. At OCV ($i = 0$) no losses appear and the cell voltage equals the thermodynamically predicted Nernst potential (Eq. 8). Under polarization ($i \neq 0$) the losses induced by electrochemistry and transport sum up to the overvoltage η. The over-voltage can be subdivided into three parts: (1) activation overvoltage η_{act}, which describes losses due to reaction kinetics, (2) ohmic overvoltage η_{ohm}, which describes the losses due to electronic and ionic resistances, and (3) concentration overvoltage η_{conc}, which describes loss-es due to transport of reactants to the electrochemically active regions. Thus, the voltage of an SOC under polarization can be written as,

$$E_{\text{cell}} = E_{\text{rev}} - \eta_{\text{act}} - \eta_{\text{ohm}} - \eta_{\text{conc}} \qquad (25)$$

.

Figure 5 shows the simulated polarization curve of an H_2 fueled SOFC together with power density and the overpotential contributions from anode, cathode and ohmic resistance. The ohmic overvoltage increases linearly with current density due to Ohm´s law (Eq. 22). While the anode activation potential is relatively small, the cathode activation potential has one of the largest contributions to the total losses. Anode concentration overvoltages are relatively high due to the high thickness of the simulated anode of 1000 μm. At high current densities $\eta_{\text{conc,an}}$ increases significantly, indicating that the limiting current density (as given by the fuel inflow velocity) is reached. The cathode concentration overpotential is almost zero over the whole polarization curve, because of the low cathode thickness of 55 μm and high air inflow velocity. It is not shown here.

Note, that in fuel cell mode losses cause a decrease of cell voltage (as shown in Figure 5), while it is increased in electrolysis mode. The sign of η is chosen equal to the direction of current flow ($\pm i$).
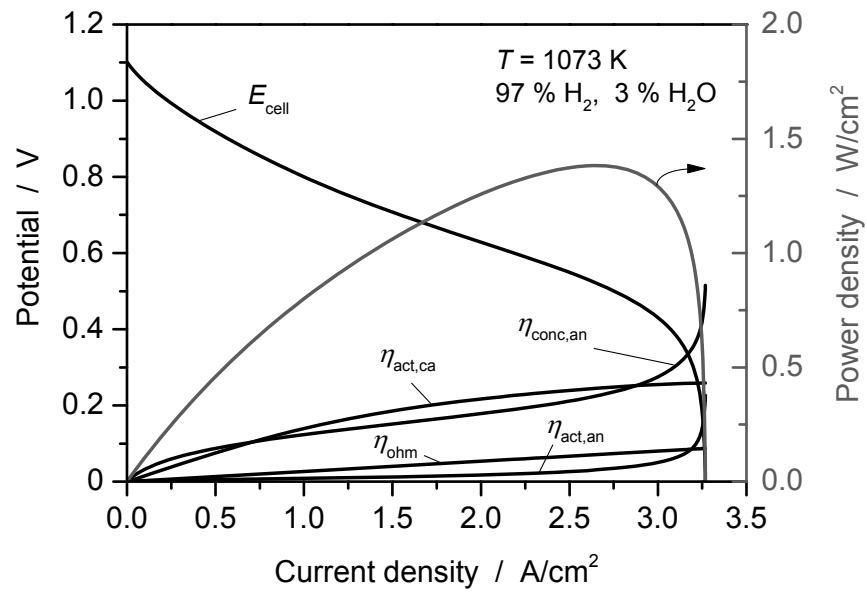
Figure 5. Cell voltage, power density and overpotentials as functions of current density for an SOFC operating on a fuel stream of 1 slm containing 97 % H_2 and 3 % H_2O against an air cathode.

2.3 Fuel electrode degradation

In addition to the losses caused by kinetics of the charge-transfer reaction and transport mechanisms, the losses caused by undesired side reactions and long term degradation effects have to be considered. Each component of an SOC can undergo degradation. Frequently the experimentally observed drop in cell performance over time is a combination of multiple processes. Degradation rates are often measured as voltage change (in %) per 1000 hours of operation at a constant current. Figure 6 shows an example of SOEC long term degradation measured at Forschungszentrum Jülich [36]. Alternatively degradation can be quantified by the change of the area specific resistance (ASR) of a cell.

A huge body of literature is available dealing with the experimental observation and modeling description of degradation issues. Recent reviews are given by Yokokawa [37] and Knibbe et al. [18]. The following paragraphs give an overview over the degradation phenomena which are known to occur at the fuel electrode of solid oxide cells.

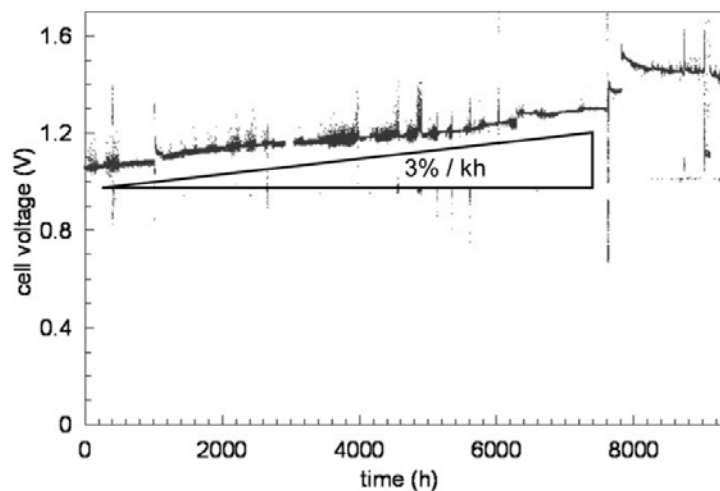Figure 6. Long term degradation of an SOEC during operation at $i = -1.0$ Acm^{-2}. Modified from [36].

2.3.1 Nickel oxidation

Focus of this thesis is the oxidation of the nickel electrode. This behavior due to reduction and reoxidation cycles (RedOx) and its effects on durability of SOFCs are well known from experimental literature [38]. Main problem is the volume increase of oxidizing nickel particles,

due to a change of molar volume from Ni to NiO by 69.9 % [39]. This produces mechanical stresses inside the porous anode structure [40], which can cause anode extension [41, 42], cracks [43, 44] and delamination from the electrolyte [45]. Figure 7 shows the impact of reoxidation on anode and electrolyte of an SOFC by SEM imaging [46]. After the first reoxidation the electrolyte phase has cracked due to the large volume expansion from nickel to nickel oxide. Additionally, nickel oxide (NiO) is an isolating material with very low ionic and electronic conductivity [47]. Therefore a layer of NiO can block the triple-phase-boundary (TPB) between nickel, electrolyte and gas phase, causing a break-down of the charge-transfer reaction (CTR). Another effect which has been observed is the reconfiguration of nickel particles during redox cycles, which can permanently decrease the TPB length [48].
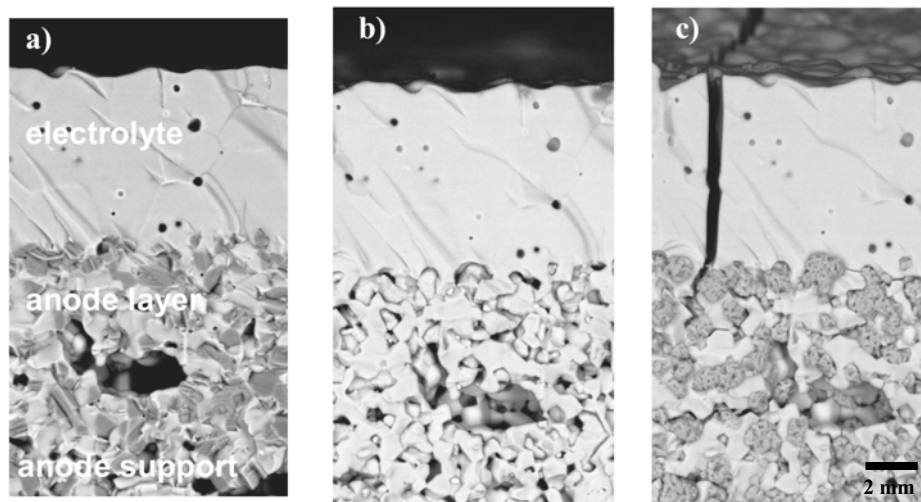

Figure 7. Microstructural changes in the anode of a SOFC [46]. a) New manufactured cell before first reduction (NiO/YSZ anode), b) reduced cell, c) re-oxidized cell.

Figure 8 shows data measured by Ivers-Tiffée et al. [49]. Plotted is the power density P (0.7 V) as a function of redox cycles for an electrolyte supported cell (ESC) in comparison to an anode supported cell (ASC) at three different temperatures. After 50 cycles the oxidation time was changed from 1 min to 10 min airflow. Results for the ESC show an increased loss of power output throughout the experiment. However, for the ASC results differ due to operation temperature. At 600 °C no effect is measured for short cycling and only a slightly decrease during the 10 min cycles. At 700 °C a small decrease of power is visible during the short cycles, which gets stronger during the longer cycles. At 800 °C the power oscillates around the initial value for the first 20 redox cycles, but breaks down strongly afterwards.
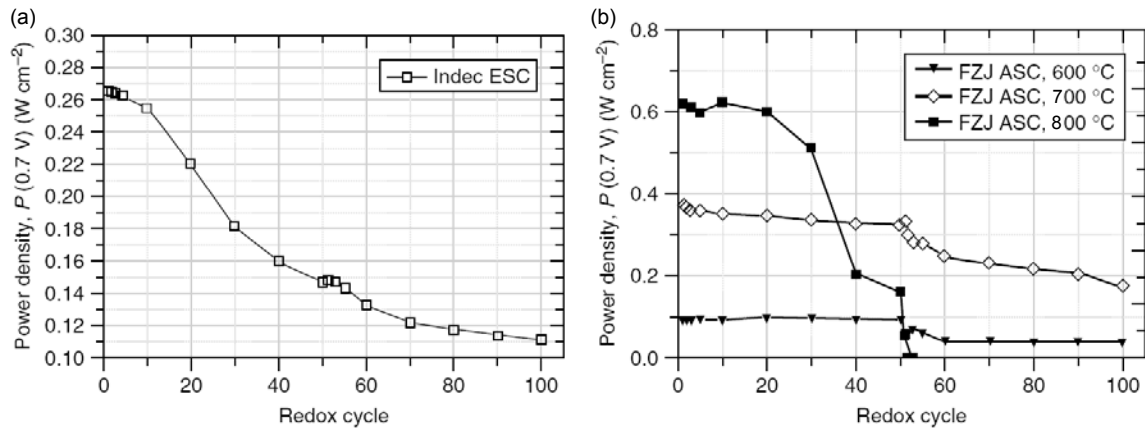
Figure 8. Power density as function of redox cycles (cycle 1−50: 1 min airflow, cycle 50−100: 10 min airflow) for (a) an ESC at 800 °C and (b) an ASC at 600, 700 and 800 °C [49].

The challenge of reoxidation accounts for solid oxide electrolyzer cells (SOEC), as well. Optimum system efficiency would be obtained by operation with 100 % steam. But due to the risk of reoxidation, it is a crucial question under which conditions no oxidation of the water electrode (here: cathode) will occur. Yang and Irvine [50] showed that a Ni-YSZ cathode operated in a binary mixture of Argon with 3 % steam (H_2O) at 1103 K was strongly oxidized. Figure 9 shows the corresponding IV-measurement and a photograph of the Ni/YSZ cathode which was taken after the experiment. The large slope of the current-voltage curve can be correlated to a high resistance, which corresponds to the decrease in electrochemically active area due to NiO formation. Green parts in the photo verify that a considerable part of the electrode was oxidized (metallic Ni is black and NiO is green) [50]. However, the number of studies dealing with reoxidation in SOECs is still very small [50, 51].
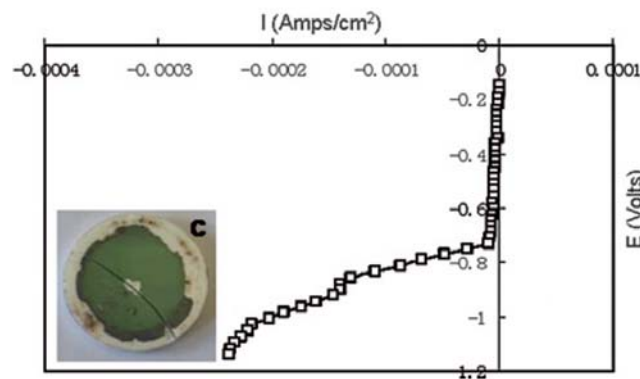

Figure 9. Performance of an SOEC with Ni/YSZ cathode at 830 °C under operation with a binary mixture of 3 % H_2O/Ar, together with a photo of the cathode taken after the test [50].

Two different pathways of the oxidation process can be distinguished, which are illustrated in Figure 10:

1) The first possible mechanism is a thermochemical reaction, driven by molecular oxygen (O_2) or a high water content of the fuel gas [39, 52],

$$Ni \; + \; \tfrac{1}{2} \, O_2 \; \rightleftarrows \; NiO \qquad\qquad (26)$$

$$Ni \; + \; H_2O \; \rightleftarrows \; NiO \qquad\qquad (27)$$

These reactions take place at the interface between metallic nickel and gas phase. During SOFC operation, thermochemical oxidation can occur, e.g., if the fuel utilization is too high, causing a low H_2/H_2O ratio at some parts of the cell. Other causes can be leakage of the electrolyte or sealing, which allow gas cross-over from the air electrode or a sudden break-down of the fuel gas supply, provoking a back-flow of air through the outlet channel.

2) The second oxidation mechanism is the electrochemical oxidation of nickel, taking place at the interface between nickel and the electrolyte phase [53, 54],

$$Ni \; + \; O^{2-} \; \rightleftarrows \; NiO + 2 \, e^- \qquad\qquad (28)$$

Here the metal is oxidized by oxygen ions from the electrolyte, releasing electrons. This mechanism takes place, for example, upon operation at low cell voltages or an interruption of the fuel supply during galvanostatic SOFC operation.

Details about thermodynamics, modeling and simulation of nickel oxide formation will be presented in Chapter 4.
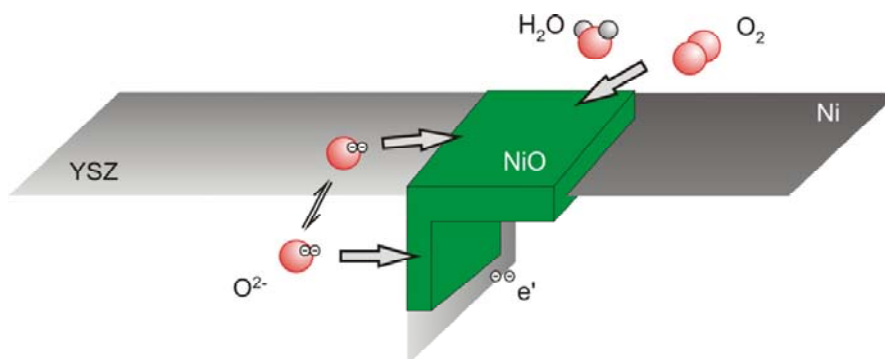

Figure 10. Schematic illustration of the reactions between Ni, YSZ and gas phase causing an oxidation of the metallic nickel. Oxidation can occur at the Ni/gas interface as well as at the Ni/YSZ interface.

2.3.2 Nickel coarsening

At SOC operation temperatures the nickel phase is partly mobile. The first lattice layers of the surface have a diffusion coefficient of about 10^{-10} m^{2}s^{-1} at 1100 °C [55]. Movement of the particles is mainly driven by the Gibbs-Thomson effect [56]: high curvatures have a higher chemical potential than low curvatures. In course of time this supports the growth of big particles with a smooth surface curvature (Ostwald ripening [57]). Inside the electrode of an SOC this is associated with a decrease of TPB length and has been measured for SOFC [41, 58] as well as for SOEC [36] operation. Experiments as well as modeling studies show that the biggest effect of Ni coarsening is occurring during the first 10 to 100 hours of cell operation [55, 59, 60]. Depending on the type of cell, an initial TPB reduction of about 25 % is typical [59]. Further sintering of the particles is strongly dependent on the steam content of the fuel gas [48, 61]. Faes et al. [41] developed a simple model to describe nickel coarsening as a process similar to charging of a capacitor,

$$r = (r_{\max} - r_0)\left(1 - \exp(-k_{s,cap}t)\right) + r_0 \quad , \tag{29}$$

where r_0 is the initial particle radius, $r_{\max}$ the maximal radius as given by the YSZ matrix, $k_{s,cap}$ a rate constant and t the time.

2.3.3 Nickel volatilization

Another degradation phenomenon is the volatilization of the nickel phase. It can occur if the fuel electrode is exposed to a high H$_2$O content, like in steam electrolysis or at high fuel utilization in SOFC mode. Thermodynamic calculations predict the formation of gaseous nickel hydroxide Ni(OH)$_2$ in a mole fraction larger than 10^{-10} for steam concentrations > 20 % [48]. Volatilization and re-deposition can cause morphological changes to the anode with considerable effect on cell performance. Hauch et al. [62] have suggested the formation of a dense nickel layer on top of electrolyte phase during SOEC operation. Figure 11 illustrates the underlying mechanism: At high current density electrolysis there will be electrical resistance in the YSZ particles. The resulting potential gradient is illustrated by $\Delta\phi$ in Figure 11b. As consequence the TPB points close to the electrolyte (red squares) will be more reducing than those at the top of YSZ particles (blue squares). Thus, the deposition of nickel hydroxide will take place at the red marked TPBs, causing a nickel film on top of the electrolyte phase. The same mechanism is believed to be responsible for microstructural changes and TPB reduction in SOFC experimental studies [48, 63, 64].
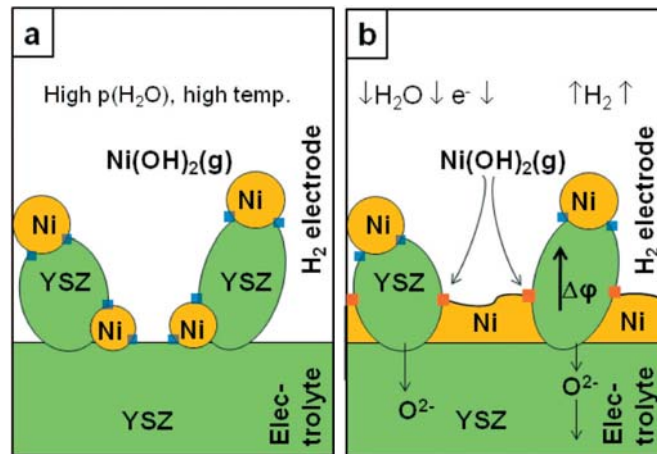
Figure 11. Possible mechanism for changes in the microstructure at the interface between cathode and electrolyte during high current density electrolysis operation: a) The YSZ-Ni/YSZ interface at OCV. TPBs are marked by blue squares. b) The interface at high current density electrolysis. The deposition of nickel hydroxide will take place at the red marked TPBs, with the higher reducing potential. Modified from [62].

2.3.4 Pollution of reactive surfaces

Many kinds of pollutants are known to appear on the surfaces inside SOC electrodes. They can either be contained in the fuel gas, like sulfur and phosphorus as compounds of natural gas [65, 66], or dissolved/segregated from inside the cell, like chromium out of ferritic components [67] or silicates as impurity of the YSZ material [68]. Equal to all contaminations is their impact on cell performance by blocking the electrochemically active surfaces. While the effect of internal pollutants can be minimized by optimization of the manufacturing process, the handling of gas impurities is challenging. Ryan and co-workers reviewed all species that have been traced in gasified coal for SOFC operation and their effect on cell degradation (Table 2) [69]. Current efforts aim towards a full understanding of the chemical reactions which underlie pollution [65, 66, 70]. Models combing thermodynamics and elementary reaction kinetics of all involved species have to be applied for finding operation strategies with minimum degradation.

Table 2. Effects of trace species in gasified coal on the anode of SOFC. Reprinted from [69].

Species	Observed reactions	Effect on SOFC	Trends with SOFC operation
Phosphorus (P)	Adsorbs to anode, forms Ni_xP_y on surface	Gradual increase of ohmic and electrodic polarization; sharp performance drop at high P concentration and formation of microcracks. Loss of electrical percolation. Poisoning occurs from the fuel channel and propagates into anode	Rates of degradation show no significant dependence on current density or fuel utilization. Increases with P concentration
Arsenic (As)	Ni consumption and migration from the anode matrix	Abrupt failure after long-term operation due to loss of electrical percolation	Depth of reaction area and agglomeration increase with AsH_3 concentration; no significant dependence on current density or fuel utilization
Selenium (Se)	Adsorbs near electrolyte interface; nanoparticles form at medium and high polarization; forms Ni_xSe_y at high current density	Rapid decrease in power to new steady state. Primarily an increase in electrodic polarization; minimal increase in ohmic loss; at intermediate current oscillatory behavior. Possible Ni_xSe_y at interface due to increase in O_2 partial pressure (pO_2). Partially reversible at low current	Increases with current and Se concentration; oscillations in performance at intermediate current; local pO_2 increases with large current
Sulfur (S)	Adsorbs to anode; may form Ni_xS_y at high current density	Rapid decrease in power to new steady state. At high current density Ni redistribution to small particles at electrolyte interface. Partially reversible under certain conditions	Increases with decreasing operating temperature; increases with increasing S concentration; increases with increasing operating voltage
Chlorine (Cl)	Adsorption of Cl to the Ni surface and possible sublimation of $NiCl_2$	Reversible increase in electrode polarization, decrease in ohmic loss at 700 °C due to scavenging effect of HCl	Higher HCl concentration leads to faster voltage change; degradation rate does not show dependence with polarization
Antimony (Sb)	Adsorption of Sb and formation of Ni_xSb_y on surface; Ni consumption and migration from matrix	Two-stage degradation: initial rapid decrease in voltage with increase in electrodic polarization; longer-term decrease in voltage with increase in ohmic loss. Loss of electrical percolation due to Ni_xSb_y	Initial stage: Nearly independent of Sb concentration; increasing degradation with decreasing current density. Late stage: Ni–Sb crystallite size grows with Sb

2.3.5 Carbon formation

The formation of solid carbon inside the SOFC anode is a special case of surface pollution. It is an undesired side product of internal reforming of hydrocarbons, which can totally block the surface of nickel as well as the free pore space and the charge-transfer reaction at the tree-phase boundary, as illustrated in Figure 12 [49]. The involved reaction paths are complex. Deutschmann and co-workers presented a system of 42 elementary-kinetic reactions which describe hydrocarbon reforming including the formation of surface carbon species [71]. Furthermore several different kinds of carbon can be distinguished, including graphitic carbon, encapsulating carbon, pyrolytic carbon, filament, and whisker carbon [21]. The removal of solid carbon is possible by addition of steam to the fuel gas [72]. However, high steam ratios bring the disadvantage of accelerated nickel coarsening (cf. Section 2.3.2) as well as the possibility of nickel oxide formation (cf. Section 2.3.1) and a reduced Nernst potential (cf. Section 2.2.1) [16]. Modeling studies based on thermodynamic data [66, 73] are capable to show safe operation conditions [74, 75].
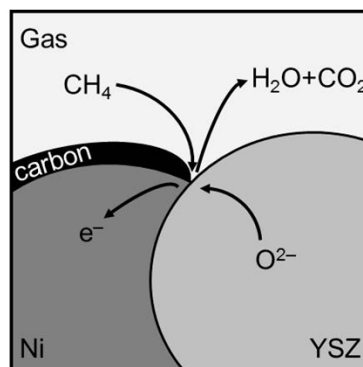

Figure 12. Illustration of solid carbon formation on top of the nickel surface in an SOFC anode. The surface of nickel is blocked, which prohibits reforming of hydrocarbons as well as the free pore space and the charge-transfer reaction at the tree-phase boundary [76].

2.4 Numerical modeling of SOCs

Computer-based modeling and simulation is one of the most prominent tools in contemporary sciences. Through representation of a physical system by differential equations (modeling) and their solution by means of a computer (simulation) the analysis of highly complex processes is possible. Regarding solid oxide cells, numerical modeling and simulation are being carried out on all spatial scales – from atoms (nm) to power plants (m). The focus of each model depends on its respective scale, as shown in Figure 13. It ranges from understanding the complex processes taking place between molecules and ions, over the prediction of the cell performance under diverse operating conditions, to the optimization of cell and system design.

Level	Scale		Chemistry	Transport	Modeling approach
System	10^0 m 10^4 s			Mass, energy fluxes	Process simulation
Cell	10^{-2} m 10^0 s		Gas-phase chemistry	Laminar flow, heat convection	Computational fluid dynamics (CFD)
Electrode	10^{-4} m 10^{-2} s		Thermal & Redox cycling	Porous multi-phase mass and charge transport	Continuum modeling Microstructural modeling
Surface	10^{-8} m 10^{-6} s		Surface chemistry, charge transfer, defect chemistry	Surface diffusion	Mean field
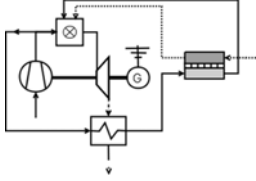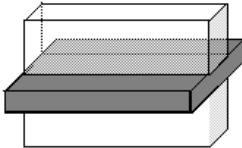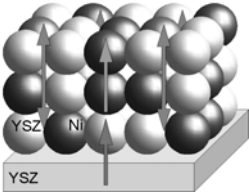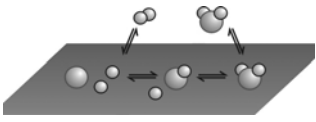
Figure 13. Time and length scales involved in solid oxide cell operation. Modified from [35].

2.4.1 Short review of SOC modeling literature

A large number of modeling work has been published in the last 20 years. Early studies focus on SOFCs. Common is a coupling of computational fluid dynamics (CFD) models with a global kinetic Butler-Volmer approach to describe the performance of the cell in 2D [77, 78] or 3D [79]. Simultaneously, the first models to describe the impedance of porous electrodes based on equivalent circuits were developed [80–82]. Drawback of this early work is the semi-empirical nature, which usually requires many fitting parameters and is only valid for predictions in a narrow range of operating conditions. Later studies overcome these limitations by including electrochemistry based on surface chemistry with elementary reaction steps [26, 29, 83] and detailed descriptions of porous electrode transport [84–87]. Review articles are available by several authors [88–92]. Recent work enhances the basic models by the implementation of mechanical or physico-chemical degradation processes. They include microstructural evolution of nickel particles [55, 93, 94], carbon deposition [74, 95], sulfur poisoning [69, 70, 96] and mechanical damage due to thermal stresses [97–99].

The first models of SOECs were published in the late 2000s. Typically the existing models of SOFCs were slightly modified to support electrolysis simulations [100–102]. Models including degradation effects are scarce, yet [103].

2.4.2 Discretization methods

A mathematical model gives a temporally and spatially continuous description of a system and the proceeding processes. For numerical solution the continuous equations have to be transformed to allow the computation of discrete points in space and time. Multiple techniques have been developed as optimum discretization methods for specific applications, of which the three most prominent methods for spatial discretization will be summarized here [104]:

- Finite Difference Method (FDM)

  FDM is the oldest and most simple discretization method. It is based on the differential form of the partial differential equations (PDE), which are approximated for each point of the computational grid. For a 1D case the solution follows from the definition of a derivative:

$$\left(\frac{\partial \phi}{\partial x}\right)_{x_i} = \lim_{\Delta x \to 0} \frac{\phi(x_i + \Delta x) - \phi(x_i)}{\Delta x} \qquad (30)$$

where the curve $\phi(x)$ is the desired solution and i a discrete point on x. Drawback of the FD method is its restriction to simple grid geometries.

- Finite Volume Method (FVM)

The FV method uses the integral form of the conservation equation [105]:

$$\frac{d}{dt} \int_{G_{cv}} \phi \; dV = - \int_{\partial G_{cv}} f(x) \cdot \mathbf{n} \; dS \qquad (31)$$

where G is a control volume (CV) with arbitrary size and shape and $\mathbf{n}$ is the normal vector. From Eq. 31 it follows that a change in ϕ can only occur in combination with a flux over the boundaries of the CV. Thus the solution of the PDEs follows from approximation of the net fluxes over the boundaries of all volumes. Main advantage of the FVM is that it is conservative, meaning that the flux entering a control volume is always equal to the flux leaving the adjacent CV. It is the most common discretization method in computational fluid dynamics [104].

- Finite Elements Method (FEM)

In contrast to FVM the FEM multiplies a weight function to each equation before it is integrated over the solution domain. The task is approximating a weight function W which guarantees continuity of the solution across the boundaries of all elements. It is applied in the form

$$\phi(x) = \sum_{i=1}^{m} W_i \cdot \phi_i(x) \qquad (32)$$

FEM can easily be applied for calculations based on a variable grid. Thus it is the method of choice in structural mechanics, e.g., for the simulation of deformation processes.

Discretization in time is typically integrated into the numerical solver, which allows a dynamic adaption of the step size to the time scale of simulated processes. Task of the solver is finding an accurate solution which fulfills the given system of equations. Based on a set of initial values, most solution methods are based on a stepwise (iterative) approach which aims to an

improved solution in each step of the calculation. Several methods suitable for application for solving the processes in electrochemical systems are given by Kee et al. [106].

2.4.3 Modeling and simulation errors

Due to effective algorithms numerical modeling is a powerful tool. Nevertheless, numerical solutions are never absolutely correct. Ferziger and Periç [104] describe three kinds of systematic errors which occur in every numerical calculation:

1) Modeling errors

   Modeling errors are errors which are already contained in the mathematical model. This includes assumptions like modeling gases as 'ideal' or by reducing a complex 3D geometry to a homogenized 1D transport problem (e.g., the porous electrodes in SOC, Section 2.2.3).

2) Discretization errors

   Discretization errors are errors which are introduced by discretizing the domain in space and time. They can be decreased by refinement of the grid and the solver step-size, which, however, implies an increase in calculation time.

3) Convergence errors

   Convergence errors describe the deviation between iterative and exact solution of the equation system. The maximum allowed size of this error can typically be defined as input parameter of the solver algorithm.

Two conclusions can be drawn:

1) Reduction of errors can only be achieved by an increased input of (simulation-)time. Since time is limited, distinguishing or deciding which errors are acceptable is an important task.

2) Interpretation of simulation results always needs to be conducted by keeping in mind the effects induced by the chosen accuracy level.

A discussion of modeling and simulation errors in this work is given in Section 4.8.

3 MULTI-PHASE MODELING AND SIMULATION FRAMEWORK

3.1 Introduction

Basis for all numerical simulations presented in this work is the software package DENIS (detailed electrochemistry and numerical impedance simulation) which is being developed by W. G. Bessler and his group since 2004 [35]. When this thesis was initiated in February 2010 the status of development regarding the modeling and simulation of SOCs was the following:

1) A detailed model of an SOFC was present (in the following called base model). It included an elementary-kinetic description of electrochemistry, the physical representation of potential steps due to electrical double layers and a quasi-three-dimensional multi-scale description of mass and charge transport. The implementation allowed the simulation of polarization curves (steady-state solution) as well as impedance spectra (transient solution) [7]. The model was validated using data from a planar segmented SOFC and could represent the experimental data over a wide range of operating conditions [107]. A model for performance degradation was not included so far.

2) Since solid oxide electrolysis is based on the identical fundamental physico-chemical processes, the modeling framework in principle allowed for simulating electrolysis, too. However, this functionality was never applied scientifically.

For modeling the formation of a bulk nickel oxide phase the code had to be extended significantly. Specifically a module for the dynamic handling of multiple phases was added. Flexibility in formulating chemical reactions was achieved by coupling with the software package CANTERA [108]. By implementation in a general form, the abilities of DENIS to simulate different types of fuel cells and batteries could be enhanced simultaneously. This chapter gives an extensive description of the multi-phase modeling framework which was developed. Additionally examples of application for modeling secondary-phase formation in PEFC and next-generation batteries are presented.

The new model was published by Neidhardt et al. in the Journal of the Electrochemical Society [8] and presented at the 9th Symposium on Fuel Cell and Battery Modeling and Experimental Validation (ModVal 9) [109] and the 10th European SOFC Form (EFCF 2012) [110].

3.2 Base model

For a complete description of the modeling framework this section briefly summarizes the model implemented by Bessler et al. before initiation of the present work. All equations included in the base model are listed in Table 3. For details of model derivation and application the reader is referred to the available publications [7, 27, 35, 111].

3.2.1 Transport

Mass and charge transport take place within bulk phases (e.g., molecules in the gas phase, ions in liquid electrolytes, electrons in solid conductors). The following transport processes are modeled:

1) Channels/gas-phase: Gas-phase convective and diffusive flow, described with a one-dimensional form of the Navier-Stokes equations (Table 3, Eqs. 33−36).

2) Porous electrodes/gas-phase: Diffusive and convective flow, described by coupled diffusion flow (Stefan-Maxwell law using Bosanquet diffusion coefficients that account for ordinary and Knudsen diffusion, Table 3, Eqs. 37−38) and for pressure-driven flow (Darcy law, Table 3, Eq. 39).

3) Porous electrodes and separator/solid phase: Electronic and ionic charge transport, described by Ohm's law (Table 3, Eqs. 40−41).

4) Cell current and voltage are derived from the electric potential distribution and the current due to electrochemical reactions and double layer charge/discharge (Table 3, Eqs. 46−49).

5) Transport over the three-phase boundary (TPB): Surface diffusion of adsorbed species perpendicular to the TPB line [7, 27].

All transport processes are coupled within a quasi-three-dimensional multi-scale modeling approach, as illustrated in Figure 14. In the channels, mass transport is modeled in one dimension (x) in flow direction. In the electrodes, mass transport is modeled in one dimension (y) perpendicular to the membrane/separator. This yields an overall 1D+1D model. The model can be extended by surface transport perpendicular to the three-phase boundary, giving rise to an overall 1D+1D+1D model.
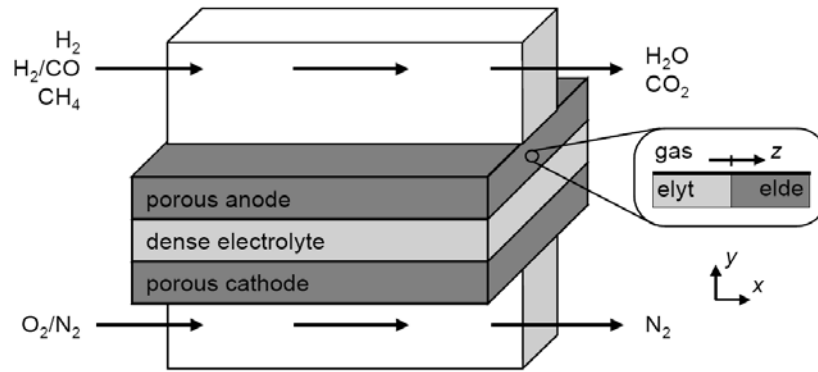
Figure 14. Schematic representation of the quasi-three-dimensional modeling approach. The x dimension (mm-cm scale) is along the gas channels, the y dimension (mm-µm scale) through the MEA thickness, and the z dimension (µm-nm scale) perpendicular to the three-phase boundary line [7].

3.2.2 Electrochemistry

The species continuity equations for the porous electrodes (Table 3, Eqs. 37−39) include source terms $\dot{s}_i$ due to interfacial reactions. These are the net production rates of the species i, which can be calculated according to mass-action kinetics (Table 3, Eq. 42). Forward and backward rates of each reaction are given by a modified Arrhenius equation (Table 3, Eq. 43) and thermodynamic consistency, respectively (Table 3, Eq. 44). Thermodynamic data for the molar enthalpy h and the molar entropy s is taken from literature (either explicitly from thermodynamic tables or implicitly by converting from kinetic data). The latter are used to compute the temperature-dependent values for the molar Gibbs reaction enthalpy ΔG (Table 3, Eq. 45). The absolute production rates of bulk species are obtained by multiplying area-specific (or line-specific) rates of production with the surface area A^V or the boundary length l^V. The Faradaic current density i_F follows from the sum over the net production rates of electrons $\dot{s}_{\text{electron}}$ of all reactions (Table 3, Eq. 49). The same ansatz is used to compute chemistry between species within a bulk phase, like gas-phase reactions.

Table 3. Summary of equations of the base model.

Physicochemical process	Model equation	
Gas-phase transport in channels		
Continuity	$\dfrac{\partial \rho}{\partial t} = -\dfrac{\partial(\rho v)}{\partial x} + \dfrac{P_{\mathrm{chem}}^{\mathrm{cha}}}{A^{\mathrm{cha}}} \sum \dot{s}_i^{\mathrm{cha}} M_i$	(33)
Momentum conservation	$\dfrac{\partial(\rho v)}{\partial t} = -\dfrac{\partial(\rho v v)}{\partial x} - \dfrac{\partial p}{\partial x} - \dfrac{P_{\mathrm{h}}^{\mathrm{cha}}}{A^{\mathrm{cha}}} \tau_{\mathrm{w}}$	(34)
Species conservation	$\dfrac{\partial(\rho Y_i)}{\partial t} = -\dfrac{\partial(\rho v Y_i)}{\partial x} - \dfrac{\partial j_i^{\mathrm{diff}}}{\partial x} + \dfrac{P_{\mathrm{chem}}^{\mathrm{cha}}}{A^{\mathrm{cha}}} \dot{s}_i^{\mathrm{cha}} M_i$	(35)
Ideal gas law	$p = \rho RT \sum\limits_i Y_i / M_i$	(36)
Gas-phase transport in porous electrodes		
Species conservation	$\dfrac{\partial(\varepsilon\, c^{\mathrm{g}} X_i)}{\partial t} = -\dfrac{\partial J_i^{\mathrm{diff}}}{\partial y} - \dfrac{\partial J_i^{\mathrm{flow}}}{\partial y} + \sum\limits_m A_m^{\mathrm{V}} \dot{s}_{i,m}$	(37)
Diffusive fluxes: Stefan-Maxwell law	$\dfrac{\partial(c^{\mathrm{g}} X_i)}{\partial y} = \sum\limits_{j \in S_{\mathrm{g}}} \dfrac{X_i J_j^{\mathrm{diff}} - X_j J_i^{\mathrm{diff}}}{D_{ij}^{\mathrm{eff}}}$	(38)
Pressure-driven porous fluxes: Darcy flux	$J_i^{\mathrm{flow}} = X_i c^{\mathrm{g}} \dfrac{B}{\mu_{\mathrm{g}}} \dfrac{\partial p}{\partial y}$	(39)
Charge transport in solid conductors		
Coupled ionic and electronic charge transport (electrodes)	$\dfrac{\partial}{\partial y}\left(\sigma_{\mathrm{elyt}} f_\sigma \dfrac{\partial(\Delta\phi)}{\partial y} \right) = -\left(i_{\mathrm{F}} + i_{\mathrm{dl}} \right)$	(40)
Ionic charge transport (solid electrolyte)	$\dfrac{\partial}{\partial y}\left(\sigma_{\mathrm{electrolyte}} \dfrac{\partial \phi_{\mathrm{electrolyte}}}{\partial y} \right) = 0$	(41)
Electrochemistry		
Species production rate	$\dot{s}_i = v_i\left(k_f \prod\limits_{j \in R_f} a_j^{v_j'} - k_r \prod\limits_{j \in R_r} a_j^{v_j''} \right)$	(42)
Forward rate constant	$k_{\mathrm{f}} = k_0^{\mathrm{f}} T^\beta \exp\left(-\dfrac{E_{\mathrm{f}}^{\mathrm{act}}}{RT} \right) \exp\left(-\dfrac{\alpha z F}{RT} \Delta\phi \right)$	(43)
Reverse rate constant	$\dfrac{k_{\mathrm{f}}}{k_{\mathrm{r}}} = \exp\left(-\dfrac{\Delta G}{RT} \right)$	(44)
Molar Gibbs reaction enthalpy	$\Delta G = \sum\limits_{i \in R} v_i \mu_i = \sum\limits_{i \in R} v_i (h_i - T s_i)$	(45)
Cell current and voltage		
Cell voltage	$E = \phi_{\mathrm{ca}} - \phi_{\mathrm{an}}$	(46)
Total current density	$i = \int\limits_{y=0}^{L_{\mathrm{electrode}}} \left(i_{\mathrm{F}} + i_{\mathrm{dl}} \right) \mathrm{d}y$	(47)
Current density due to electrical double layer	$i_{\mathrm{dl}}(t) = A_{\mathrm{dl}}\, C_{\mathrm{dl}} \dfrac{\partial(\Delta\phi)}{\partial t}$	(48)
Faradaic current density	$i_{\mathrm{F}} = \sum\limits_m F \dot{s}_{\mathrm{electron},m} A_m^{\mathrm{V}} + \sum\limits_n F \dot{s}_{\mathrm{electron},n} l_n^{\mathrm{V}}$	(49)
Potential step	$\Delta\phi = \phi_{\mathrm{electrode}} - \phi_{\mathrm{electrolyte}}$	(50)

3.2.3 Base model performance

The performance of the base model was tested and compared to experimental under various operation conditions of an segmented SOFC by Bessler and colleagues [107]. Selected results are shown in Figure 15.
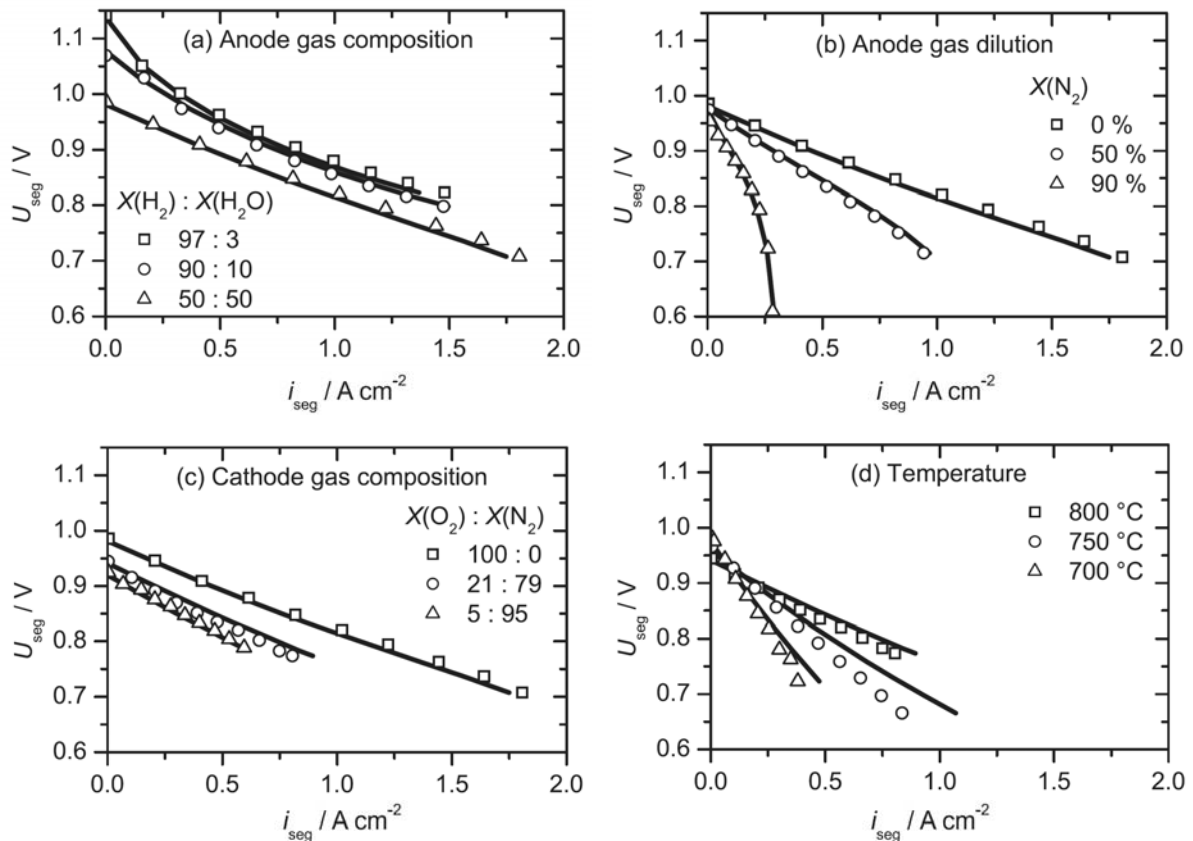
Figure 15. Comparison of 1D model calculations (base model) to experimental data under validation conditions (low fuel utilization). (a) Variation of anode gas composition without N_2 at 800 °C with cathode at 100 % O_2, (b) Variation of anode gas dilution with 50 % H_2 and 50 % H_2O at 800 °C and cathode at 100 % O_2, (c) Variation of cathode gas composition at 800 °C with anode at 50 % H_2 and 50 % H_2O, (d) Variation of temperature with anode at 50 % H_2 and 50 % H_2O and cathode air. Modified from [107].

3.3 Generalized computational domain

In order to realize multi-step management, a first necessary step was the generalization of the computational domain with respect of the phases, species and chemical reactions involved. Although this does not result in new conservation equations, it required careful definition and considerable coding effort (cf. Section 3.5). The computational domain for the generalized framework is shown in Figure 16. It represents the basic repeat unit of an electrochemical cell. The model is based on the following assumptions and constituents:

1) The computational domain consists of up to seven *layers*. The base cell functionality requires at least three layers, representing anode, cathode and electrolyte/separator. Additional layers can be added for gas supply (gas channels), as required for solid oxide cells and for current collection. The layers are characterized by their macroscopic geometry (thickness).

2) Each layer consists of an arbitrary number of *bulk phases*. They can either be solid, liquid, or gaseous. The phases are characterized by their respective volume fraction ε and density ρ. For layers consisting of multiple phases, a continuum (homogenization) approach is applied [7, 33]. Properties of a layer are given by effective continuum parameters, like porosity, tortuosity, conductivity, volume-specific area and volume-specific boundary length. This approach is in contrast to an exact representation of the microstructure, with the gain of a significantly reduced simulation time.

3) Each bulk phase consists of an arbitrary number of chemical species. This can be a single species making up a bulk phase (e.g., NiO in bulk nickel oxide), or a mixture of species in the gas phase or a liquid solvent. The species are characterized by their concentrations c (or mole fractions X).

4) Each layer can also contain an arbitrary number of *phase boundaries*. These can be two-phase boundaries (interfaces) or three-phase boundaries (edges). They are characterized in the continuum approach by their volume-specific area A^V and the volume-specific boundary length l^V, respectively. Area and length generally depend on the volume fraction of the adjacent bulk phases; this dependence describes the influence of microstructure on reactivity.

5) Optionally, *surface-adsorbed species* can be defined at each interface. This allows to describe electrochemical reactions based on elementary kinetics [26]. Surface adsorb-

ates are characterized by their coverage θ.

6) An arbitrary number of *chemical reactions* take place at each phase boundary. Reactions may involve species from one or several adjacent bulk phases and/or surface-adsorbed species.

7) *Mass and charge transport* occur within the 1D+1D+1D modeling domain (cf. Section 3.2.1).

Within this generic framework, different applications (solid oxide cells, batteries, etc.) differ only in number and type of constituents (layers, phases, boundaries, species, reactions) as well as their structural, chemical and transport properties.
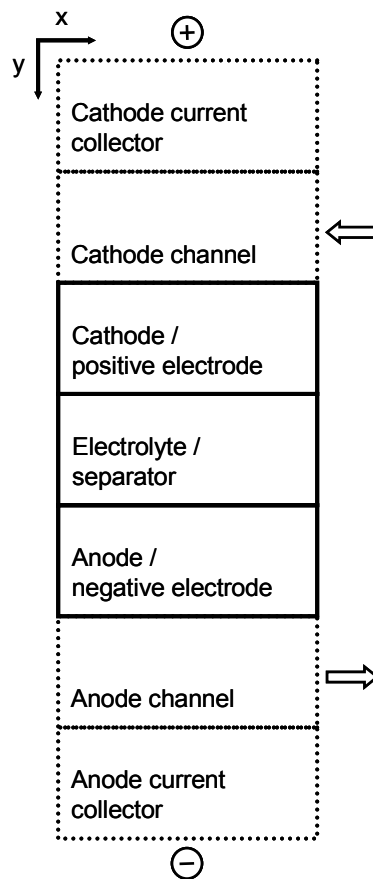

Figure 16. Fundamental repeat unit of a solid oxide cell, fuel cell or battery consisting of up to seven layers. Dotted lines represent optional components.

3.4 Multi-phase management

3.4.1 Multi-phase reactions

Modeling the evolution of phases requires the introduction of a multi-phase management. The volume fraction of a bulk phase can change by three different processes, that is, phase formation/dissolution, phase transition, and phase transport:

1) Phase formation/dissolution is characterized by mass transfer from one phase to another by an (electro-)chemical reaction. For example, the oxidation of nickel metal by oxygen creates a new phase of solid nickel oxide (NiO), dissolving the nickel phase,

$$2\,\mathrm{Ni} + \mathrm{O}_2^{(gas)} \; \rightleftharpoons \; 2\,\mathrm{NiO} \; . \tag{51}$$

Reaction kinetics of the phase formation/dissolution can be described by Eqs. 42−45 (Table 3).

2) Phase transition describes the change between different states of aggregation. Even though a phase transition is not a chemical reaction in a conventional sense, it obeys the laws of thermodynamics and can be treated as special case of a reaction between two bulk phases. Therefore the formulation above (Table 3, Eqs. 42−45) can be applied to phase transitions as well. For example, the transition from liquid water to steam is written as reversible reaction,

$$\mathrm{H}_2\mathrm{O}^{(liquid)} \; \rightleftharpoons \; \mathrm{H}_2\mathrm{O}^{(gas)} \; . \tag{52}$$

3) Phase transport occurs, for example, in PEFCs where the presence of liquid water has to be considered. Phase transport is not included in the present work. All solid phases (Ni, NiO, YSZ) are assumed spatially immobile.

3.4.2 Governing equations

Purpose of the multi-phase management module is accounting for the volume fractions ε of all phases within a layer as a function of time and spatial location inside the cell. Mass conservation of each phase i is described in terms of the mass density ($\rho\varepsilon$) via the continuity equation,

$$\frac{\partial(\rho_i \varepsilon_i)}{\partial t} = R_i M_i \quad , \tag{53}$$

where ρ_i is the density and M_i the mean molar mass of phase i. It is assumed, that phase formation/dissolution reactions occur at interfaces between two or more phases. The rate of formation R_i follows from the chemical source terms $\dot{s}_{i,m}$ of all reactions m involving phase i, including surface reactions, surface/gas phase reactions, surface/bulk reactions, and charge-transfer reactions. It is given by

$$R_i = \sum_m \dot{s}_{i,m} A_m^{\mathrm{V}} \quad , \tag{54}$$

where A_m^{V} accounts for the volume specific surface area corresponding to reaction m. For reactions including more than two phases, the term of the active surface area is replaced by the active boundary length l_m^{V} in between all involved phases,

$$R_i = \sum_m \dot{s}_{i,m} l_m^{\mathrm{V}} \quad . \tag{55}$$

Phase formation/dissolution reactions, like growth of solid structures, can cause changes to the total volume of the solid materials. As a result the pressure and/or volume of the system can vary. This effect is handled by defining compressible phases. If present, the gas phase fulfills this role (e.g., in solid oxide cells): Upon solid volume fraction increase, gas-phase volume fraction decreases and gas-phase pressure increases, as described by the ideal gas law. One of the requirements of the present model was its flexibility in usage for other types of electrochemical cells, in particular, batteries. In batteries, no gas-phase is present. Here, the property of a "compressible" phase is assigned to the liquid electrolyte: Upon solid volume fraction increase, electrolyte volume fraction decreases, and concentrations of electrolyte species increase. This assumption ensures mass conservation. It could also be interpreted as presence of a buffer volume for the liquid phase not included in the computational domain (e.g., by slight expansion of the cell dimensions). A full description of such effects would require the integration of a mechanical model (describing pressure increase and compression effects inside the electrode) as well as convective liquid flux into the buffer volume, which is out of the scope of the present work. The volume fraction of the compressible phase is described by applying the constraint

$$\sum_i \varepsilon_i = 1 \quad . \tag{56}$$

Eqs. 53–56 are of central importance for modeling multi-phase behavior of electrochemical

systems. Firstly, they allow following the dynamic change of bulk phases, which is fundamental for solid oxide cells (where secondary phase formation represents important degradation mechanisms) as well as for batteries (where the state of charge is directly related to volume fractions). More importantly, they allow a direct coupling to both, chemical kinetics (via modification of interfacial areas) and transport (via modification of transport coefficients and available transport pathways). This will be further described below.

3.4.3 Feedback between multi-phase management and microstructure

The spatial appearance of secondary phases, as well as changes in the volume fractions of primary phases, has multiple effects on structure, chemistry and bulk transport processes. Concerning microstructure, key parameters used in the present model are the volume-specific two-phase interfacial areas $A_{m,n}^{\mathrm{V}}$ between two bulk phases m, n, and the volume-specific three-phase specific lengths $l_{m,n,o}^{\mathrm{V}}$ between three phases m, n, o. A general expression can be used to describe their dependence on changes of bulk-phase volume fractions,

$$A_{m,n}^{\mathrm{V}} = A_0^{\mathrm{V}} \cdot f_{m,n}(\varepsilon_m, \varepsilon_n) \cdot f_{\mathrm{num}} \quad , \tag{57}$$

$$l_{m,n,o}^{\mathrm{V}} = l_0^{\mathrm{V}} \cdot f_{m,n,o}(\varepsilon_m, \varepsilon_n, \varepsilon_o) \cdot f_{\mathrm{num}} \quad , \tag{58}$$

where A_0^{V} is the initial surface area and l_0^{V} the initial boundary length. The functions f describe the change of A_0^{V} or l_0^{V} depending on the volume fractions of adjacent phases and f_{num} is an additional term for improvement of numerical stability in case of the volume fraction of an adjacent phase approaching to zero (cf. Sections 3.5 and 4.3.1). The relationships described by f can be either empirical, or based on geometrical considerations. For example, the formation of a surface film in a system of cylindrical pores can be described by the square root of the surrounding medium [112]. This yields the geometrical expression,

$$f_{\mathrm{surface}} \sim \sqrt{\varepsilon_{\mathrm{pore}}} \quad , \tag{59}$$

which is schematically plotted in Figure 17. The relationships used to model nickel oxide formation in solid oxide cells are given in Section 4.3.1.
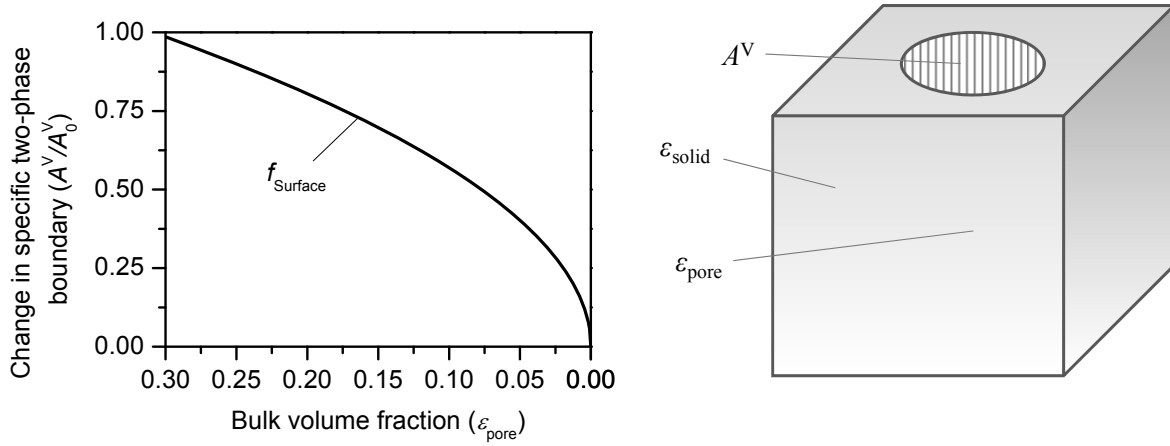
Figure 17. Effect on the volume-specific two-phase boundary A^V between solid and pore phase as function of change in pore volume fraction.

Changes in microstructure directly influence reaction rates, because chemical source terms in the governing equations are proportional to the volume-specific surface area and TPB length (Eqs. 37−39). This can be illustrated at the case of nickel oxide formation: If a part of the electrode is fully oxidized, the nickel volume fraction tends to zero and, consequently, the triple-phase boundary between Ni, YSZ and gas-phase tends to zero, as well (cf. Chapter 4).

3.4.4 Feedback between multi-phase management and transport coefficients

In the continuum approach used in this work, mass and charge transport are described through effective coefficients (diffusion coefficients, conductivities). They are assumed to depend on volume fraction ε_i as well as on tortuosity factor τ_i^2 of the bulk phase according to

$$D_i^{\mathrm{eff}} = \frac{\varepsilon_i}{\tau_i^2} D_i \quad \text{and} \quad \sigma_i^{\mathrm{eff}} = \frac{\varepsilon_i}{\tau_i^2} \sigma_i \qquad (60)$$

where D is a diffusion coefficient (e.g., gas-phase or liquid-phase species diffusion coefficient), σ is a conductivity (solid-phase ionic or electronic conductivity), and τ is a tortuosity.

In the transport equations, the time derivative of the conservation variable includes the volume fraction of the respective phase (Eqs. 37−39). This can be interpreted as a chemical capacitance. The dynamic behavior of mass and charge transport is thus strongly influenced by multi-phase management.

3.5 Simulation methodology

3.5.1 Implementation and simulation procedure

The modeling framework is mathematically represented by a differential-algebraic equation system (DAE). It describes the implicit relationship between current density i and cell voltage E of an electrochemical cell under consideration of multi-phase management, chemistry, and transport processes. It was implemented into the software package DENIS (detailed electro-chemistry and numerical impedance simulation) developed by Bessler and co-workers [27]. To evaluate the chemical source terms ($\dot{s}_i$ in Eq. 42) the code CANTERA, developed by Goodwin and co-workers [108], is used. CANTERA is open-source software for solving complex chemical reaction systems based on conveniently-structured input files. Both codes were connected on code-basis, making the full CANTERA functionality available during DENIS runtime. For numerical simulation, the computational domain is spatially discretized using the finite-volume method. The resulting DAE system is solved using LIMEX [113]. Analytic expressions for specific boundaries (e.g., Eqs. 57 and 58) are evaluated using mu-Parser [114]. A schematic representation of the DENIS package, illustrating the main modules and their interconnections, is given in Figure 18.
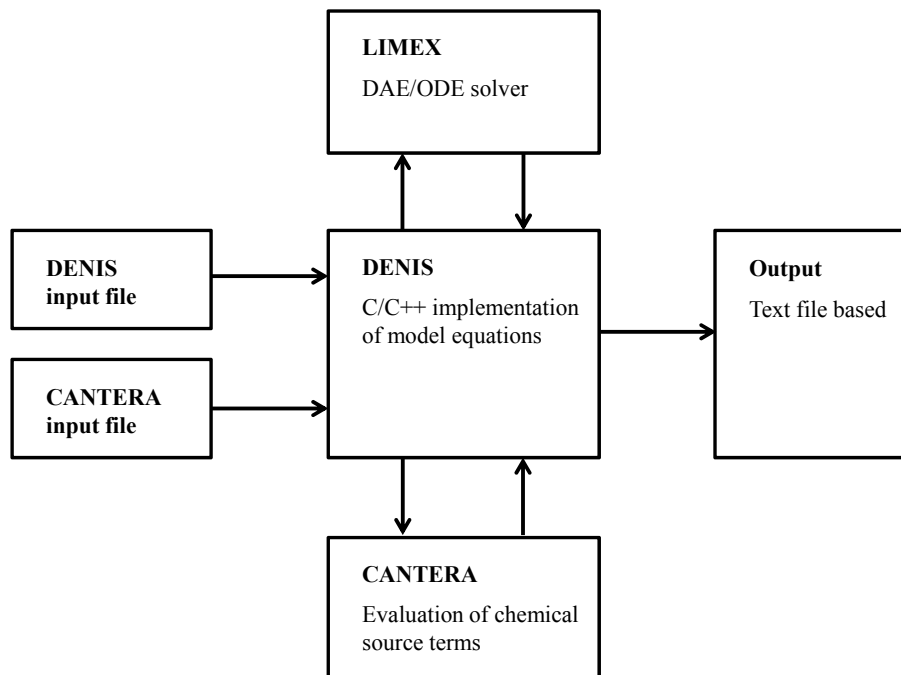

Figure 18. Schematic representation of the DENIS software package.

The full model functionality is controlled via two ASCII input files: (1) a DENIS input file controlling phase management, transport parameters and simulation methodology, and (2) a CANTERA input file controlling thermodynamic and kinetic properties of phases and species. Figure 19 shows an extract of the CANTERA input file for modeling solid oxide cells. Shown are the definitions of a nickel surface and an YSZ surface, including surface adsorbed species and elementary reaction steps. All data is provided in a conveniently structured and self-explaining style.

Simulations are carried out on a conventional desktop computer (Intel core i7 with 2.93GHz, 4GB RAM, 64-bit, Windows 7). Simulation times vary between seconds, for 0D simulations (pure thermodynamics and electrochemistry), up to 1−3 weeks for full resolution 1D+1D calculations including multi-scale transport and secondary phase formation.

```
# Nickel-Gas surface
#--------------------------------------------------------------------
ideal_interface(
    name = "Nickel_surface",
    phases = 'gas_anode nickel',
    site_density = (6.10e-9, 'mol/cm2'),
    elements = "Ni H O",
    species = " H(Ni) O(Ni) OH(Ni) H2O(Ni) (Ni)",
    reactions = ["Ni-rxn-*"],
    initial_state = state( coverages = '(Ni):1.0')

    )

# Thermodynamics
species( name = "(Ni)",      atoms = "Ni:1",          thermo = const_cp(h0 = (0.0, 'kJ/mol'),    s0 = (0.0, 'J/mol/K')))
species( name = "H(Ni)",     atoms = "Ni:1 H:1",      thermo = const_cp(h0 = (-31.81, 'kJ/mol'), s0 = (40.73, 'J/mol/K')))
species( name = "O(Ni)",     atoms = "Ni:1 O:1",      thermo = const_cp(h0 = (-221.635, 'kJ/mol'),s0 = (38.981, 'J/mol/K')))
species( name = "OH(Ni)",    atoms = "Ni:1 O:1 H:1",  thermo = const_cp(h0 = (-192.74, 'kJ/mol'), s0 = (106.44, 'J/mol/K')))
species( name = "H2O(Ni)",   atoms = "Ni:1 H:2 O:1",  thermo = const_cp(h0 = (-273.215, 'kJ/mol'),s0 = (130.696, 'J/mol/K')))

# Reaction mechanism
surface_reaction( "H2 + (Ni) + (Ni) <=> H(Ni) + H(Ni)",   [9.80000E+17, 0.5, 0.0],   id = 'Ni-rxn-1')
surface_reaction( "H2O + (Ni) <=> H2O(Ni)",               [1.40000E+10, 0, 0.0],     id = 'Ni-rxn-2')
surface_reaction( "H(Ni) + O(Ni) <=> OH(Ni) + (Ni)",      [5.00000E+22, 0, 97.9],    id = 'Ni-rxn-3')
surface_reaction( "H(Ni) + OH(Ni) <=> H2O(Ni) + (Ni)",    [3.00000E+20, 0, 42.7],    id = 'Ni-rxn-4')
surface_reaction( "H2O(Ni) + O(Ni)<=> OH(Ni) + OH(Ni)",   [5.42300E+23, 0, 209.37],  id = 'Ni-rxn-5')
surface_reaction( "O2 + (Ni) + (Ni) <=> O(Ni) + O(Ni)",   stick(0.01, 0, 0.0),       id = 'Ni-rxn-6')


# YSZ-Gas surface
#--------------------------------------------------------------------
ideal_interface(
    name = "YSZ_surface",
    phases = 'gas_anode YSZ',
    site_density = (1.3e-9, 'mol/cm2'),
    elements = "O  H  E",
    species = "O--(YSZ) OH-(YSZ) H2O(YSZ) (YSZ)",
    reactions = 'YSZ-rxn-*'
    )

# Thermodynamics
species( name = "(YSZ)",      atoms = "",          thermo = const_cp(h0 = (0.0, 'kJ/mol'),      s0 = (0.0,'J/mol/K')))
species( name = "O--(YSZ)",   atoms = "O:1 E:2",   thermo = const_cp(h0 = (-236.383, 'kJ/mol'), s0 = (0.0, 'J/mol/K')))
species( name = "OH-(YSZ)",   atoms = "O:1 H:1 E:1",thermo = const_cp(h0 = (-282.485, 'kJ/mol'), s0 = (66.99, 'J/mol/K')))
species( name = "H2O(YSZ)",   atoms = "H:2, O:1",  thermo = const_cp(h0 = (-272.982, 'kJ/mol'), s0 = (97.94,'J/mol/K')))

# Reaction mechanism
surface_reaction("(YSZ) + O--[YSZ] <=> V[YSZ] + O--(YSZ)",     [1.6e22, 0.0, (91.0, 'kJ/mol')],   id = "YSZ-rxn-01")
surface_reaction("H2O + (YSZ)<=> H2O(YSZ)",                    [6.595e11, 0.5, (0.0, 'kJ/mol')],  id = "YSZ-rxn-02")
surface_reaction("H2O(YSZ) + O--(YSZ) <=> OH-(YSZ) + OH-(YSZ)", [1.591e22, 0.0, (9.647, 'kJ/mol')], id = "YSZ-rxn-03")
```

Figure 19. Extract of the CANTERA input file for modeling solid oxide cells.

3.5.2 Numerical stability

For numerical stability the rates of formation of solid phases (Eqs. 54 and 55) which are approaching a volume fraction of zero during simulation runtime are set to zero. This is realized by an additional term which is multiplied to the equation, describing the size of the respective interfaces (surface area or triple phase boundary length, Eqs. 81 and 84). The hyperbolic tangent function is applied to model a numerically stable smooth transition between an active interface ($f_{num} = 1$) and a non-active interface ($f_{num} = 0$). The exact function depends on the number and type of bulk phases adjacent to the respective surface. The implementation regarding nickel oxide formation is described below (Section 4.3).

3.6 Demonstration models

Focus of this work is modeling the formation of NiO and other side products occurring during SOC operation, which will be discussed in Chapter 4. Nevertheless, the multi-phase modeling framework which was developed in context of the present work is highly flexible. It allows for the description of many additional applications. Three exemplary cases from the area of PEFCs (polymer electrolyte fuel cell), lithium-sulfur-batteries (Li-S) and lithium-oxygen-batteries (Li-O) will be discussed in the following. They were developed in collaboration with my co-workers at DLR Stuttgart [8] and represent a direct spin-off of the new model described in the previous sections. Scope of this work was the extensive validation of the modeling framework and its implementation, as well as demonstration of the achieved flexibility.

An overview of the three exemplary systems in comparison to an SOFC anode is given in Figure 20. Illustrated are all phases, phase boundaries and electrochemical reactions participating in secondary-phase formation at one of the electrodes. In all cases the main reaction is taking place at the interface of three or even four different phases. While in SOFCs the main task is to prevent the formation of secondary phases like nickel oxide or solid carbon, operation of PEFCs as well as Li-S and Li-O batteries is even more complex. Here the formation of a liquid or solid secondary phase is a necessary consequence of cell operation. Thus, understanding of the underlying processes is an important task, which can be achieved by means of computational modeling and simulation.

The following sections give a short description of each demonstration model and show exemplary results.

3.6.1 Water management in PEFC

One of the key issues for the functionality of PEFCs is proper water management [115]. On one hand, sufficiently high water content is required for high proton conductivity of the membrane. Insufficient humidification of the inflow gases leads to a drying-out of the membrane, causing an increase in resistance. On the other hand, oxygen transport may be blocked due to high liquid water content at the cathode side (so-called flooding). Focus of this application example is demonstrating the breakdown of fuel cell function caused by flooding.

In PEFCs, liquid water may occur due to two mechanisms: First, it is created by the oxygen reduction reaction at the cathode side,
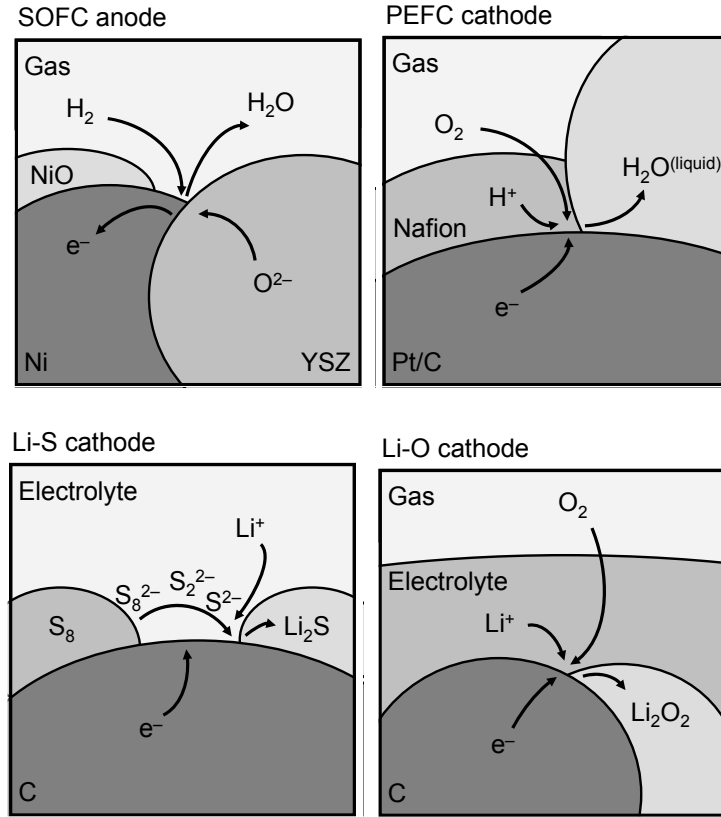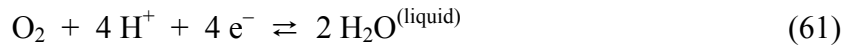
Figure 20. Illustration of multi-phase reactions taking place on the micro-scale during the operation of fuel cells (top) and batteries (bottom).

$$O_2 \ + \ 4\,H^+ \ + \ 4\,e^- \ \rightleftarrows \ 2\,H_2O^{(liquid)} \tag{61}$$

Second, depending on partial pressure and temperature, gaseous water may condensate to liquid water or liquid water may evaporate into the gas phase, respectively, according to

$$H_2O^{(liquid)} \ \rightleftarrows \ H_2O^{(gas)} \ . \tag{62}$$

Furthermore, water is dragged from anode to cathode side via electro-osmosis.

Table 7 (appendix) defines the layers, bulk phases, phase boundaries, species, and reactions used in the PEFC model. The model used here is based on the single-phase PEFC model of Eschenbach et al. [116], which is extended by liquid water formation, as described in the following. The liquid water evaporation rate (Eq. 62) can be described by the Hertz-Knudsen equation [117]

$$R_{H_2O} = \alpha_e \, \frac{p_0(T) - p}{\sqrt{2\pi MRT}} \quad , \tag{63}$$

where α_e is the so-called evaporation coefficient, which strongly depends on the particular

flow situation, p denotes the partial pressure of water, whereas $p_0(T)$ is the temperature dependent saturation pressure.

An empirical relationship is applied to describe the dependence of water volume fraction and the gas-platinum interface in the cathode according to

$$f_{\text{Platinum–Gas}} = \frac{\varepsilon_{\text{gas}}}{\varepsilon_{\text{gas},0} + \varepsilon_{\text{liquid},0}} \quad . \tag{64}$$

Water evaporation/condensation takes place at the vapor/liquid interface. In order to avoid numerical instabilities, which may occur when reaching volume fractions equal to zero, we assume that the boundary vanishes for very low as well as for very high volume fractions $\varepsilon_{\text{liquid}}$, according to

$$f_{\text{Liquid–Gas}} = 1 - \exp(-\xi \varepsilon_{\text{liquid}}) - \exp(\xi(\varepsilon_{\text{liquid}} - \varepsilon_{\text{gas},0} - \varepsilon_{\text{liquid},0})) \quad , \tag{65}$$

with $\xi = 100$.

The model is used to investigate the flooding in the cathode catalyst layer (CL), which occurs due to the mechanisms described above. The increase of liquid water content in the catalyst layer leads to a reduction of the pore space, i.e., lowers the diffusion of oxygen. This eventually causes a breakdown of the cell function. To demonstrate this, we increase the power density within 50 seconds up to 800 W/m^2 and subsequently keep it constant. We consider inlet air with relative humidity RH = 0.3 at temperature $T = 354$ K and pressure $p = 101325$ Pa. The evaporation coefficient is assumed to be $\alpha = 0.01$. Note that in the present simulations we do not include gas diffusion layers or microporous layers, which would alter the flooding behavior.

Figure 21 shows the time evolution of current density and cell voltage. In the first 50 seconds the values change according to the linear increase of the power density. Subsequently the power density is kept constant. However, the volume fraction of liquid water inside the CL increases with time (Figure 22), which leads to a decrease of the cell voltage. In order to keep the power density constant, this drop of the cell voltage is compensated by an increase of the current density. Eventually, at about $t = 168$ s, the cell function breaks down, since the CL is almost completely flooded. Figure 22 shows the spatial distribution of liquid water in the CL at three different points in time. Liquid water is mainly created close to the membrane, where the oxygen-reduction reaction takes place. Furthermore, liquid water is created faster at the inlet of the channel due to the higher oxygen concentration and consequently high local cur-

rent density. At t = 150 s the CL is already highly flooded. Note that a volume fraction of 40 % corresponds to the total available pore space.
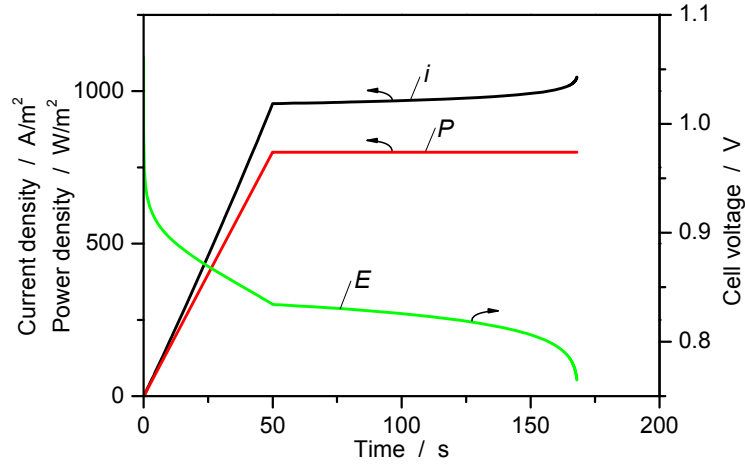

Figure 21. Temporal evolution of power density, current density and cell voltage of a simulated PEFC.
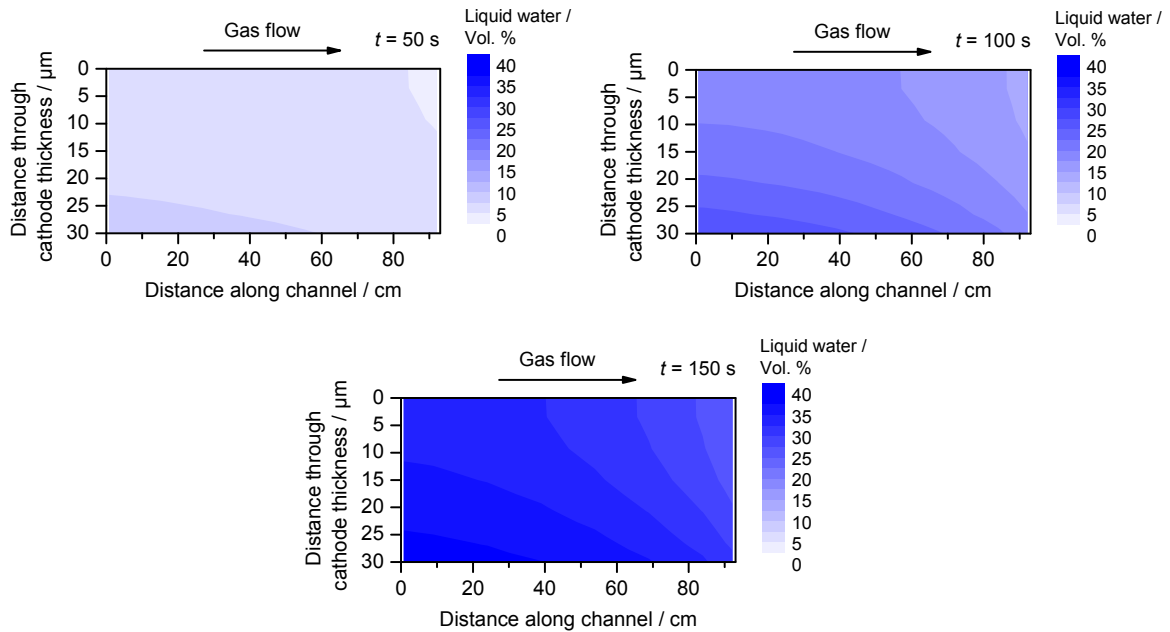

Figure 22. Spatial evolution of liquid water inside the porous PEFC cathode. A volume fraction of 40 % corresponds to the totally available pore space.

63

3.6.2 Lithium-sulfur battery

The lithium-sulfur (Li-S) battery is a promising system for energy storage. Its energy density (up to 2.6 kWh/kg) is the highest of all "closed-system" batteries known. Even though the system has been known for decades [118], recently it gained increasing attention due to the demand for lightweight high-capacity batteries for application in electric vehicles [119].

While the negative electrode of a Li-S cell consists of pure metallic lithium, the positive electrode typically is a compound of finely dispersed sulfur, electronically conducting carbon, and a stabilizing binder [120]. The overall reaction of the Li-S cell can be formulated as

$$S_8 \;+\; 16\,Li \;\rightleftarrows\; 8\,Li_2S \;. \tag{66}$$

Unlike in lithium-ion batteries, where Li atoms are intercalated into various lattice materials, all reactants and products are pure solids. The charge and discharge processes involve the dissolution and precipitation as well as the chemical transformation of these materials. The reaction proceeds over a large number of intermediate sulfur species at different oxidation states, which are partially soluble. The large number and different properties of those intermediates represent a major challenge in understanding Li-S electrochemistry. Several proposed mechanisms for the reduction of sulfur in the Li-S cell have been published [118, 121–123]. The Li-S battery model presented here is based on the work of Kumaresan et al. [121].

Table 8 (appendix) defines the layers, bulk phases, phase boundaries, species and reactions used in the Li-S model. The parameters have been converted from Kumaresan et al. [121]. The model assumes a conversion of metallic lithium and solid sulfur to solid Li_2S via the reaction pathway shown in Table 8. An empirical relationship is used for all solid-electrolyte interfaces in the Li-S cathode according to

$$f_{\text{Solid–Electrolyte}} = \left(\frac{\varepsilon_{\text{solid}}}{\varepsilon_{\text{solid, 0}}} \right)^{1.5} . \tag{67}$$

Galvanostatic discharge was simulated at a current of $0.34\ \text{A}\cdot\text{m}^{-2}$, corresponding to a discharge rate of C/50.

Figure 23 depicts the simulated discharge curve together with the volume fractions of the S_8 and Li_2S phases. From this figure, the two distinct stages of the discharge curve, which are observed in experiment [124], can be explained: During the first stage, solid sulfur is present in the cell and the voltage remains relatively high. In the second stage, when all solid sulfur is

completely dissolved, the voltage drops until it reaches a plateau as soon as solid Li_2S starts to form from dissolved Li^+ and S^{2-} ions. This can be further understood from the concentration variation of the dissolved intermediate species. As long as there is still solid sulfur in the cathode, the concentration of dissolved sulfur $S_8^{(liquid)}$ in the electrolyte remains constant. During this stage, the main reaction taking place is the reduction of $S_8^{(liquid)}$, accompanied by the formation of various polysulfides. Once the reservoir of solid sulfur is used up, the concentrations of $S_8^{(liquid)}$ and subsequently S_8^{2-} and S_6^{2-} start to decrease. The electrical current now results from the reduction of the polysulfides down to S^{2-}, which is removed from the solution by precipitation of Li_2S. Note that, only by including detailed multi-phase management into the model, the typical discharge curve and in particular the minimum between the two stages of the discharge (cf. Figure 23) can be reproduced.
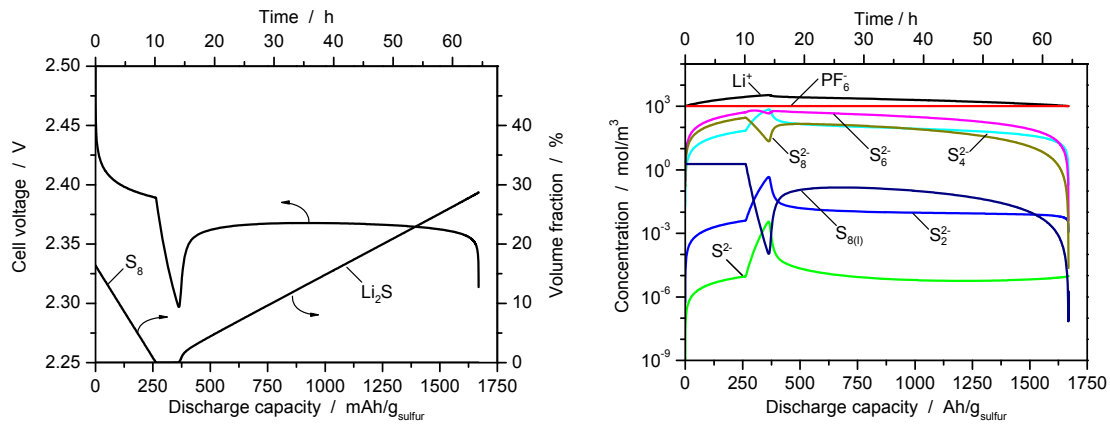

Figure 23. Left: A typical Li-S low current discharge curve alongside with the volume fractions of pure sulfur and Li_2S. Right: Concentrations of ions in the electrolyte during the galvanostatic discharge shown in the left figure.

3.6.3 Lithium-oxygen battery

Li-O batteries receive great attention in the current literature due to their large theoretical energy density (11.9 kWh/kg without the O_2 mass), which is a factor of ~5 above that of conventional Li-ion technology [125]. At the cathode, four bulk phases are involved in the reaction according to

$$2\ Li^{+(electrolyte)}\ +\ O_2^{(gas)}\ +\ 2\ e^{-(carbon)}\ \rightleftarrows\ Li_2O_2^{(solid)}\ . \tag{68}$$
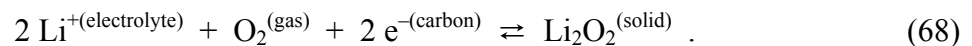
Added catalysts such as MnO_2 may represent a fifth bulk phase. Connected to the multi-phase

management, a long list of issues needs to be solved for Li-O batteries [126]. The formation of solid lithium oxide as product phase can clog pore space and/or form an insulating film on the carbon support. Oxygen solubility and diffusivity are very low in organic electrolytes [127]. Furthermore, standard carbonate-based electrolytes decompose during discharge of Li-O cells [128]. Aqueous electrolytes are interesting alternatives, but their reactivity towards lithium is a major security risk.

Table 9 (appendix) defines the layers, bulk phases, phase boundaries, species, and reactions used in the Li-O model. The model has been converted from Andrei et al. [112], exchanging the electrolyte. Our modeling framework captures solid-phase deposition conveniently: Eq. 53 describes the creation of solid reaction products, Eq. 56 the consecutive change in porosity, i.e., the volume fraction of the electrolyte. The reduction in porosity triggers two effects: The transport speed in the electrolyte is reduced resulting in pore clogging, described by Bruggemann coefficients, and the surface area of the cathodic discharge reaction decreases. This decrease is described based on geometrical considerations, assuming the formation of a surface film in a system of cylindrical pores (Eq. 59) [112]. Other authors assume that a layer of insulating reaction products passivates the cathode surface [129], an effect neglected in the present work.

Figure 24 shows discharge curves for various current densities between 0.1 $A \cdot m^{-2}$ and 1 $A \cdot m^{-2}$. Those comparatively low values were chosen because the low solubility and diffusivity of oxygen in the organic electrolyte limits the performance of the system (cf. below). After an initial drop due to activation and concentration overpotentials, the voltage remains nearly constant for a long period. The discharge capacity is limited by pore clogging due to Li_2O_2 deposition, as discussed in the following.

Figure 25 shows spatial profiles along the cathode thickness. Initially (SoC = 100 %), oxygen concentration and current production are homogeneously distributed in the cathode (Figure 25a/b). Quickly, a steep concentration gradient of oxygen evolves due to its slow transport and low solubility (Figure 25a). Thus, the reaction mainly proceeds at the front of the cathode (Figure 25b). In this region, Li_2O_2, which is deposited during discharge, is concentrated (Figure 25c). Consequently, the volume fraction of the electrolyte-filled pore space decreases in time, especially at the front of the pores. This enhances the problem of slow oxygen transport until the pores are completely blocked (Figure 25c). In Figure 25d we show that inhomogeneities and pore clogging are accelerated at high discharge currents.
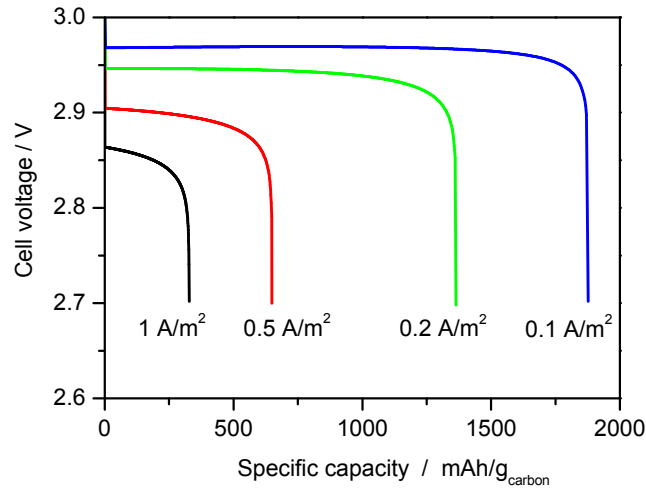
66

Figure 24. Discharge curves of a Li-O battery at various current densities between 0.1 and 1 A/m^2.
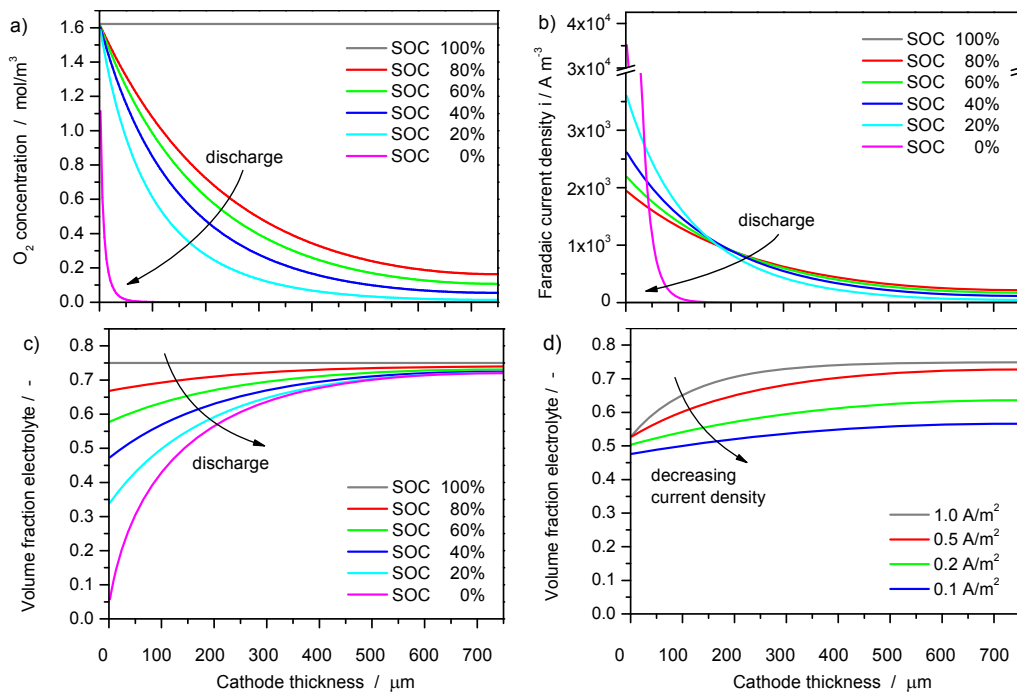

Figure 25. Spatial profiles inside the porous Li-O cathode. a) O$_2$ concentration, b) faradaic current and c) porosity at various SOC, $i = 0.5$ A/m^2. d) Porosity at various current densities and SoC = 50 %.

3.7 Summary and conclusions

Multi-phase management is crucial for both performance and durability of batteries and fuel cells. In this chapter a generic framework for describing the spatiotemporal evolution of gaseous, liquid and solid phases, as well as their interdependence with interfacial (electro-) chemistry and structure in a continuum description was presented. The modeling domain consists of up to seven layers (current collectors, channels, porous electrodes, separator/membrane), each of which can consist of an arbitrary number of bulk phases (gas, liquid, solid) and connecting interfaces (two-phase or multi-phase boundaries). Chemical source terms for global or elementary interfacial reactions are calculated based on mass-action kinetics with potential-dependent kinetic coefficients. Mass and charge transport within bulk phases is described using a 1D+1D+1D approach. The present methodology provides a useful tool for understanding and optimizing multi-phase management in electrochemical cells. Due to its flexibility, it allows rapid, efficient and robust modeling and simulation. The validity and flexibility of the developed framework was demonstrated by three exemplary studies regarding secondary-phase formation in PEFCs, Li-S and Li-O batteries which were developed in collaboration with co-workers at DLR Stuttgart.

4 NICKEL OXIDATION IN SOFC AND SOEC ELECTRODES

4.1 Introduction

This chapter presents a detailed study of nickel oxide formation in solid oxide fuel and electrolyzer cells. Firstly a thermodynamic description of the oxidation process is given. Analytical thermodynamic calculations offer a fast way to roughly estimate the oxidative conditions. Secondly, the SOC model presented in Chapter 3 is used to predict NiO formation based on local conditions inside the electrodes of a cell under operation. The model is parameterized with kinetic data from experimental literature. Results predict for the first time the influence of electrochemical nickel oxidation on the shape of the SOFC polarization curve together with a spatially and temporally resolved insight into the anode. Conditions for NiO formation in SOECs are discussed and safe conditions of SOC operation presented. Finally, the limitations of the model will be discussed.

Results from this chapter have been published in the Journal of the Electrochemical Society [8], submitted to the Journal of Power Sources [9] and presented on four international conferences: 10th European SOFC Forum (EFCF 2012) [130], 10th Symposium on Fuel Cell and Battery Modeling and Experimental Validation (MODVAL 10) [131], Fundamentals & Development of Fuel Cells Conference (FDFC 2013) [76] and 2nd International Conference on Materials for Energy (EnMat II) [132].

4.2   Thermodynamic analysis of nickel oxidation

Like any chemical reaction, nickel oxidation is governed by both thermodynamics and kinetics. This section presents a thermodynamic analysis, which forms the basis for kinetic predictions. Throughout this work we distinguish between thermochemical NiO formation, which is governed by species concentration and temperature, and electrochemical NiO formation, where electric potentials inside the electrode have to be considered additionally (cf. Section 2.3.1).

4.2.1 Thermochemical oxidation

Thermochemical nickel oxidation can be described as reaction of bulk nickel with gaseous oxygen,

$$\text{Ni} + \tfrac{1}{2}\,\text{O}_2 \;\rightleftarrows\; \text{NiO} \;. \tag{69}$$

The equilibrium constant K of the reaction is given by:

$$K = \frac{k_f}{k_r} = \frac{a_{\text{NiO}}}{a_{\text{Ni}}\sqrt{a_{\text{O}_2}}} = \exp\left(-\frac{\Delta G}{RT}\right) \;, \tag{70}$$

where k_f and k_r are forward and reverse reaction rate constant, a_i is the activity of species i, ΔG is the Gibbs energy of formation at standard pressure, R the ideal gas constant and T the temperature. Values for ΔG were obtained using temperature-dependent thermodynamic data for Ni from McBride et al. [24] and for NiO from Holmes et al. [133] (Table 4). Substituting the activity of the solid phases with 1 and the activity of oxygen by its partial pressure $\left(a_{\text{O}_2} = p_{\text{O}_2}/p_0\right)$ allows predicting a limiting p_{O_2}. Below this partial pressure nickel is thermodynamically favored; above nickel oxide formation takes place. Figure 26a shows limiting p_{O_2} as function of operating temperature. Oxidation of nickel takes place at rather low oxygen partial pressures in the range of 10^{-13} to 10^{-7} Pa. With increasing temperature the oxidation limit shifts to higher oxygen partial pressures.

Additionally nickel can be oxidized by water vapor,

$$\text{Ni} + \text{H}_2\text{O} \;\rightleftarrows\; \text{NiO} + \text{H}_2 \;. \tag{71}$$

In this case Equation (70) changes to

70

$$K = \frac{k_f}{k_r} = \frac{a_{\text{NiO}} a_{\text{H}_2}}{a_{\text{Ni}} a_{\text{H}_2\text{O}}} = \exp\left(-\frac{\Delta G}{RT}\right) \quad , \tag{72}$$

which yields a $p_{\text{H}_2}/p_{\text{H}_2\text{O}}$ ratio limiting the formation of NiO. Figure 26b shows the limiting ratio as function of operating temperature. Depending on temperature, nickel oxide formation takes place if the partial pressure of water is 130–230 times larger than the partial pressure of hydrogen. In the case of a H_2/H_2O fueled SOFC this ratio corresponds to a mole fraction $x_{\text{H}_2\text{O}} > 99\,\%$.

Table 4. Thermodynamic data for nickel [24] and nickel oxide [133].

T / K	$h_{,\text{Ni}}$ / J·mol^{-1}	$s_{,\text{Ni}}$ / J·mol^{-1}·K^{-1}	$h_{,\text{NiO}}$ / J·mol^{-1}	$s_{,\text{NiO}}$ / J·mol^{-1}·K^{-1}
900	$1.866 \cdot 10^4$	$6.356 \cdot 10^1$	$-2.022 \cdot 10^5$	$1.021 \cdot 10^2$
950	$2.024 \cdot 10^4$	$6.526 \cdot 10^1$	$-2.006 \cdot 10^5$	$1.037 \cdot 10^2$
1000	$2.184 \cdot 10^4$	$6.691 \cdot 10^1$	$-1.990 \cdot 10^5$	$1.055 \cdot 10^2$
1050	$2.346 \cdot 10^4$	$6.849 \cdot 10^1$	$-1.972 \cdot 10^5$	$1.072 \cdot 10^2$
1100	$2.509 \cdot 10^4$	$7.001 \cdot 10^1$	$-1.952 \cdot 10^5$	$1.090 \cdot 10^2$
1150	$2.675 \cdot 10^4$	$7.148 \cdot 10^1$	$-1.931 \cdot 10^5$	$1.109 \cdot 10^2$
1200	$2.841 \cdot 10^4$	$7.289 \cdot 10^1$	$-1.908 \cdot 10^5$	$1.129 \cdot 10^2$

4.2.2 Electrochemical oxidation

In contrast to thermochemical oxidation, the electrochemical pathway of nickel oxidation involves oxygen ions and a release of electrons into the nickel electrode,

$$\text{Ni} + \text{O}^{2-} \rightleftarrows \text{NiO} + 2\,\text{e}^- \quad . \tag{73}$$

The reaction is driven by the local potential difference $\Delta\phi$ between nickel and the ion-conducting phase. For equilibrium conditions (open circuit voltage, OCV) the limiting cell voltage causing this potential can be calculated by applying the Nernst equation,

$$E = \frac{RT}{4F} \ln\left(\frac{p_{\text{O}_2,\text{ca}}}{p_{\text{O}_2,\text{an}}}\right) \quad , \tag{74}$$

by setting the value for $p_{\text{O}_2,\text{an}}$ from the Ni/NiO equilibrium (Eq. 70). Figure 26c shows limiting cell voltages as function of operating temperature for an assumed oxygen partial pressure of air at the cathode ($p_{\text{O}_2,\text{ca}} = 2.128 \cdot 10^4$ Pa). Results show values around 0.64 to 0.78 V.
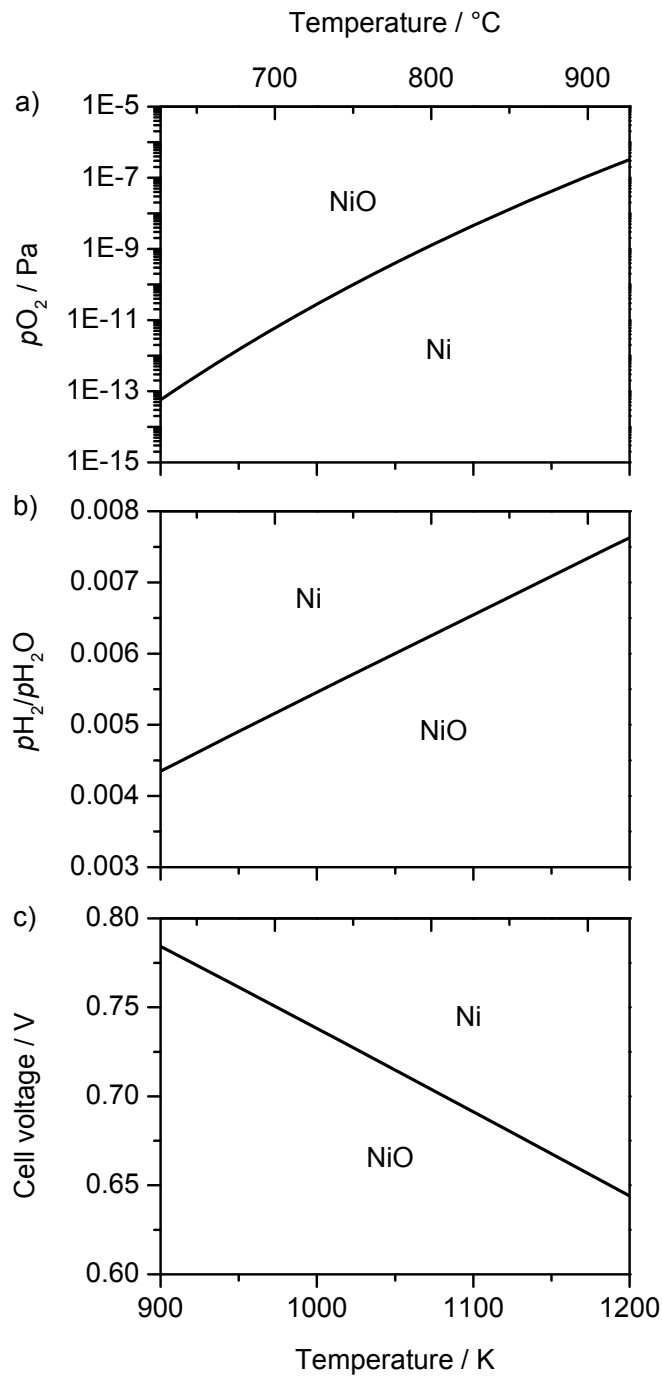
Figure 26. Nickel oxidation regimes predicted from thermodynamics. a) Limiting oxygen partial pressure for O_2-induced chemical NiO formation. b) Limiting hydrogen-to-steam ratio for H_2O-induced chemical NiO formation. c) Limiting cell voltage for electrochemical NiO formation under equilibrium conditions (OCV).

Under cell polarization the conditions for oxidation of nickel get more complex. Figure 27 illustrates the potential gradient building up through the electrolyte and composite electrodes during cell operation. The gradient depends on multiple parameters, for example, ionic con-

ductivity, reaction kinetics, electrolyte and electrode thickness, and microstructure. Furthermore the local potential depends on the effective overpotentials at anode and cathode as well as concentration distributions. Therefore no direct correlation between global cell voltage E and the local potential difference $\Delta\phi$ can be established. Valid predictions of electrochemical nickel oxidation under polarization are only possible by applying a numerical model taking into account the above-mentioned effects.

In the following we use the term local cell voltage (E_{local}) instead of $\Delta\phi$. We define it as the difference between local anode potential step (under operation) and the cathode reference potential step (at OCV conditions),

$$E_{local}(i,x,y) = \Delta\phi_{cathode,OCV} - \Delta\phi_{anode}(i,x,y) \qquad (75)$$

For E_{local} the predictions shown in Figure 26c are valid independently of the global cell voltage.
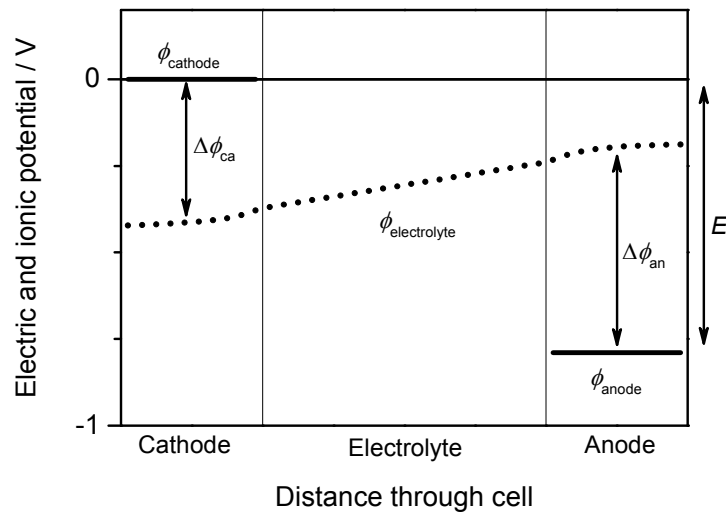

Figure 27. Potential distribution in a polarized solid oxide cell with porous composite electrodes. The electric potential at the cathode is defined as zero.

4.3 Model description and parameterization

Basis for the following simulations is the validated 2D model of a planar SOFC which has been presented previously [107] (cf. Section 3.2). Results are calculated under the assumption of isothermal conditions at $T = 1073$ K and a pressure of 101325 Pa. Surface diffusion is assumed fast, reducing the full 1D+1D+1D model to a 1D+1D model. A summary of all model parameters is given in Table 5. The model includes coupled electrochemistry and transport through the membrane electrode assembly (MEA) and gas channels. Anode electrochemistry is described using elementary kinetics for surface reactions on Ni and YSZ, and for charge transfer (hydrogen spillover) [27]. Cathode electrochemistry is described using a modified Butler-Volmer equation introduced by Zhu and co-workers [29]. The same cell model is applied for SOEC simulations, which we define by a negative current output. The number of control volumes for numerical discretization in x and y dimension is chosen such, that a further increase does not affect the calculated results within 0.5 %. An exemplary simulated IV-curve is shown in Figure 28.
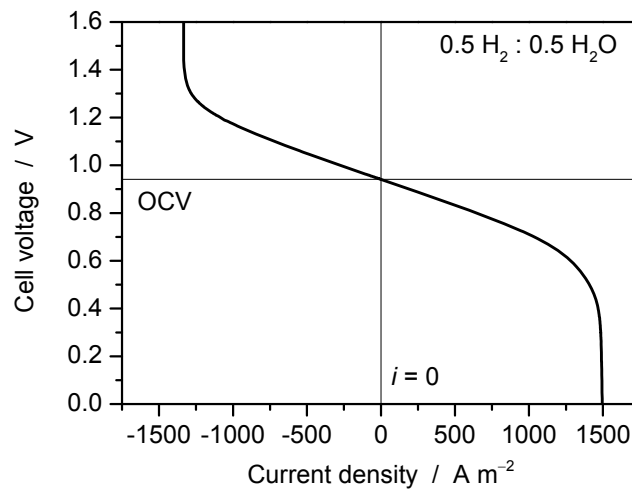

Figure 28. Simulated IV curve using the 2D elementary kinetic model, showing the operation behavior in fuel cell mode and in electrolysis mode. Fuel composition: 50 % H_2–50 % H_2O vs. air, inflow rate: 0.2 slm

For quantifying the evolution of nickel and nickel oxide inside the electrodes, multi-phase management is used (Section 3.4). Each layer (anode, electrolyte, cathode, channels) consists of one or multiple bulk phases as well as reactive surfaces. The layers, phases, surfaces and

74

species, as well as chemical reactions are summarized in Table 5. The volume fractions ε of all phases are calculated as a function of time and spatial location inside the cell by taking into account mass conservation and chemical rate equations. In case of NiO formation a four-phase-system is assumed, consisting of Ni, NiO, YSZ and pore space (gas phase).
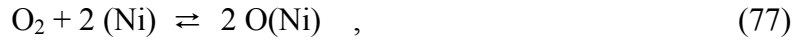
Table 5. Summary of model parameters. The base cell model including elementary reaction kinetics was presented previously by Bessler et al. [107]. Thermodynamics for gas-phase species are taken from McBride et al. [24] as implemented in CANTERA [108]. Reverse reaction coefficients follow from thermodynamic consistency.

Cathode channel	**Length × Width** **CVs**	0.088 × 0.002 m 18 × 1	**Species** O_2 N_2		
Cathode	**Thickness** **CVs**	55 µm 18 × 3			
	Bulk phases LSM YSZ Gas	**Volume fraction** 0.4 0.36 0.24 ($\tau = 2$)	**Species** – YSZ V_{YSZ} O^{2-}_{YSZ} See channel	**Molar enthalpy** – – 0 kJ·mol⁻¹ −236.4 kJ·mol⁻¹	**Molar entropy** – – 0 J·K⁻¹·mol⁻¹ 0 J·K⁻¹·mol⁻¹
	Interfaces LSM-YSZ-Gas	**Specific length** $1.52\cdot10^6$ m·m⁻³	**Reactions** $O_2 + 2\,V_{YSZ} + 4\,e^- \rightleftharpoons 2\,O^{2-}_{YSZ}$	**Preexponential factor** $8.57\cdot10^4$ m⁸·kmol⁻²·s⁻¹	**Activation energy** 125 kJ·mol⁻¹
Electrolyte	**Thickness** **CVs**	10 µm 18 × 8			
	Bulk phases YSZ	**Volume fraction** 1.0	**Species** See cathode		
Anode	**Thickness** **CVs**	540 µm 18 × 28			
	Bulk phases Nickel YSZ Gas Nickel oxide	**Volume fraction** 0.32 0.36 0.32 ($\tau = 8$) $1\cdot10^{-10}$	**Species** Ni ($\rho = 8908$ kg·m⁻³) See cathode See channel NiO ($\rho = 7450$ kg·m⁻³)	**Molar enthalpy** see Table 4 see Table 4	**Molar entropy** see Table 4 see Table 4
	Surfaces Nickel surface YSZ surface		**Species** (Ni) H(Ni) O(Ni) OH(Ni) H₂O(Ni) (YSZ) O²⁻(YSZ) OH⁻(YSZ) H₂O(YSZ)	**Molar enthalpy** 0 kJ·mol⁻¹ −31.81 kJ·mol⁻¹ −221.635 kJ·mol⁻¹ −192.74 kJ·mol⁻¹ −273.215 kJ·mol⁻¹ 0 kJ·mol⁻¹ −236.383 kJ·mol⁻¹ −282.485 kJ·mol⁻¹ −272.982 kJ·mol⁻¹	**Molar entropy** 0 J·K⁻¹mol⁻¹ 40.73 J·K⁻¹mol⁻¹ 38.981 J·K⁻¹mol⁻¹ 106.44 J·K⁻¹mol⁻¹ 130.696 J·K⁻¹mol⁻¹ 0 J·K⁻¹mol⁻¹ 0 J·K⁻¹mol⁻¹ 66.99 J·K⁻¹mol⁻¹ 97.94 J·K⁻¹mol⁻¹
	Interfaces Ni-Gas	**Specific area** $2.25\cdot10^6$ m²·m⁻³	**Reactions** $H_2 + (Ni) + (Ni) \rightleftharpoons H(Ni) + H(Ni)$ $H_2O + (Ni) \rightleftharpoons H_2O(Ni)$ $H(Ni) + O(Ni) \rightleftharpoons OH(Ni) + (Ni)$ $H(Ni) + OH(Ni) \rightleftharpoons H_2O(Ni) + (Ni)$ $H_2O(Ni) + O(Ni) \rightleftharpoons OH(Ni) + OH(Ni)$ $O_2 + (Ni) + (Ni) \rightleftharpoons O(Ni) + O(Ni)$	**Preexponential factor** $9.8\cdot10^{13}$ m⁵·kmol⁻²·s⁻¹ $1.4\cdot10^7$ m³·kmol⁻¹·s⁻¹ $5\cdot10^{21}$ m²·kmol⁻¹·s⁻¹ $3\cdot10^{19}$ m²·kmol⁻¹·s⁻¹ $5.4\cdot10^{22}$ m²·kmol⁻¹·s⁻¹ 0.01 (sticking coeff.)	**Activation energy** 0 kJ·mol⁻¹ 0 kJ·mol⁻¹ 97.9 kJ·mol⁻¹ 42.7 kJ·mol⁻¹ 209.37 kJ·mol⁻¹ 0 kJ·mol⁻¹
	YSZ-Gas	$1.10\cdot10^6$ m²·m⁻³	$(YSZ) + O^{2-}_{YSZ} \rightleftharpoons O^{2-}(YSZ) + V_{YSZ}$ $H_2O + (YSZ) \rightleftharpoons H_2O(YSZ)$ $H_2O(YSZ) + O^{2-}(YSZ) \rightleftharpoons OH^-(YSZ) + OH^-(YSZ)$	$1.6\cdot10^{19}$ m³·kmol⁻¹·s⁻¹ $6.6\cdot10^8$ m³·kmol⁻¹·s⁻¹ $1.6\cdot10^{21}$ m²·kmol⁻¹·s⁻¹	91 kJ·mol⁻¹ 0 kJ·mol⁻¹ 9.647 kJ·mol⁻¹
	Ni-YSZ-Gas	$3.96\cdot10^{12}$ m·m⁻³	$H(Ni) + OH^-(YSZ) \rightleftharpoons H_2O(YSZ) + (Ni) + e^-$	$2.0\cdot10^{17}$ m·kmol⁻¹·s⁻¹	235 kJ·mol⁻¹
	Ni-NiO-Gas	$2.25\cdot10^6$ m·m⁻³	$Ni + O(Ni) \rightleftharpoons NiO + (Ni)$	$2.7\cdot10^3$ m⁴·kmol⁻¹·s⁻¹	144 kJ·mol⁻¹
	Ni-NiO-YSZ	$3.82\cdot10^5$ m·m⁻²	$Ni + O^{2-}_{YSZ} \rightleftharpoons NiO + V_{YSZ} + 2\,e^-$	$4\cdot10^{-7}$ m⁴·kmol⁻¹·s⁻¹	144 kJ·mol⁻¹
Anode channel	**Length × Width** **CVs**	0.088 × 0.002 m 18 × 1	**Species** H_2 N_2 O_2 H_2O		

Thermochemical oxidation of nickel is implemented in the model as elementary-kinetic reaction of bulk nickel with oxygen atoms adsorbed on the Ni surface. Thus the oxidation pathways by molecular oxygen and by water vapor can be covered by one reversible NiO formation reaction,
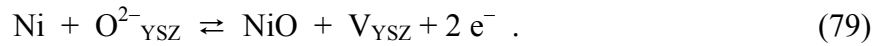
$$\text{Ni} + \text{O(Ni)} \rightleftharpoons \text{NiO} + \text{(Ni)} , \tag{76}$$
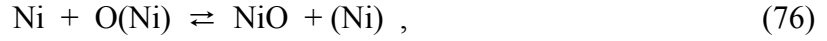
where surface-adsorbed oxygen atoms O(Ni) originate from either gas-phase O_2,

$$O_2 + 2\,\text{(Ni)} \rightleftharpoons 2\,\text{O(Ni)} , \tag{77}$$

or from gas-phase H_2O in multiple steps,

$$H_2O + 3\,\text{(Ni)} \rightleftharpoons \text{H(Ni)} + \text{OH(Ni)} + \text{(Ni)} \rightleftharpoons 2\,\text{H(Ni)} + \text{O(Ni)} . \tag{78}$$

Electrochemical oxidation is described by a global reaction at the interface between the nickel and YSZ bulk phases,

$$\text{Ni} + \text{O}^{2-}_{\text{YSZ}} \rightleftharpoons \text{NiO} + \text{V}_{\text{YSZ}} + 2\,\text{e}^- . \tag{79}$$

Results are presented and discussed in terms of the degree of oxidation (DOO), which is defined as ratio of nickel oxide volume over the total Ni and NiO volume,

$$\text{DOO} = \frac{\varepsilon_{\text{NiO}}}{\varepsilon_{\text{Ni}} + \varepsilon_{\text{NiO}}} . \tag{80}$$

4.3.1 Feedback on structural parameters

In the continuum model described above (Chapter 3), microstructural features are described via homogenized quantities, that is, specific interfacial area between two bulk phases A^{V} (in m^2/m^3) and specific TPB length between three bulk phases l^{V} (in m/m^3). These values change upon the formation of solid nickel oxide due to microstructure modifications.

In the present model, scaling functions are applied to the continuum parameters in order to account for microstructural changes. For the length of the electrochemically active TPB of the anode ($l^{\text{V}}_{\text{Ni-YSZ-Gas}}$) an empirical exponential function is used. At a DOO of 1 % a reduction of TPB by a factor of 10 is assumed,

$$l^{\text{V}}_{\text{Ni-YSZ-Gas}} = l^{\text{V}}_{\text{Ni-YSZ-Gas},0} \cdot \exp\left(-2.3 \cdot \text{DOO}\right) \cdot f_{\text{num}} \tag{81}$$

where a subscript $_0$ denotes the initial TPB length. f_{num} is an additional term required for im-

proving numerical stability if the volume fraction of an bulk phase approaches zero (cf. Section 3.5). Regarding the phase formation/dissolution process during conversion from nickel to nickel oxide, the following function is applied, as illustrated in Figure 29,

$$f_{num} = 1 - abs(\tanh(10^9 \cdot \varepsilon_{NiO}) - \tanh(10^9 \cdot \varepsilon_{Ni})) \qquad (82)$$

In addition to a change of interfacial areas, formed NiO will expand into the free pore space and therefore affect gas-phase transport. This feedback mechanism of NiO formation on cell performance is implicitly included in the model via the effective diffusivity of gas-phase species,

$$D_i^{eff} = \frac{\varepsilon_{Gas}}{\tau_{Gas}^2} D_i \qquad (83)$$

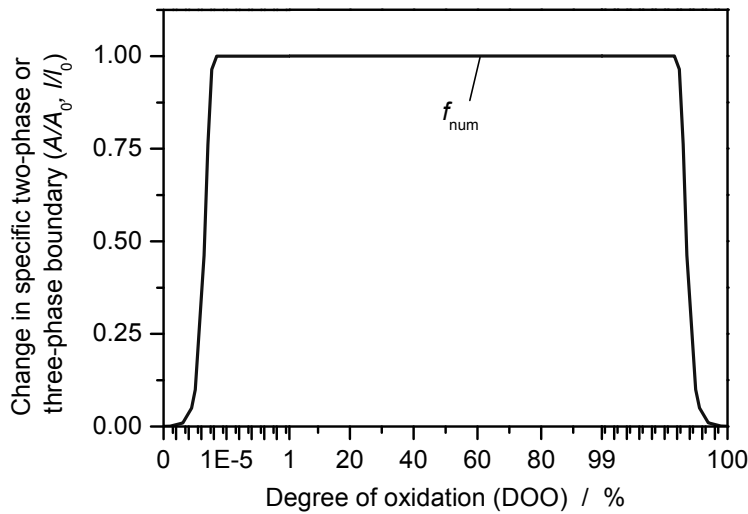where D_i describes the diffusion coefficient of species i and τ the tortuosity.

Figure 29. Effect of numerical stability function on interface size, expressed as change in specific two-phase or three-phase boundary, as function of degree of oxidation.

4.3.2 Determination of reaction kinetics

The base model (cf. Section 3.2) has been parameterized and validated before [107]. It represents the performance of an anode-supported SOFC. We parameterize the kinetic data for thermochemical and electrochemical nickel oxidation (Eqs. 76 and 79) by using literature

experiments. Since the rates of the backward reactions follow from thermodynamics (Eq. 44), it is sufficient to obtain the preexponential factor k_0^f and the activation energy E_f^{act} of the forward reactions. Sarantaridis and Atkinson [39] report a value of 144 ± 15 kJ mol^{-1} for the activation energy of nickel oxidation. Lacking more data, we apply this value to both oxidation reactions. The k_0^f values are obtained by fitting to measurements by Hagen et al. [134] and Wang et al. [53] as described in the following. Measured data and simulations for *thermochemical* oxidation and reduction are shown in Figure 30 and for *electrochemical* oxidation in Figure 31.
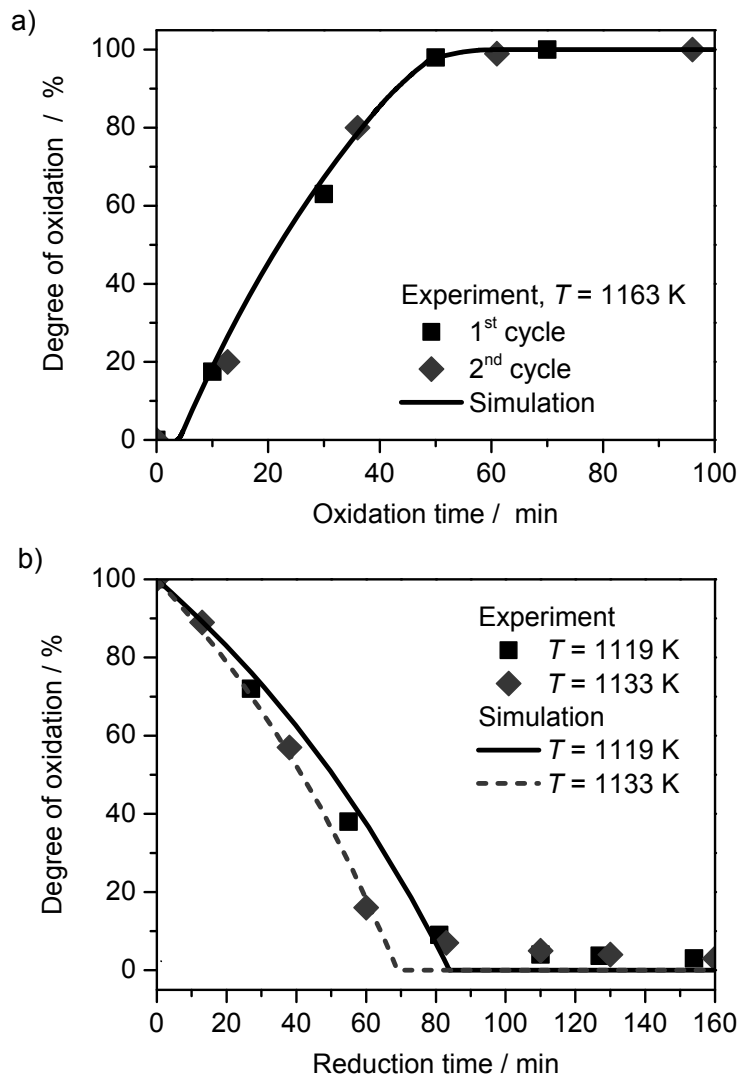

Figure 30. a) Simulated oxidation dynamics of bulk nickel in air at 1163 K compared to experimental data of Hagen et al. [134]. Model kinetic parameters (forward reaction) are fitted to match the experiment. b) Reduction dynamics of bulk nickel oxide in Helium containing 4 % H_2 at 1119 K (first cycle) and 1133 K (second cycle) [134].

Hagen et al. [134] conducted a zero-current experiment of an SOFC with two consecutive reduction–oxidation cycles. This experiment is suitable to parameterize the *thermochemical* reaction rate parameters (Eq. 76), as electrochemical oxidation is assumed to be disabled when no current load is applied. The authors used an anode supported cell with a Ni/YSZ anode of 360 μm thickness and a porosity of approximately 30 %. The temperature was set to 1163 K during the oxidation steps and to 1119 K and 1133 K during the first and second reduction steps, respectively. The oxidation steps were performed with air at a flow rate of 5 $l \cdot h^{-1}$. The reduction steps were performed with helium containing 4 % hydrogen at a flow rate of 4 $l \cdot h^{-1}$. The preexponential factor of thermochemical Ni oxidation was adjusted in order to fit simulations to experiments, resulting in a value of $2.7 \cdot 10^3$ $m^4 \cdot kmol^{-1} \cdot s^{-1}$. Simulated data for oxidation was shifted by 3.4 minutes because the initially lower reaction kinetics as measured by Hagen (s-shaped curve) could not be reproduced by the present model.
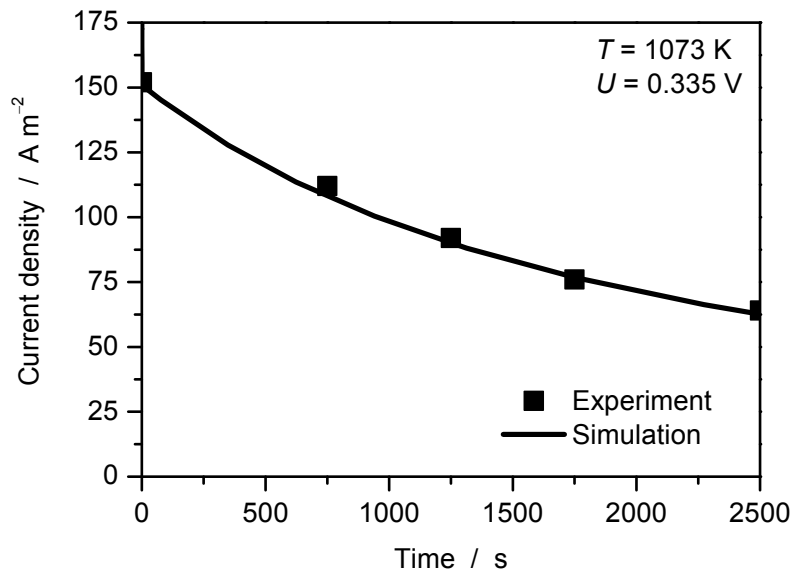

Figure 31. Simulated dynamics of electrochemical nickel oxidation compared to experiments by Wang et al. [53] under nitrogen atmosphere with a fixed voltage of 0.335 V at 1073 K. Model kinetic parameters and reduction of the active surface area between Ni and YSZ are fitted to match the experiment.

Kinetics of the *electrochemical* nickel oxidation was obtained from an SOFC experiment by Wang et al. [53]. During continuous potentiostatic operation the hydrogen fuel was replaced with pure nitrogen. This disables the hydrogen oxidation reaction, and the measured current is

assumed to be due to electrochemical oxidation of nickel only (Eq. 79). The experiment was performed at 1073 K with a fixed voltage of 0.335 V. The preexponential factor of electrochemical nickel oxidation was determined to be $4 \cdot 10^{-7}$ $m^4 \cdot kmol^{-1} \cdot s^{-1}$. To reproduce the slope of the experiment the model had to be modified by an additional function which describes the interdependence between NiO volume fraction and the active surface area between nickel and YSZ ($A^V_{\text{Ni-NiO-YSZ}}$). Good agreement could be obtained by applying an exponential function,

$$A^V_{\text{Ni-NiO-YSZ}} = A^V_{\text{Ni-NiO-YSZ,0}} \cdot \exp(-50 \cdot \varepsilon_{\text{NiO}}) \cdot f_{\text{num}} \tag{84}$$
,

which is also used in all following simulations.

The feedback between nickel oxide formation and on the triple-phase-boundary length $l^V_{\text{Ni-YSZ-Gas}}$ (Eq. 81) and on the active surface between nickel and YSZ $A^V_{\text{Ni-NiO-YSZ}}$ (Eq. 84) is plotted in Figure 32. Both functions cause a strong decrease in size of active interface, followed by a reduction of electrochemical rates (Eqs. 54−55).
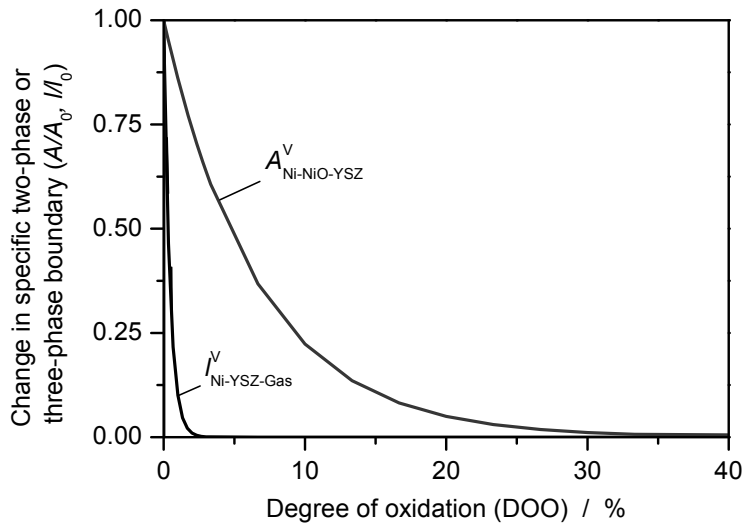

Figure 32. Feedback of NiO formation on the triple-phase-boundary length $l^V_{\text{Ni-YSZ-Gas}}$ (Eq. 81) and on the active surface between nickel and YSZ $A^V_{\text{Ni-NiO-YSZ}}$ (Eq. 84).

4.4 Nickel oxide formation in SOFC

4.4.1 Oxidation due to air leakage

Exposure to air at SOFC operation temperature is a fatal incident due to resulting reoxidation of the anode. It can be caused, e.g., by leakage of the fuel supply system or from the cathode side due to cell cracks (cf. Section 2.3.1). Figure 33 shows the formation of nickel oxide inside a porous Ni/YSZ anode with inflow of air at a temperature of 1153 K. Data corresponds to the parameterization simulation shown in Figure 30a.
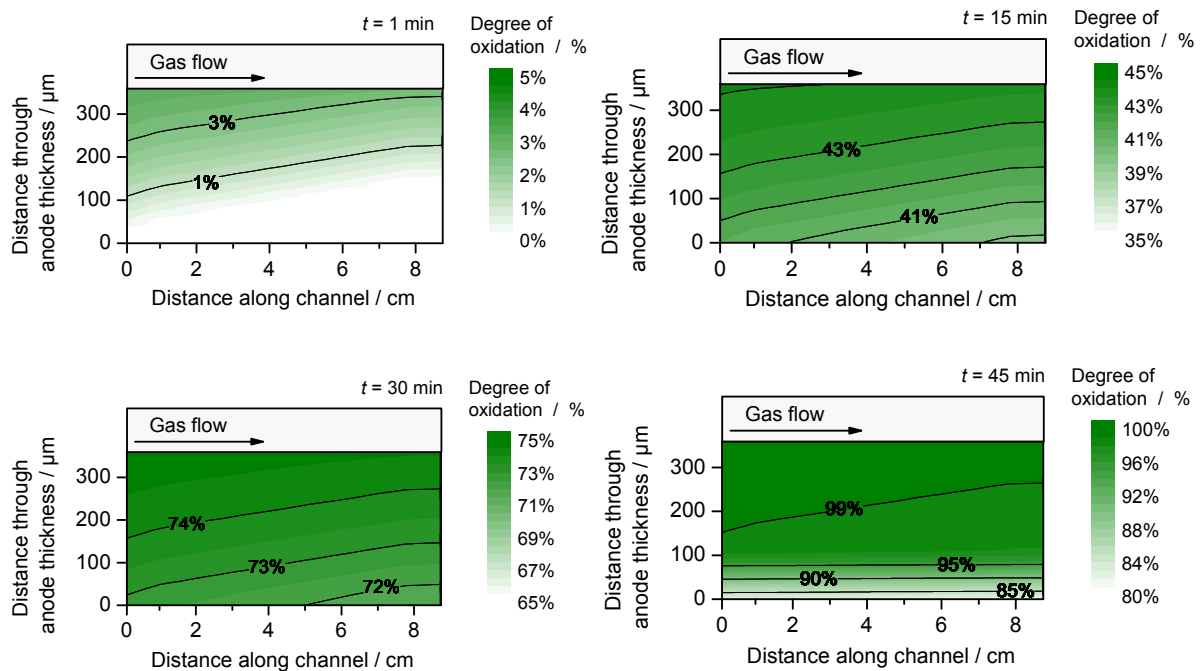

Figure 33. Spatial evolution of DOO inside the porous anode of an SOFC for four different times during exposure to air at $T = 1173$ K. The data corresponds to the simulation shown in Figure 30a. Note that the scale for DOO is changing to allow a clear visual representation in the range between 1 % and 100 %.

The spatial distribution of NiO is shown for four points of time, which correspond to the beginning ($t = 1$ min), the intermediate region ($t = 15$ min and $t = 30$ min), and the end ($t = 45$ min) of the oxidation process. NiO formation starts at the gas inlet. Here the highest DOO is observed. Parts of the electrode close to the electrolyte layer are less oxidized. After 1 min about half of the anode shows a degree of oxidation > 1 %. This indicates that a large part of

the nickel phase is already covered by a thin layer of NiO. Nevertheless, the electrochemically active area, which is located in the first 50 to 100 μm from the electrolyte, is not yet affected. Thus, no permanent damage should appear after this exposure time. After 15 min the picture has changed dramatically. Throughout the electrode a minimum DOO of 39 % is reached. With this amount of NiO present, the active triple-phase boundary is largely blocked and no more hydrogen reduction is possible. With a DOO up to 45 % close to the channel the probability of permanent cell damage is high. After 30 min the DOO throughout the anode has risen linearly. The degree of oxidation is between 70 and 80 %. After 45 min nearly the complete nickel phase is oxidized. Close to the electrolyte the DOO has grown less, due to slow oxygen transport through the very small remaining pore space.

4.4.2 Oxidation under potentiostatic operation

Figure 34 shows simulation results for NiO formation under low-voltage potentiostatic SOFC operation. Plotted are the temporal evolution of current density and the average NiO volume fraction for a voltage variation over 12 h operating time, with a fuel gas composition of 10 % H_2 and 90 % H_2O. Starting at $t = 0$, the voltage is linearly reduced from OCV down to 0.34 V within 1 h (black line). At this level it is held for 11 h. As expected, lowering the voltage leads to an increase of current density (blue line). The blue dotted line, which holds a constant level between 1 and 12 hours, shows the simulated current density without considering Ni oxidation. NiO volume fraction (green line) starts to increase from $t = 0.6$ h until it reaches a maximum value of after about 10.5 h. Ni oxidation is delayed relative to the voltage variation; with the parameters used in the present study, it occurs on a time scale of around 10 hours. Ni oxidation leads to a reduction of current density which is due to the combined effects of three-phase boundary length reduction and porosity decrease. Under the presently assumed operating conditions with low fuel utilization (40 %), the nickel oxide volume fraction does not increase above 1.6 Vol.-%.

The spatially resolved evolution of NiO volume fraction inside the porous anode during the voltage variation is shown in Figure 35. Three time points are chosen, which correspond to the beginning ($t = 1$ h), the intermediate region ($t = 3$ h), and the end ($t = 10$ h) of the oxidation process. The simulations show that NiO formation starts close to the solid electrolyte at the gas outlet side. In the following hours it spreads through the anode, increases concentration and finally develops the highest values close to the solid electrolyte at the gas outlet side.
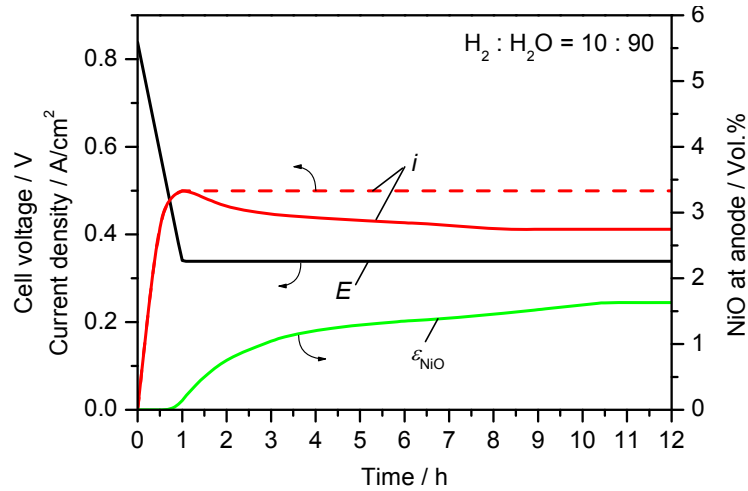
Figure 34: Formation of nickel oxide in a SOFC during polarization down to low voltages in highly humidified fuel gas.
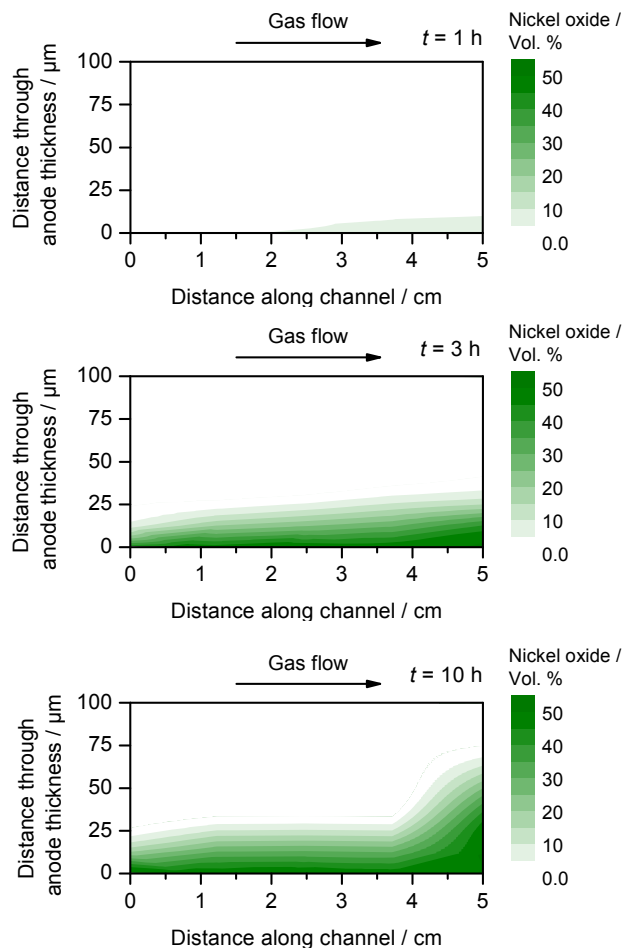

Figure 35: Spatial evolution of NiO inside the porous anode corresponding to the simulation shown in Figure 34. A volume fraction of 51 % corresponds to the maximum available pore space.

4.4.3 Oxidation due to high fuel utilization

The cell operation state (in terms of fuel utilization and cell voltage) and NiO formation/reduction chemistry mutually influence each other. We have studied our virtual SOFC single cell at high fuel utilization (FU) in order to analyze this behavior. Figure 36 shows the results of a simulated load cycle. The current density was linearly increased from zero to 1,500 $A \cdot m^{-2}$ and decreased back to OCV within a total simulation time of 1 h. Inlet fuel flow and maximum current density were chosen such that the FU reaches nearly 100 % at high current density. Reference simulations excluding NiO formation mechanisms (Figure 36a, black dashed line) show the expected behavior: After an extended polarization range with approximately linear correlation between voltage and current, the cell voltage breaks down at a limiting current density of ca. 1,360 $A \cdot m^{-2}$, because full fuel utilization is reached (Figure 36a, point of interest 1). The demand target of 1,500 $A \cdot m^{-2}$ cannot be reached under these conditions. Simulations including anode reoxidation (both electrochemical and thermochemical mechanisms) show a different behavior (Figure 36a, red solid line). In the range of linear operation, behavior is unchanged. At a current density above ca. 1,200 $A \cdot m^{-2}$ the FU reaches values close to 100 % and the cell voltage starts to break down. However, beyond a current density of 1300 $A \cdot m^{-2}$ (ca. 0.50 V) the voltage stabilizes again, forming a second plateau. This point represents the onset of Ni oxidation, marked by the starting increase of the DOO (Figure 36a, green solid line). The voltage continues decreasing down to 0.38 V until the demand target of 1,500 $A \cdot m^{-2}$ is reached. During the 3.8 minutes between start of the oxidation process and maximum current about 1 % of the nickel gets oxidized. With subsequently decreasing current the DOO at first keeps rising until the cell voltage reaches a value of 0.38 V ($i = 1230$ $A \cdot m^{-2}$). Here, the DOO reaches its maximum of 2.4 %. From this point NiO is slowly reduced back to nickel. During the virtual experiment, the cell voltage shows a pronounced hysteresis. The polarization/depolarization curves fall together only after the anode is completely reduced again. Note, that the presented model does not include irreversible performance degradation.

The same data are shown as function of time in Figure 36b. As soon as fuel utilization reaches values close to 100 % (Figure 36b, blue line), nickel gets oxidized. However, even during subsequent Ni reduction, fuel utilization keeps staying close to 100 %. This is due to the fact that all hydrogen available is consumed by the nickel reduction reaction (Eq. 71). Once the anode is fully reduced, the FU value recovers quickly.
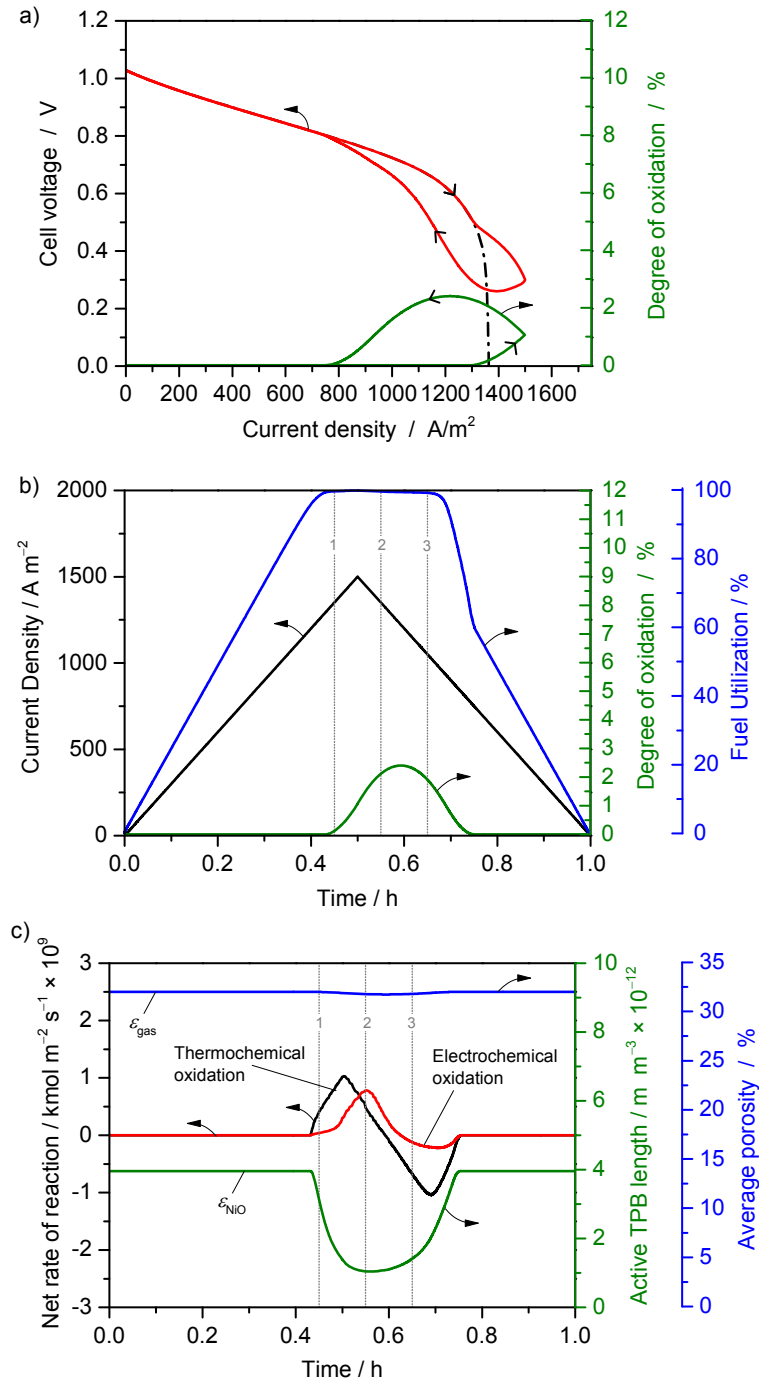
Figure 36. Simulation of nickel oxide formation and reduction in an SOFC under current cycling. Fuel composition: 46.5 % H_2–7 % H_2O–46.5 % N_2 vs. air, inflow velocity: 0.2 slm. a) Polarization curve showing the hysteretic effect caused by NiO formation. The black dashed line shows simulations where Ni oxidation was switched off. b) Current density, degree of oxidation and fuel utilization versus time for the same simulation run. Dotted lines indicate points of interest (POI) at $t = 0.45$ h, $t = 0.55$ h and $t = 0.65$ h. c) Net rates of reaction for thermochemical ($Ni + H_2O \rightarrow NiO + H_2$) and electrochemical ($Ni + O^{2-} \rightarrow NiO + 2\,e^-$) oxidation of nickel, together with average active TPB length and average porosity versus time.

The physical model allows a more detailed insight into the processes taking place during this cycle. Figure 36c shows the net rates of reaction of the thermochemical and the electrochemical nickel oxidation reactions together with the active triple phase boundary length and average porosity. Data is averaged over the complete anode volume. The simulations show that oxidation of the anode is initiated by the thermochemical reaction pathway. Rates for thermochemical oxidation have a peak at around 0.5 h, which corresponds to the point of maximum current density. With decreasing current density the rate decreases and turns to negative values at about 0.6 h (peak of DOO). The thermochemical reaction is also the main pathway during NiO reduction to nickel. The electrochemical oxidation reaction plays a minor role in the initial stage of the oxidation process, but the rate increases significantly at about 0.5 h and reaches a maximum value at 0.54 h (point of interest 2). This corresponds to the point of minimum cell voltage. At 0.6 h we find the situation where the electrode is subject to electrochemical oxidation but thermochemical reduction. Beyond 0.66 h (point of interest 3), electrochemical reaction rate gets negative and electrochemical reduction of nickel occurs. Active TPB length and porosity are correlated to the degree of oxidation. Simulations show that the TPB is decreasing significantly down to a minimum value of about $1 \cdot 10^{-12}$ m·m^{-3}, corresponding to a reduction of the initial value by 75 %. In contrast, the effect of nickel oxidation on porosity in the shown data is only minor. Average porosity is reduced about 1 % at its minimum peak.

Plotting spatially resolved data of the SOFC anode at different points of time reveals where oxidation and reduction of nickel (oxide) take place. Figure 37 shows degree of oxidation, local hydrogen-to-steam ratio and local voltage (Eq. 75) for three times during the IV-curve simulations, as marked in Figure 36. Contour lines indicate the thermodynamically predicted limits for thermochemical (middle row) and electrochemical (lower row) nickel oxidation. In the top row both border contours are plotted to simplify comparison with the actual DOO.

The left column diagrams of Figure 37 ($t = 0.45$ h) represent the beginning of the oxidation process. Oxidation starts close to electrolyte and channel outlet (upper panel). This is where the smallest p_{H_2}/p_{H_2O} ratios (middle panel) and lowest local voltages (lower panel) occur. A low DOO of about 0.1 % is present in about the half of the electrode volume. Contours for thermochemical and electrochemical oxidation are nearly identical. They are present about 1 cm ahead of the oxidized area, indicating finite oxidation kinetics.

Six minutes later ($t = 0.55$ h, middle column) the DOO has strongly increased. More than 3 % NiO has formed within a large part of the anode. The strongest oxidation with a DOO > 3.4 %

is located close to electrolyte and channel outlet. The oxidized area corresponds roughly to the thermodynamic limits (contours), which are similar for both reaction pathways. The local voltage in the second half of the cell has decreased significantly, indicating that the oxidation process is strongly driven by the potential. This is in agreement with the average reaction rates shown in Figure 36c (peak of electrochemical oxidation rate at point of interest 2).

The right column shows a point where NiO reduction is taking place ($t = 0.65$ h). The DOO gradient has become steeper, with higher DOOs up to 4 %, extending into a smaller electrode volume as compared to $t = 0.55$ h. Both, p_{H_2}/p_{H_2O} ratio and local voltage have risen above the thermodynamic oxidation limit. Reduction starts in the region close to the channel inlet where the highest hydrogen-to-steam ratio and the highest local voltages appear. It is mainly driven by the thermochemical reaction pathway (NiO reduction by H_2), corresponding to the reaction rates plotted in Figure 36c.
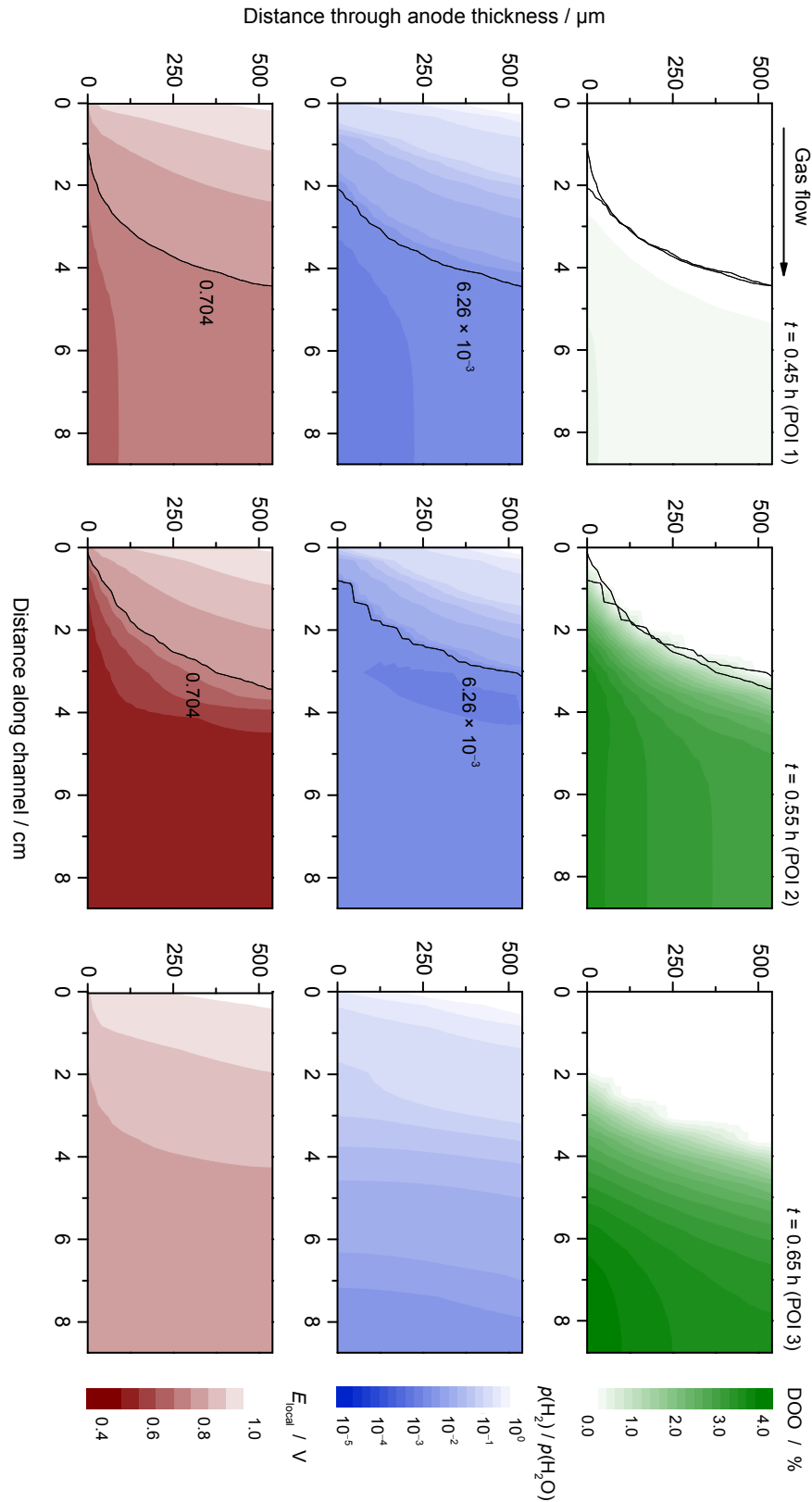
Figure 37. Spatial evolution of degree of oxidation, fuel-to-steam ratio p_{H_2}/p_{H_2O}, and local cell voltage inside the porous anode for three different points of interest (POI) corresponding to the simulations shown in Figure 36. Solid contour lines indicate the oxidation limits as given by thermodynamics (Eq. 72 and Eq. 74).

4.5   Nickel oxide formation in SOEC

Based on the thermodynamic calculations presented in Section 4.2, the formation of nickel oxide in electrolysis mode turns out to be rather unlikely: During operation of the cell there is a constant production of hydrogen and consumption of water, which prevents reaching critical H_2-to-H_2O ratios for thermochemical oxidation. In addition, during electrolysis, the cell voltage is always above OCV. Therefore undershooting the critical voltage for electrochemical oxidation is not possible (cf. Figure 26c).

To verify this thermodynamic analysis a simulation under worst-case conditions is shown in Figure 38, which is a cell fueled by pure water vapor. The simulation starts from a fully reduced fuel electrode. At $t = 0$ the fuel is switched from pure nitrogen to 100 % H_2O, while at the same time a constant current of $-1{,}500$ A·m^{-2} is applied. Feeding pure steam quickly initiates oxidation of the cathode. The DOO keeps rising for about 100 h until a steady-state value of 3.2 % is reached. Voltage stabilizes at 1.03 V.
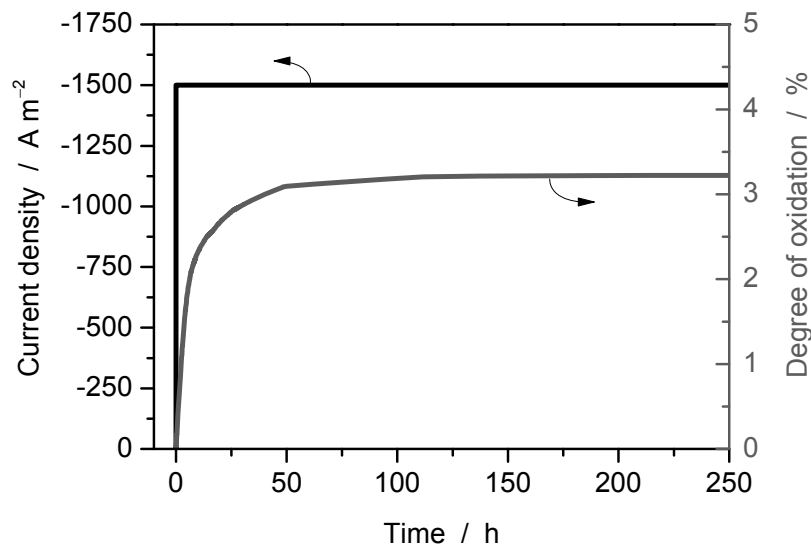

Figure 38. Simulation of nickel oxide formation in an SOEC under constant-current operation. At $t = 0$ the fuel is switched from pure nitrogen to 100 % steam (inflow velocity: 10 slm), and current is switched on. Cell voltage adjusts to a constant value of 1.03 V within the first seconds of simulation (not shown).

A spatial analysis at steady state is plotted in Figure 39. It reveals that the part of the cathode close to the steam inlet is completely oxidized due to thermochemical oxidation (Eq. 78), according to the contour of critical p_{H_2}/p_{H_2O} ratio. Formation of NiO takes place although the local voltages are above the thermodynamic limit. This indicates that thermochemical oxidation dominates over electrochemical reduction (note, that the indicated overshoot of DOO over the contour of critical H_2-to-H_2O ratio is a numerical inaccuracy due to control volume resolution).
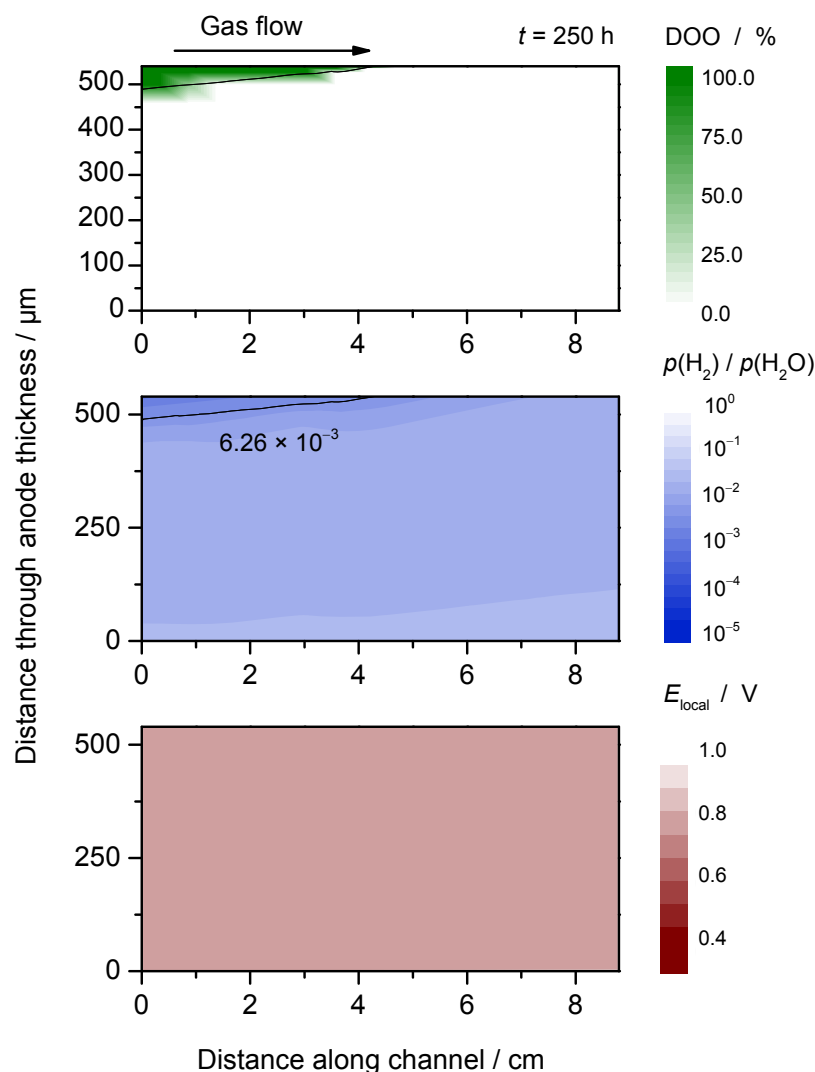

Figure 39. Spatial evolution of degree of oxidation, fuel-to-steam ratio p_{H_2}/p_{H_2O}, and local cell voltage inside the porous SOEC cathode at $t = 250$ h corresponding to the simulation shown in Figure 38. Contour lines indicate the oxidation limits as given by thermodynamics for thermochemical oxidation (limit for electrochemical oxidation not crossed).

Throughout the largest volume of the electrode no NiO is present due to constant production of hydrogen. The results demonstrate that during electrolysis even under low current load and 100 % H_2O a sufficient amount of hydrogen is produced to prevent a further oxidation of nickel.

However, results change dramatically if current density is below a critical value. Figure 40 shows the evolution of degree of oxidation for different current densities from $-1{,}500$ $A \cdot m^{-2}$ down to -500 $A \cdot m^{-2}$. Decreasing the current supply strongly increases the formation of NiO, since the production of hydrogen, which prevents oxidation of the electrode, is proportional to the applied current density. While at current densities of $-1{,}500$ $A \cdot m^{-2}$ and $-1{,}000$ $A \cdot m^{-2}$ only a DOO of about 2 % or 7 % is reached after 100 h of operation, it gets up to a value of 14 % for $i = -750$ $A \cdot m^{-2}$ and even close to 28 % for $i = -500$ $A \cdot m^{-2}$.
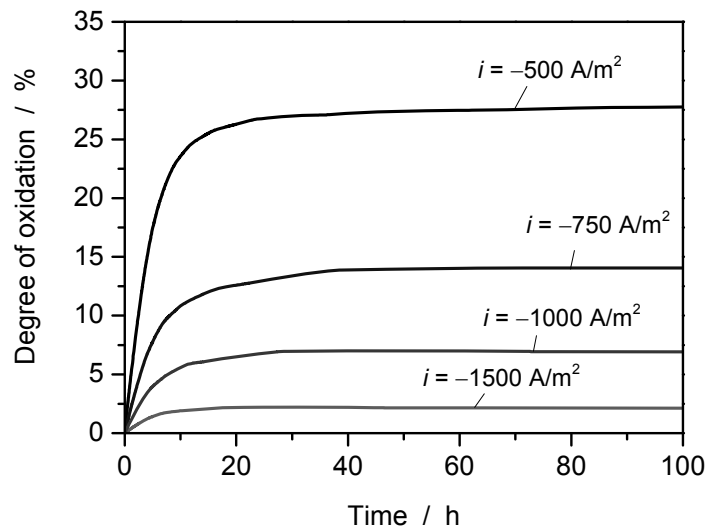
Figure 40. Simulation of nickel oxide formation in an SOEC under constant-current operation for different current densities. At $t = 0$ the fuel is switched from pure nitrogen to 100 % steam and current is switched on.

Further simulations shown in Figure 41 reveal that adding a small amount of hydrogen to the inlet gas completely prevents the electrode from reoxidation. At an applied current density of $-1{,}500$ $A \cdot m^{-2}$ already 0.5 % H_2 in 99.5% of steam reduce the maximum DOO from 2.2 % to 8.5×10^{-4} %. Addition of 1 % H_2 completely prevents formation of nickel oxide in SOEC operation (curve not visible in the figure). This is consistent with the thermodynamic calculations shown in Section 4.2.1.

Note that results in Figure 40 and Figure 41 are simulated with a reduced discretization mesh (7 instead of 18 control volumes for discretization in *x*-direction), to decrease calculation time from 100 h to 8 h per parameter set.

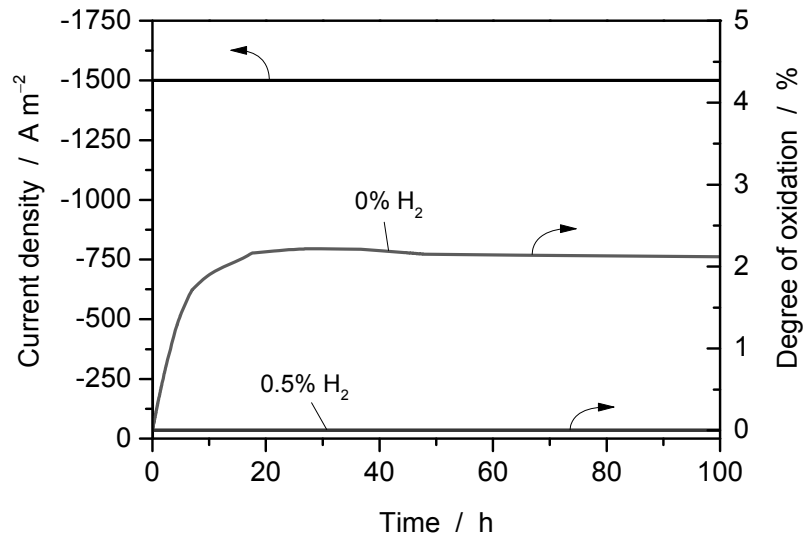Figure 41. Effect of hydrogen addition on nickel oxide formation in an SOEC under constant-current operation. At *t* = 0 the fuel is switched from pure nitrogen to 100 % steam or a mixture of steam and hydrogen and current is switched on.

4.6 Prediction of safe operation points

4.6.1 Local conditions

The previous sections have revealed a complex and in some cases opposite interdependence of thermochemical and electrochemical oxidation pathways. Following thermodynamic considerations a plot showing 'safe' and 'unsafe' conditions with respect to nickel oxide formation can be developed, as shown in Figure 42. Based on the local fuel-to-steam ratio (LFSR = p_{H_2}/p_{H_2O}) and the local cell voltage (E_{local}, Eq. 75), four distinct regimes (quadrants) can be distinguished: (1) Upper right quadrant: LFSR > $6.26 \cdot 10^{-3}$, E_{local} > 0.704 V, both electrochemical and thermochemical reduction; (2) lower right quadrant: LFSR > $6.26 \cdot 10^{-3}$, E_{local} < 0.704 V, electrochemical oxidation but thermochemical reduction; (3) upper left quadrant: LFSR < $6.26 \cdot 10^{-3}$, E_{local} > 0.704 V, thermochemical oxidation but electrochemical reduction; and (4) lower left quadrant: LFSR < $6.26 \cdot 10^{-3}$, E_{local} < 0.704 V, thermo- and electrochemical oxidation. The absolute numbers depend on temperature; here they are given for 1073 K. Under thermodynamic equilibrium at OCV, regimes 2 and 3 are not accessible for thermodynamic consistency reasons. However, during operation, kinetic effects play an important if not dominant role, and the local state can access regimes 2 or 3. The Ni oxidation behavior for these cases is particularly interesting.

In order to further illustrate and discuss this behavior, we have filled the diagram with data points from the fuel cell and electrolysis simulations shown before (Figures 7–9). Each data point represents the conditions at a local position inside the fuel electrode. For the SOFC, data from the three points of interest (t = 0.45 h, 0.55 h, 0.65 h) are included; for the SOEC, data from the steady state (t = 250 h) are taken. Red triangles represent a DOO > 10^{-4} ('unsafe' conditions), while black squares represent a DOO < 10^{-4} ('safe' conditions). The following behavior is observed.

1) In the upper right quadrant (electrochemical and thermochemical reduction) most data points show no NiO. The data points that do show NiO all correspond to point of interest 3 (t = 0.65 h), that is, a condition during NiO reduction. This demonstrates that reduction kinetics are slow, such that oxidized regions remain even if operation returns to reducing conditions. This is in agreement with the 2D data shown in Figure 37.

2) In the lower right quadrant (electrochemical oxidation and thermochemical reduction)

all available data points show reduced states. This indicates that electrochemical oxidation has a slower kinetics than thermochemical reduction, the latter therefore dominating the behavior.

3) In the upper left quadrant (electrochemical reduction and thermochemical oxidation) all data points originate from the SOEC. All conditions show an oxidized state and correspond to the oxidized spatial area shown in Figure 39. Again, this indicates that thermochemical oxidation dominates electrochemical reduction.

4) In the lower left quadrant (electrochemical and thermochemical oxidation) all data points show an oxidized state. This demonstrates that oxidation kinetics are fast, such that even under transient operation (point of interest 1: cell has just entered oxidizing conditions) the behavior is governed through thermodynamics.
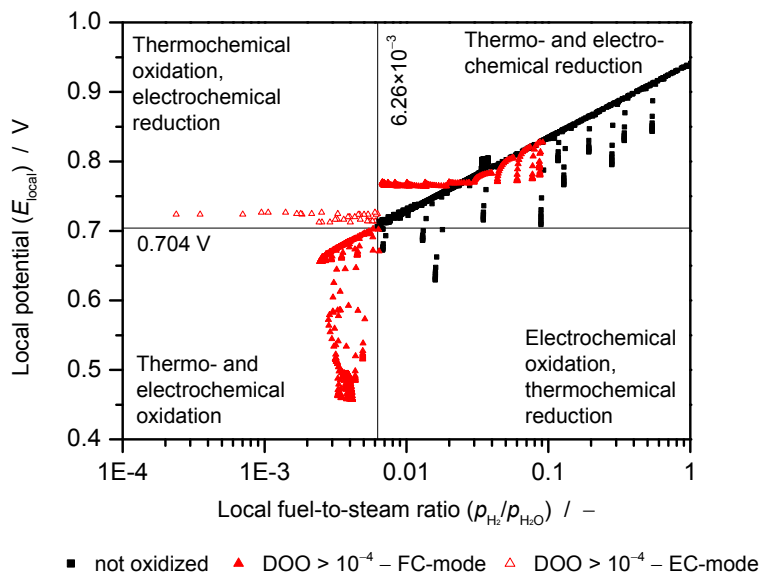
Figure 42. The four regimes of NiO formation as function of local operating conditions for T = 1073 K. Data points show local conditions inside the fuel electrode from simulations shown in Figure 6 (POI 1–3) and Figure 8 ($t = 250$ h); red triangles indicate a local DOO > 10^{-4}.

4.6.2 Global conditions

The analysis presented in the previous section was based on local electrode conditions (E_{local}, LFSR). However, local data are not available during experimental cell operation. It is therefore important to relate NiO formation propensity to available global conditions, that is, cell voltage and fuel utilization. Figure 43 plots a simulated map of 'safe' and 'unsafe' operation

points with respect to the global parameters cell voltage and fuel utilization. The plot shows the same quadrant structure as discussed above.

The data represented by symbols were obtained from several simulated polarization curves at different inflow velocities. Each data point shows quasi steady-state operation conditions (equilibration time of 10^9 s). Black squares indicate that no nickel oxide is formed inside the electrode. If a global DOO $> 10^{-4}$ is present this is represented by a red triangle. Results show that cell operation far below the thermodynamically limiting voltage of 0.704 V, even down to 0 V, is possible without reoxidation as long as the fuel utilization is low. Under the conditions studied, NiO formation only takes place for a FU above ca. 95 % for all cell voltages down to 0 V. At cell voltages above 0.6 V, operation up to the thermodynamic limit of FU = 99.4 % is possible.
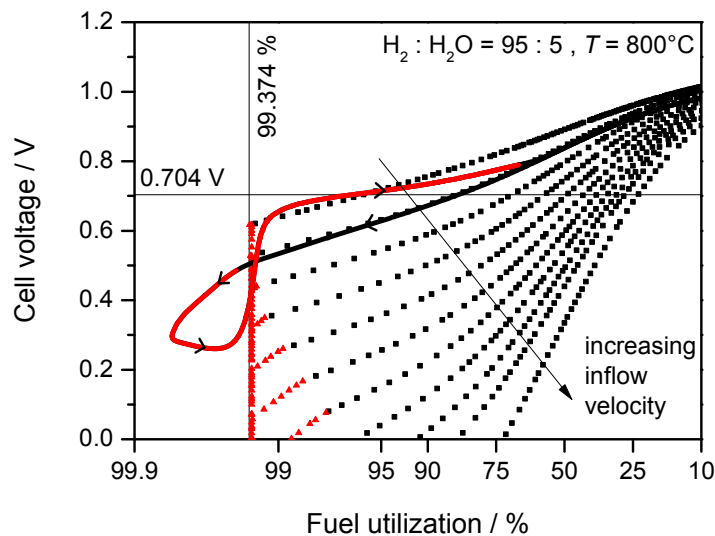
Figure 43. The four regimes of NiO formation as function of global operating conditions. Data points show results from a set of polarization curves with different inflow velocities. Red triangles indicate a reoxidation of the anode. The solid line represents the data from the dynamic load cycle shown in Figure 36.

Additionally, Figure 43 shows a solid line which represents the dynamic behavior during the virtual experiment shown in Figure 36. Starting from OCV, nickel remains reduced within the complete regime 2 (thermochemical reduction, electrochemical oxidation). Oxidation quickly occurs as soon as the state enters regime 4 (thermochemical and electrochemical oxidation),

indicating fast oxidation kinetics. During depolarization back towards OCV, the electrode remains oxidized far into regime 1 (thermochemical and electrochemical reduction), indicating slow reduction kinetics.

The results show again that nickel oxidation is governed by the thermochemical rather than the electrochemical mechanism. However, it should be kept in mind that no general prediction of 'safe' operation conditions based on global parameters is possible. The data shown here is only valid for the simulated SOFC with the parameters given in Table 5.

4.7 Simulation of irreversible degradation

Anode reoxidation can cause irreversible performance degradation of the cell. This is mainly due to changes in microstructure [40]. During each oxidation or reduction process the Ni/NiO phases reorganize because of the changing bulk volume and an associated sintering process. Ivers-Tiffée et al. [49] report measurements of the feedback between redox cycling and degradation for two types of fuel cells. Results show that the effect on cell performance depends on multiple parameters like type of the cell, electrode porosity, operation temperature and degree of oxidation (cf. Section 2.3.1). In addition to microstructural reconfiguration the mechanical stresses inside the anode during nickel oxide formation can cause electrode extension and cracking of the electrolyte [46, 99]. Here, the principle capability of reproducing an irreversible impact caused by changes in the microstructure of the nickel composite electrode shall be demonstrated.

4.7.1 Modeling and parameterization

For simplification the cell model presented in Section 4.3 is reduced to 1D, that is, only gas transport through the electrodes is considered, while channel flow is neglected (cf. Section 3.2.1). Microstructural reconfiguration of the nickel phase is described by introduction of a new bulk phase denoted 'unconnected nickel'. This new phase has same physical properties as nickel, but is not connected to the electrochemically active nickel network. Thus, the formation of 'unconnected nickel' causes a decrease of active nickel volume, causing a decrease of active nickel surface area and of active three-phase boundary length. Here, identical linear relationships between the volume fraction of unconnected nickel and the decrease in active surface area and active TPB length are assumed,

$$A_{\text{Nickel\_surface}}^{\text{V}} = A_{\text{Nickel\_surface},0}^{\text{V}} \cdot \left(1 - \frac{\varepsilon_{\text{Nickel\_unconnected}}}{\varepsilon_{\text{Nickel},0}} \right) , \tag{85}$$

$$l_{\text{Ni-YSZ-Gas}}^{\text{V}} = l_{\text{Ni-YSZ-Gas}}^{\text{V}} \cdot \left(1 - \frac{\varepsilon_{\text{Nickel\_unconnected}}}{\varepsilon_{\text{Nickel},0}} \right) . \tag{86}$$

We further assume that the formation of 'nickel unconnected' only occurs during reduction of nickel oxide, because this process implies a volume reduction and therefore strong microstructural reconfiguration [40]. Additionally, the changes in microstructure are assumed to be irreversible. Thus, the following irreversible chemical reaction is applied in parallel to the

reversible nickel oxidation reactions (Eqs. 26−27),

$$NiO + H_2 \rightarrow Ni\_unconnected + H_2O \ . \tag{87}$$
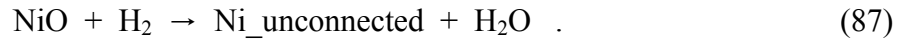
The amount of nickel oxide converted to unconnected nickel phase during reduction is governed through the kinetics of reaction 87. This value depends strongly on the original microstructure of the cell [49]. For the present study the rate is set to $k_f = 5 \times 10^{-8}$ m^4 kmol^{-1} s^{-1} and the activation energy assumed as $E_{act} = 0$.

4.7.2 Results and discussion

Figure 44 shows simulated irreversible cell degradation during three consecutive redox cycles. In each cycle the electrode is exposed to air for 100 minutes ($xO_2 = 0.21$, $xN_2 = 0.79$), followed by exposure to hydrogen containing atmosphere ($xH_2 = 0.03$, $xN_2 = 0.97$). Plotted are the volume fractions of nickel (black line), nickel oxide (green line) and 'unconnected nickel' (purple line) together with the active nickel surface area (blue dotted line) versus time. The first oxidation period takes about 50 min until the electrode is completely oxidized. During reduction nickel and 'unconnected nickel' phase form simultaneously. Since 'unconnected nickel' is formed by an irreversible reaction, its volume fraction is increasing during the following two redox cycles. In consequence the amount of active nickel phase decreases and the active nickel surface area is reduced irreversibly. After the third redox cycle active nickel surface area and active TPB length have decreased by 37 %.

Figure 45 shows results for a similar simulation with reduced air exposure times of 10 min in each reoxidation cycle. In this time span about 22 % of nickel in the electrode are converted to NiO. Consecutively less amount of 'unconnected nickel' is formed. After three redox cycles active nickel surface area and active TPB length have decreased by 10 %.

Due to the modeled reduction in three-phase boundary length, the feedback of redox cycling on electrochemical cell performance can be simulated. For example, the power of an SOFC is a function of the TPB length. Thus, the decrease in active TPB length as shown in Figure 44 and Figure 45 will cause the same trend of decreasing power density, as measured by Ivers-Tiffée et al. (cf. Figure 8) [49].
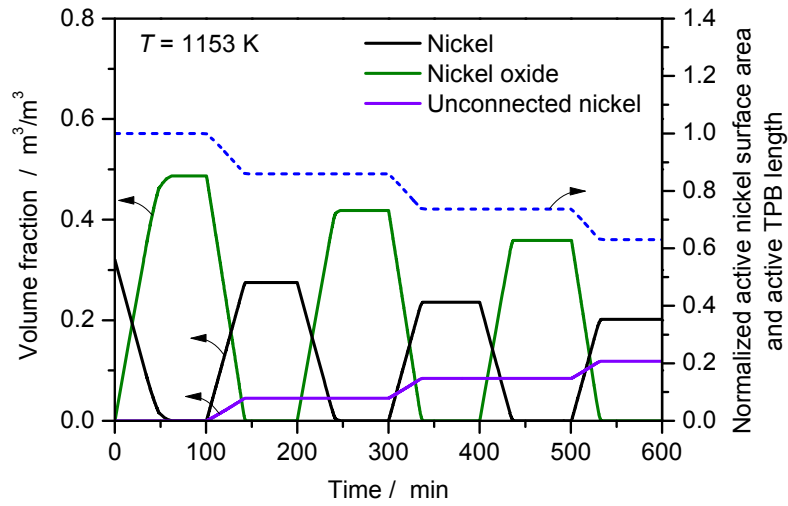
Figure 44. Simulation of irreversible degradation during redox cycling by loss of active nickel surface area and active TPB length. Oxidation is caused by anode exposure to air for 100 min.
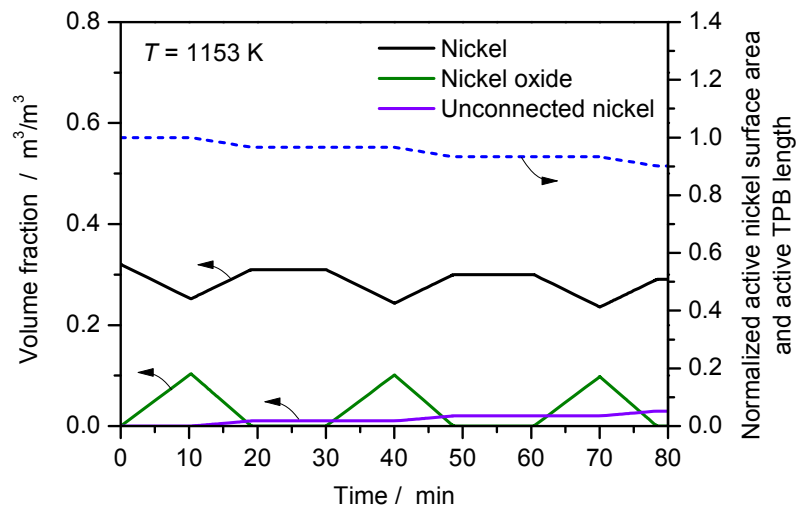

Figure 45. Simulation of irreversible degradation during redox cycling with anode exposure to air for 10 min.

4.8 Model limitations

The results presented in this chapter are based on a number of assumptions, which may influence the predictions and therefore the conclusions with respect to 'safe' and 'unsafe' cell operation. Two main sources of uncertainty can be distinguished, firstly the accuracy of input parameters, and secondly the model assumptions themselves.

Concerning the input parameters, main properties governing the Ni oxidation behavior are the thermodynamics of Ni and NiO. The experimental data used in the present work [24, 133] are comparatively old and furthermore may not necessarily represent the type of Ni/NiO present in SOCs. Particularly, thermodynamics depend on morphology (due to the influence of surface tension). Accurate experimental determination of relevant materials and morphologies would be desirable.

Kinetic data for thermochemical and electrochemical Ni oxidation were obtained by fitting to experimental literature data. Especially regarding the kinetics of electrochemical NiO formation, only a very limited number of studies are available to date. Improving the experimental database would help to further support this study.

Concerning the model, an important simplification is the continuum assumption, that is, no microstructural resolution. All feedback on microstructure is combined into an empirical expression describing the reduction of active TPB length (cf. Eq. 81). Note that, although microstructure-resolved simulations would give further insights into Ni oxidation, due to their high computational expense they do not allow the study of 2D macroscopic cell behavior.

Finally, possible side reactions of nickel, as the formation of volatile nickel compounds like nickel hydroxide [48, 62], and the poisoning with impurities from the gas phase like arsenic and phosphorus [65], are not included in the model. Nickel is simulated as a perfect conductor (no Ohmic losses) which is not affected by oxidation. Simulations are conducted isothermal, whereas the oxidation of nickel depends on the local temperature of the cell (cf. Figure 26).

4.9 Summary and Conclusions

Formation of nickel oxide inside the electrodes is a severe mechanism affecting the lifetime of solid oxide fuel cells (SOFC) and solid oxide electrolyzer cells (SOEC). In this chapter a detailed analysis of Ni oxidation and NiO reduction, as well as the impact on cell performance, based on thermodynamic and 2D kinetic models was presented.

Kinetically, thermochemical and electrochemical reaction pathways can be distinguished. Both reaction pathways were implemented into a validated 2D elementary kinetic model of an anode-supported SOC. Reaction kinetics were parameterized with experimental data from literature. The model allows calculating concentration and potential gradients inside the electrodes, as well as the resulting formation and dissolution dynamics of a bulk nickel oxide phase. Feedback of NiO presence on cell performance is modeled via a decrease of active TPB length and via reduced gas-phase diffusivity due to the solid volume expansion during oxidation. Simulations allow the prediction of local and global conditions for safe and unsafe cell operation regarding nickel oxide formation.

Under SOFC operation, simulation results have shown an onset of Ni oxidation at high fuel utilization. It leads to in the occurrence of a second plateau and a pronounced hysteresis in the polarization curve. Spatially and temporally resolved data show the local evolution of nickel oxide and the limits for oxidation inside the anode. Under SOEC operation, the formation of NiO is unlikely due to high cell voltages and the production of hydrogen. Simulations do show a region of oxidized electrode upon cell operation with 100 % steam, depending on current density. Adding 1 % hydrogen to steam already completely prevents electrode reoxidation.

Additionally, a model for irreversible degradation upon redox cycling based on microstructural changes was developed. It allows the prediction of performance losses of an SOC which undergoes total or partial reoxidation. Since the rate of degradation is strongly dependent on the type of electrode and its microstructure, no general parameterization of the degradation rate is possible. However, the principle applicability of the model could be successfully demonstrated.

Main limitations of the presented models are the simplified feedback of NiO formation on electrode microstructure and the exclusion of side reactions.

5 DETAILED MODELING OF NICKEL OXIDE FILM GROWTH

5.1 Introduction

To obtain a more fundamental understanding on oxidation kinetics as well as on microstructural effects of NiO formation an additional model has been developed. It describes the growth of nickel oxide as a thin film at the interface between nickel and the adjacent bulk phase (gas phase or YSZ). The model assumes that the oxidation rate is controlled by transport of ions and vacancies across the film. Model predictions agree well with a literature experimental measurement of oxidation-layer growth.

Model and results presented in this chapter are under preparation for submission to the 13th International Symposium on Solid Oxide Fuel Cells (SOFC-XIII) [10]. Publication of a full length paper is planned for Autumn/Winter 2013.

5.2 Modeling and simulation methodology

5.2.1 Computational domain

Figure 46 illustrates the basic layout of the computational domain. Nickel oxide is modeled as flat film in one Cartesian dimension z. The film has two interfaces, where chemical and/or electrochemical reactions with the adjacent phases (e.g., bulk Ni, gas phase or YSZ) take place. Inside the film species transport is described via diffusion and migration.

Using a multi-scale approach, the film model is integrated into a 1D+1D continuum model of a single solid oxide cell (x and y dimensions, Sections 3.2−3.4). Specifically, individual 1D film domains are included into every grid point of the macroscopic model, giving rise to an overall 1D+1D+1D multi-scale model. For the results presented here, only one grid point is used on the macro-scale. That is, transport of gaseous species in channels and porous electrodes are ignored. This allows focusing on the effect of a given gas-phase composition or an applied potential on growth of the nickel oxide film, while still allowing for realistic boundary conditions.

The number of control volumes for numerical discretization in x, y and z dimension is chosen such, that a further increase does not affect the calculated results within 0.5 %.
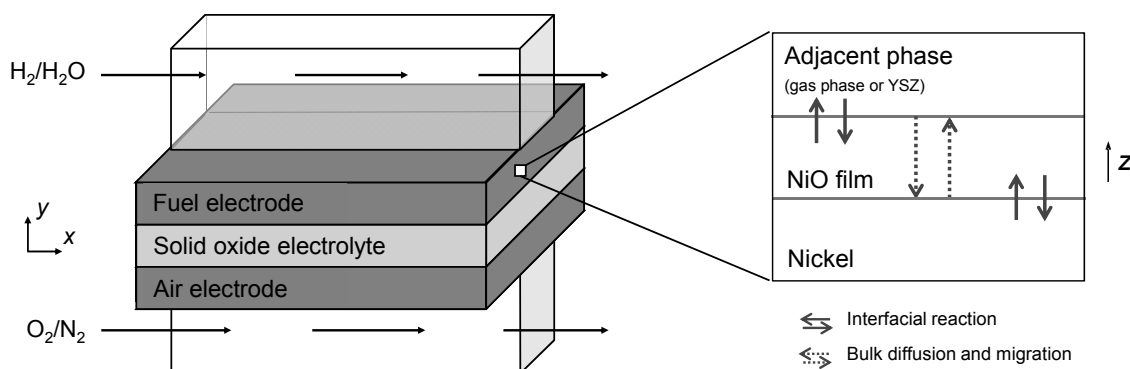

Figure 46. Illustration of the modeling domain for description of NiO growth, consisting of a 1D+1D model of an SOC and a coupled 1D model of the nickel oxide film.

5.2.2 Film model

Growth of the film phase is controlled by transport of charged species inside the film. Fundamental work on this topic has been published by Wagner in 1933 [135], who described the growth of a metal oxide by transport of ions inside the thickening film. A detailed review is provided by Atkinson [136]. More recently, Yu et al. described the transport inside NiO by first-principle calculations [47]. It is agreed that the (thermochemical) growth of NiO over a wide range of temperatures is governed by vacancy diffusion of doubly-charged nickel ions (Ni^{2+}). It is accompanied by diffusion of electrons for maintenance of local charge neutrality [136]. Additionally, the diffusion of oxygen interstitials (O^{2-}) can take place. Measurements by Chevalier et al. show that for temperatures > 1073 K the O^{2-} and Ni^{2+} diffusion coefficients have a similar magnitude [137].

We apply the Nernst-Planck equation for evaluation of the species concentrations over time,

$$\frac{\partial c_i}{\partial t} = \nabla \cdot \left(D_i \nabla c_i + \frac{z_i c_i D_i F}{RT} \nabla \phi \right) \quad , \tag{88}$$

with concentration c_i, diffusion coefficient D_i and charge number z_i of species i. ϕ, F, R and T denote electrical potential, Faraday's constant, ideal gas constant and temperature, respectively. Local electrical charge neutrality (EN) is assumed and introduced as additional governing equation,

$$\sum z_i c_i = 0 \tag{89}$$
.

Boundary conditions for the transport equation are given by the species fluxes through the interfaces, which can be expressed in terms of chemical rates,

$$J_i \big|_x = \dot{s}_{i,\text{interface}} \quad , \tag{90}$$

where $\dot{s}_{i,\text{interphase}}$ (in mol·m^{-2}·s^{-1}) is the heterogeneous molar production rate of species i at the interface. Boundary conditions for the electric potential ϕ follow from the net production rates of electrons $\dot{s}_{\text{electron}}$ due to interfacial electrochemical reactions, which depend on the potential difference between the adjacent phases.

The changes in volume fraction of the film phase and the adjacent phases are quantified by a multi-phase modeling approach, which was described above (Section 3.4). The latter is solving for the volume fractions $\varepsilon(t, x, y)$ of all phases inside the cell as a function of time and

spatial location, by taking into account the chemical rate laws of all involved reactions and mass conservation (continuum approach). As a consequence, the thickness of the film δ can be described as function of its volume fraction,

$$\delta = \frac{\varepsilon_{\text{film}}}{A^{\text{V}}}$$ (91)

,

where A^{V} is the volumetric surface area of the film interfaces. Both interfaces are assumed to have the same area.

5.2.3 Parameterization

For reliable prediction of nickel oxide film growth the model has to be parameterized properly. For all species inside the film, thermodynamic properties (molar enthalpies and entropies) and diffusion coefficients are required, as well as the kinetic coefficients (preexponential factors, activation energies, symmetry factors) of (electro-)chemical reactions between NiO and the adjacent phases (nickel, gas-phase and YSZ). A summary of all film model parameters is given in Table 6.

Three mobile species are assumed in the film. Doubly-charged nickel ions (Ni^{2+}) are known to be the main species governing the growth of NiO during thermochemical oxidation [136]. The transport mechanism is vacancy diffusion, allowed by the non-stoichiometric structure of NiO (strictly $Ni_{1-y}O$) [138]. The transport of Ni^{2+} is accompanied by electrons (e^-) for maintenance of local charge neutrality [136]. The third species that can contribute in NiO film growth are doubly-charged oxygen ions (O^{2-}). Their transport can be described by interstitial diffusion through the bulk [139]. Alternatively, oxygen transport can occur along grain boundaries or via micro-cracks in the non-uniform NiO structure [137] (not included in the present model).

While thermodynamic data and diffusion coefficients are known from literature, the reactions at the interfaces between nickel oxide and nickel (NiO/Ni), nickel oxide and gas phase (NiO/gas) and nickel oxide and YSZ (NiO/YSZ) can only be assumed. (1) Reactions at the interface NiO/Ni are assumed identical for the thermochemical and the electrochemical oxidation process. Eq. 92 describes the transition of nickel atoms from the bulk material into the film. During this process the Ni is oxidized to Ni^{2+}, releasing two electrons. With Eq. 93 the formation of bulk NiO is described by the bonding of nickel and oxygen ions. This reaction is assumed to be possible at all interfaces of NiO and reappears in Eq. 96 and Eq. 99. Finally,

Eq. 94 creates an electrochemically coupling between nickel and nickel oxide phase by the possibility of electron transfer between both phases (boundary condition for ϕ in Eq. 88). (2) At the interface NiO/gas the most prominent reaction is the incorporation of gaseous oxygen into the film (Eq. 95). (3) In equivalence to Ni oxidation at the Ni/NiO interface, O_2 is reduced to two O^{2-}-ions by absorbance of four free electrons from the NiO film. Eq. 97 allows for modeling nickel oxidation by steam via dissociation of water to hydrogen and oxygen.

At the interface NiO/YSZ oxygen-ions from the electrolyte phase can be incorporated into the NiO film (Eq. 98). Since this reaction is a charge transfer reactions (it affects the concentration of charged species in the adjacent phases) it couples the electrochemical potentials of NiO and YSZ phase (boundary condition for ϕ in Eq. 88).

Table 6. Model parameters for NiO film growth ($T = 1073$ K).

Film species	Thermodynamic data (h, s)	Ref.	Diffusion data (D_0, E_a)	Ref.
Ni^{2+}	80 kJ mol^{-1}, 0 J mol^{-1} K^{-1}	[138]	4.3×10^{-5} m^2 s^{-1}, 171.7 kJ mol^{-1}	[140]
O^{2-}	-182 kJ mol^{-1}, 17.7 J mol^{-1} K^{-1}	[139]	17.7×10^{-2} m^2 s^{-1}, 259.8 kJ mol^{-1}	[137]
e^-	0, 0		4.3×10^{-5} m^2 s^{-1}, 171.7 kJ mol^{-1}	[140]
Interface NiO/Ni (thermo- and electrochemical oxidation)			**Kinetic data (k^f)**	**Eq.**
Ni $\rightleftarrows$ Ni^{2+}[film] + 2 e$^-$[film]			1×10^2 m kmol^{-1} s^{-1}	(92)
Ni^{2+}[film] + O^{2-}[film] $\rightleftarrows$ NiO			1×10^{-3} m^4 kmol^{-1} s^{-1}	(93)
e$^-$[film] $\rightleftarrows$ e$^-$[Ni]			1×10^{-6} m kmol^{-1} s^{-1}	(94)
Interface NiO/Gas (thermochemical oxidation)			**Kinetic data (k^f)**	**Eq.**
O_2 + 4 e$^-$[film] $\rightleftarrows$ 2 O^{2-}[film]			5×10^{-3} m^4 kmol^{-1} s^{-1}	(95)
Ni^{2+}[film] + O^{2-}[film] $\rightleftarrows$ NiO			1×10^{-1} m^4 kmol^{-1} s^{-1}	(96)
2 H_2O $\rightleftarrows$ 2 H_2 + O_2			1×10^5 m kmol^{-1} s^{-1}	(97)
Interface NiO/YSZ (electrochemical oxidation)			**Kinetic data (k^f)**	**Eq.**
O^{2-}[film] $\rightleftarrows$ O^{2-}[YSZ]			6×10^{-8} m^4 kmol^{-1} s^{-1}	(98)
Ni^{2+}[film] + O^{2-}[film] $\rightleftarrows$ NiO			1×10^{-1} m^4 kmol^{-1} s^{-1}	(99)

Reaction kinetics are chosen such, that migration through the film is the rate-limiting step for NiO formation for $X_{O_2} = 1$ [39] during thermochemical oxidation, and for $E = 0.1$ V during electrochemical oxidation at a temperature of $T = 1073$ K. For low oxygen partial pressures or high cell voltages the oxygen incorporating step can get rate determining (Eq. 95 or Eq. 98). Since not temperature dependencies of the assumed reactions are known, the activation energies are set to zero and only forward rate constants are listed in Table 6. Backward reaction

rates follow from thermodynamic consistency.

The initial film NiO thickness is set to 10^{-10} m.

5.2.4   Numerical implementation

The model was implemented into the multi-phase modeling framework, which was described above (Chapter 3). The film is treated as special case of a bulk phase. Modeling of a film with variable thickness requires the introduction of a discretization mesh with adaptive grid sizes. By defining grid sizes as fraction of the film thickness, the absolute compartment size can be recalculated in each calculation step,

$$dz_j = \zeta_j \delta$$

(100)

where dz is the absolute size and ζ the fraction of grid compartment j with respect to the film thickness δ.

To achieve mass conservation of the species inside the film upon changing grid sizes the species conservation equation (Eq. 88) has to be extended by an additional source term. This is illustrated in Figure 47: If grid sizes are changed relative to film thickness (Eq. 91) a growing film results in an apparent increase of average concentration. Concentration c of a species inside the film can be written as,

$$c_i = \frac{n_i}{\delta \cdot A^V}$$

(101)

where n_i is the absolute amount of species i. Under the condition of a constant n_i and assuming a fixed surface area, derivation with respect to time gives the required corrective source term,

$$\frac{\partial c_i}{\partial t} = -\frac{n_i}{\delta^2 A^V} \cdot \frac{\partial \delta}{\partial t} = -\frac{c_i}{\delta} \cdot \frac{\partial \delta}{\partial t}$$
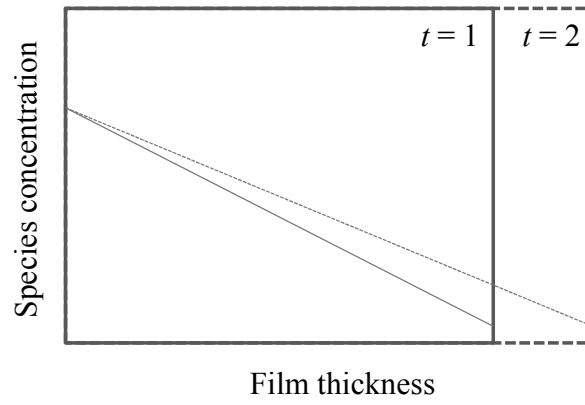
(102)

Figure 47. Illustration of concentration overestimation due to adaptive grid size adjustment. This is fixed by a correction term which is added to the species conservation equation.

5.3 Results and discussion

5.3.1 Thermochemical oxidation

For simulating thermochemical oxidation it is assumed that the reduced nickel electrode is exposed to oxygen at different mole fractions (X_{O_2} = 1, 0.1, 10^{-2}, 10^{-3}, 10^{-4}, 10^{-5}) in binary O_2/N_2 mixtures, and alternatively to pure water vapor. The counterelectrode is exposed to air. Total pressure of 1.013 bar and temperature of 1073 K are assumed. Further, a growing NiO film with interfaces to the gas phase (NiO/gas) and to bulk Ni (NiO/Ni), with the respective reactions given in Table 6, is considered. The electrode is assumed to consist of a solid nickel block with a thickness of 100 μm. This assumption offers the possibility of direct comparison to experiments by Atkinson [140]; a realistic geometry occurring in SOFC electrodes will be investigated below.

Figure 48a shows simulated NiO film growth for this case. Solid lines indicate the film thickness as function of time. For X_{O_2} = 1 the simulation shows good agreement with experimental data by Atkinson [140]. This profile shows a parabolic shape, which is well-known to correspond to a growth process where bulk diffusion is the rate-limiting step [141]. Decreasing oxygen pressures cause a decreased oxidation rate and simultaneously an increasing deviation from parabolic behavior. The deviation is caused by different kinetics during the beginning of the oxidation process. For a small film thickness and low oxygen pressure the rate-limiting process changes from bulk transport to surface reaction [141]. Most probably the oxygen reduction reaction is the rate-limiting step under these conditions. This effect is very prominent for oxidation in water vapor (X_{H_2O} = 1). In this case, the simulated profile shows completely linear oxidation kinetics in the depicted time span.

This interpretation is supported by the concentration profiles shown in Figure 48b. For X_{O_2} = 1 (solid lines) the concentrations of nickel ions and electrons show a strong gradient. Concentrations are about zero at the NiO/gas interface and increase throughout the film. Due to imposed local charge neutrality, electron concentration is twice the Ni^{2+} concentration, while oxygen ion concentration is low. The electrical potential shows only a small gradient. These results are in agreement with the profiles for diffusion-limited film growth predicted by Atkinson [136]. However, for X_{O_2} = 10^{-5} (dotted lines) a different behavior can be observed. Here, concentrations of all species are nearly constant. This shows that the rate-limiting step

for Ni oxidation has changed from diffusion to the oxygen reduction reaction (Eq. 95) for low oxygen partial pressures.
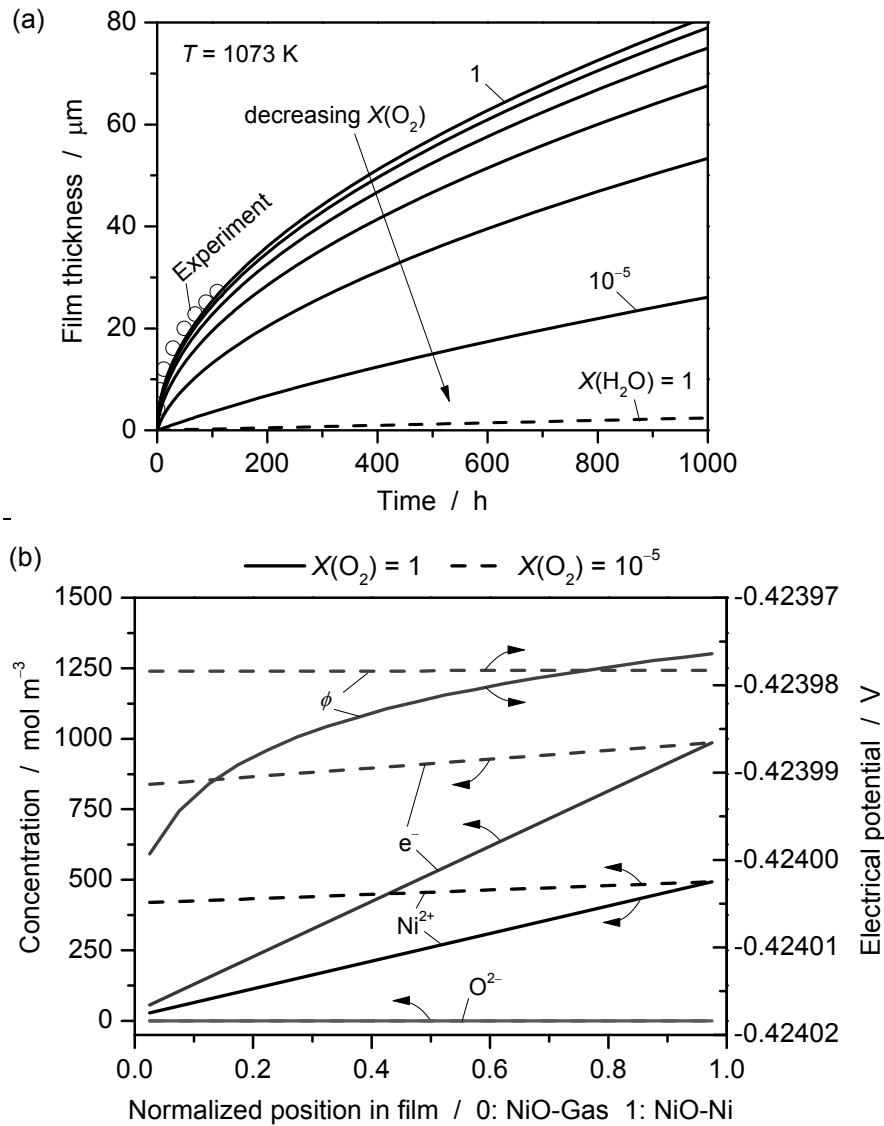
Figure 48. (a) Simulated NiO film growth via thermochemical Ni oxidation in comparison to measurements by Atkinson et al. [140] (b) Species concentration profiles and electrical potential distribution inside the film at 100 h for $X_{O_2} = 1$ and $X_{O_2} = 10^{-5}$.

5.3.2 Electrochemical oxidation

For simulating electrochemical oxidation, it is assumed that the nickel electrode is exposed to pure nitrogen. In this case, the only electrochemical driving force between the electrodes is nickel oxidation. Further, a growing NiO film with interfaces to Ni (NiO/Ni) and YSZ (NiO/YSZ), with the respective reactions given in Table 6, is assumed. The counterelectrode is exposed to air.

Figure 49a shows simulated NiO film growth for different cell voltages E (solid lines). Comparison to thermochemical oxidation by $X_{O_2} = 1$ (dotted line) shows that electrochemical oxidation is faster than thermochemical oxidation for voltages < 0.4 V. Oxidation kinetics do not show parabolic behavior. For $E = 0.4$ V the deviation is clearly visible by comparison to the profile for $X_{O_2} = 1$. For low film thickness oxidation kinetics are slower than parabolic, but for high thickness they are faster. Lower voltages show the same behavior. For high cell voltages ($E > 0.4$ V) profiles are quasi-linear indicating a surface reaction as rate-limiting step [141].
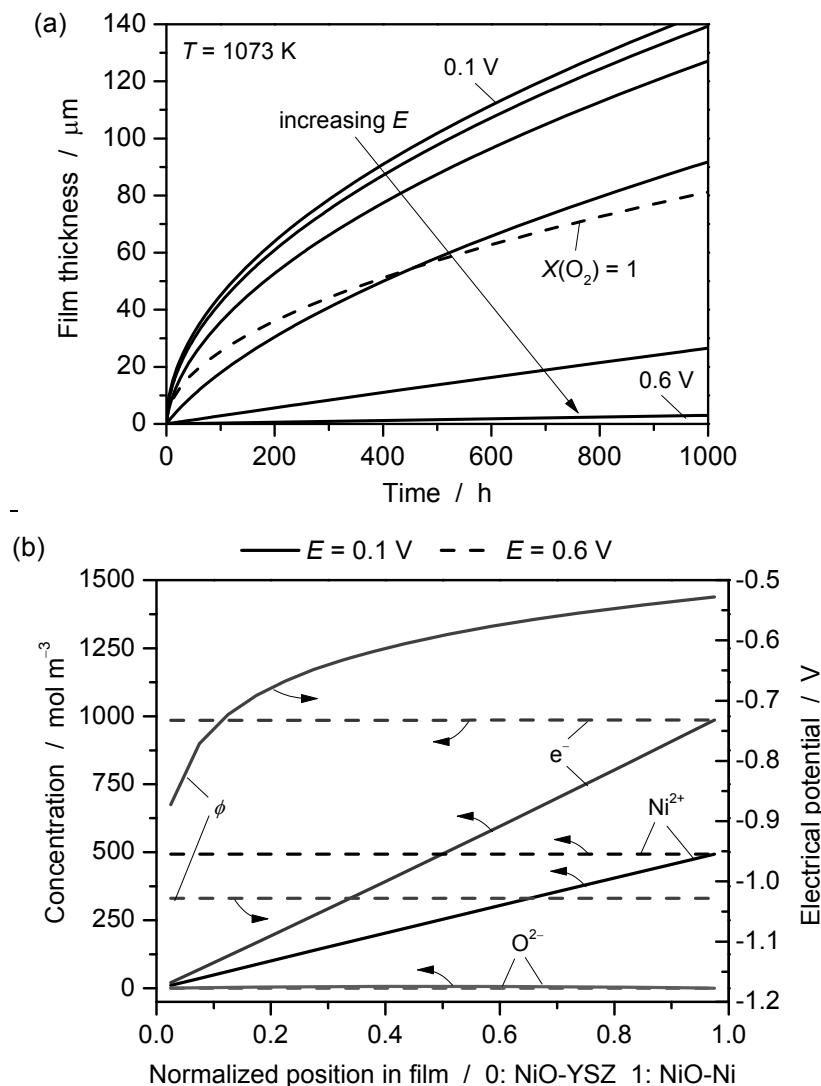

Figure 49. (a) Simulated NiO film growth via electrochemical Ni oxidation. The dashed line shows results for thermochemical oxidation (Figure 48). (b) Species concentration profiles and electrical potential distribution inside the film after 100 h for cell voltages of $E = 0.1$ V and $E = 0.6$ V.

Concentration profiles for all species and the electrical potential are shown for two voltages ($E = 0.1$ V and $E = 0.6$ V) in Figure 49b. Species profiles are very similar to the case of thermochemical oxidation (cf. Figure 2b). For $E = 0.1$ V transport of nickel ions is rate-limiting, while for $E = 0.6$ the oxidation is controlled by oxygen transfer into the NiO (Eq. 15). However, in contrast to thermochemical oxidation, a large potential gradient of about 0.4 V can be observed for $E = 0.1$ V. This gives a possible explanation for the fast kinetics for electrochemical oxidation shown in Figure 48a. Due to the potential gradient an additional migration flux can support the transport of nickel ions, allowing for faster film growth.

5.3.3 Combined model

Combination of thermochemical and electrochemical oxidation is simulated by assuming a nickel layer of 1 μm thickness surrounded by two individual NiO films, yielding a "stack" YSZ/NiO/Ni/NiO/Gas, where the left-hand side allows electrochemical oxidation while the right-hand side allows thermochemical oxidation. This allows the simulation of competition of both processes. Furthermore the conditions that occur locally during SOC operation [9] can be reproduced. Figure 50 depicts the simulated oxidation processes which are described by the simulated "stack" in the combined film model, in comparison to the processes assumed in the real microstructure of SOCs. Nickel particles can be oxidized by formation of a thermochemical and/or electrochemical film. In the real microstructure the TPB is blocked rapidly by either oxidation process. This can be modeled by a function which couples the active TPB length to the thickness of the nickel oxide films; e.g., $A_{TPB}^V = 0$ for $\delta > 50$ nm.
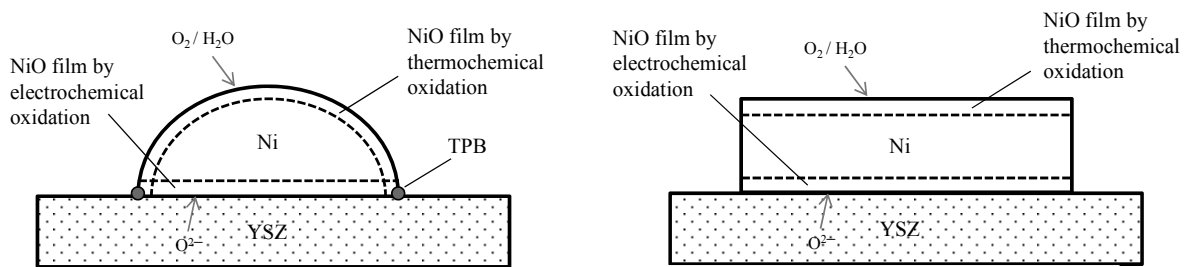
Figure 50. Illustration of thermochemical and electrochemical oxidation process as assumed in the real microstructure (left) and as described by the combined film model (right). In the real microstructure the TPB is blocked rapidly by either oxidation process.

Figure 51 shows oxidation of the nickel layer upon thermochemically and electrochemically strongly oxidative conditions ($X_{O_2} = 1$, $E = 0.1$ V). The counterelectrode is exposed to air. In a time span of 3.8 min the complete nickel (solid line) is oxidized to a growing film of NiO from the interface to the gas phase (dotted line) as well as a second film forming at the interface to YSZ (dashed line). Due to the increase of molar volume [39] the final nickel oxide layer has a total thickness of 1.52 µm, out of which 39 % were formed by the thermochemical and 61 % by the electrochemical process.

Figure 51. Competition of thermochemical and electrochemical film growth during oxidation of a nickel layer with 1 µm thickness.

5.4 Summary and Conclusions

The growth of nickel oxide in solid oxide cells was modeled by description as a flat one-dimensional film. The model can succes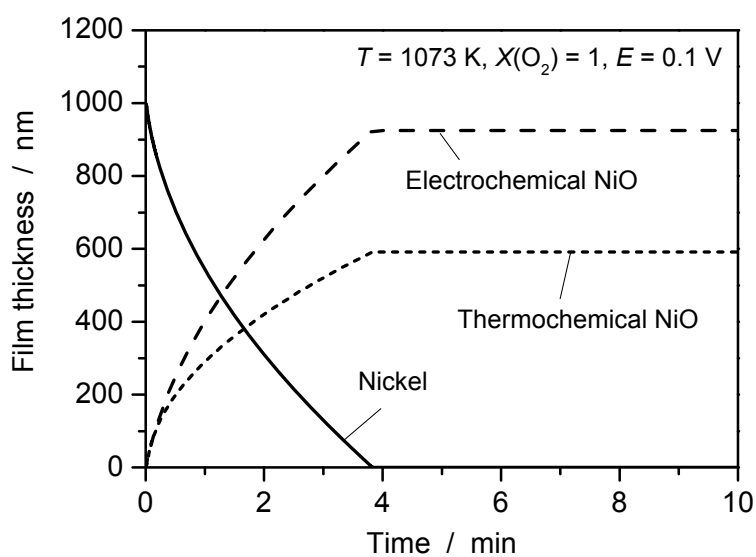sfully reproduce oxidation by molecular oxygen or water from the gas phase (thermochemical oxidation) as well as oxidation by oxygen ions from the YSZ electrolyte, driven by a potential gradient (electrochemical oxidation). In case of thermochemical oxidation, good agreement to a measurement by Atkinson et al. [140] is obtained. Simulations show that for high oxygen partial pressures ($xO_2 > 10^{-5}$) and for low cell voltages ($E < 0.4$ V) transport of nickel ions in the film is the rate-limiting step for film layer growth. At lower oxygen pressures or higher cell voltages the model predicts a growth which is co-limited by oxygen incorporation into the NiO at the interfaces. Electrochemical oxidation is a potentially faster process than thermochemical oxidation because the occurring potential gradient supports species transport via migration.

Coupling of both oxidation mechanisms in a combined model can give insight into properties at real SOC operation conditions. Simultaneous oxidation from two interfaces increases the speed of oxidation. At the presented conditions ($T = 1073$ K, $xO_2 = 1$, $E = 0.1$ V) a nickel layer of 1 µm thickness is completely oxidized in a time span of 3.8 min.

The presented model is the basis for further investigations on nickel oxide formation under SOC operating conditions, aiming at a more fundamental understanding of electrode degradation mechanisms. Future simulations can provide a quantitative predictive capability for improving electrode design and controlling operating conditions.

6 SUMMARY AND OUTLOOK

6.1 Summary

By their ability to convert excessive electrical energy into chemical fuels and vice versa with high efficiency, solid oxide cells (SOC) are a promising technology that can contribute to an economy based on 100 % renewable resources. However, durability is a major issue for reliable operation of SOC systems. One severe degradation mechanism is the formation of nickel oxide (NiO) inside the fuel electrode of SOCs. The goal of the research presented in this thesis is a detailed analysis of the NiO formation process by development and application of mathematical models and simulations, as well as the prediction of operation conditions which minimize degradation.

The background chapter provided fundamental knowledge on the working principle of SOCs, including thermodynamics, electrochemistry, transport phenomena and degradation mechanisms occurring at the fuel electrode. It was complemented by a section on numerical modeling.

As basis for modeling and simulation of NiO formation an existing in-house code framework describing transport and electrochemistry in electrochemical cells (DENIS) was extended by multi-phase functionality. This includes the following aspects:

1) The spatiotemporal evolution of gaseous, liquid and solid phases is described in a 1D + 1D continuum approach. In particular, phase formation and dissolution as well as phase transitions (multi-phase management) can be modeled by the newly developed framework.

2) Feedback between multi-phase management and microstructural properties is implemented via coupling of effective properties of the cell, like electrochemically active areas or mass and charge transport coefficients, to the volume fractions of related phases.

3) For calculation of chemical source terms DENIS was internally coupled to the open-source software CANTERA, which enables access to a large database for thermodynamic species data and provides the ability to use conveniently-structured input files.

4) The validity and flexibility of the developed framework was demonstrated by three exemplary studies regarding secondary-phase formation in PEFCs, Li-S and Li-O batteries which were developed in collaboration with co-workers at DLR Stuttgart.

Based on the new computational capabilities the conditions causing NiO formation and its feedback on cell performance were investigated in detail. A thermochemical and an electrochemical pathway for NiO formation were implemented in the model of a solid oxide cell and parameterized using experimental data from literature. The model includes feedback of nickel oxide on cell performance by decreased active triple phase boundary length and reduction of electrode porosity. The following results were obtained:

1) Thermodynamic calculations show the limits for nickel oxidation under steady-state conditions. For a temperature of 1073 K, nickel oxidation occurs for oxygen partial pressure $p_{O_2} > 1.26 \cdot 10^{-9}$ Pa, fuel-to-steam ratio $p_{H_2}/p_{H_2O} < 6.25 \cdot 10^{-3}$, or local voltage $E_{local} < 0.704$ V.

2) Ni oxidation is governed by local conditions inside the electrode (local fuel-to-steam ratio p_{H_2}/p_{H_2O}, local electrode potential). The analysis of global operating conditions (fuel utilization, cell voltage) allows only limited conclusions on Ni oxidation propensity. Instead, the exact limits for cell voltage and fuel utilization have to be derived numerically for individual cell geometries and system conditions.

3) Ni oxidation is governed by a complex interdependence of thermochemical and electrochemical oxidation pathways. Thermochemical nickel oxidation generally dominates electrochemical nickel oxidation in the cases where local conditions show opposing driving forces (thermochemical oxidation and electrochemical reduction, or vice versa). As consequence of this observation, cells can be operated far below the limiting oxidation voltage (0.704 V at 1073 K) as long as fuel utilization remains sufficiently low

(< 95 % for the cell geometry studied here).

4) Under SOEC operation, the formation of NiO is unlikely due to high cell voltages and the production of hydrogen. Simulations do show a region of oxidized electrode upon cell operation with 100 % steam, depending on current density. Adding 1 % hydrogen to steam completely prevents electrode reoxidation.

5) Irreversible cell degradation based on microstructural changes of the electrode upon re-dox cycling could be successfully demonstrated. The model allows the prediction of performance losses of an SOC which undergoes total or partial reoxidation.

A more detailed insight into the fundamental processes causing nickel oxide formation could be obtained by an additional sub-model, which describes the growth of a NiO film on nano/micro scale. The growth of NiO is modeled by diffusion and migration of species through a flat one-dimensional film. Parameterization with experimental data from literature allows modeling of thermochemical and electrochemical initiation of the oxidation process.

1) Simulations show that for high oxygen partial pressures ($X_{O_2} > 10^{-5}$) and for low cell voltages ($E < 0.4$ V) transport of nickel ions is the rate-limiting step for film layer growth. At lower oxygen pressures or higher cell voltages the model predicts a growth which is co-limited by oxygen incorporation into the NiO at both interfaces. Electro-chemical oxidation is a potentially faster process than thermochemical oxidation be-cause the occurring potential gradient supports species transport via migration.

2) Coupling of both oxidation mechanisms into a combined model can give insight into the behavior under real SOC operation conditions. Simultaneous oxidation from two inter-faces increases the speed of oxidation. At the presented conditions ($T = 1073$ K, $X_{O_2} = 1$, $E = 0.1$ V) a nickel layer of 1 μm thickness is completely oxidized within a time span of 3.8 min.

6.2 Outlook

The present work provides a well-founded basis for further studies. Especially, the developed multi-phase management for modeling secondary-phase formation in electrochemical cells is already being used in several ongoing projects. The following list gives some personal recommendations for possible further research:

1) The multi-phase modeling framework (Chapter 3) can be used as basis for the implementation of further degradation mechanisms into the presented model of a solid oxide cell. Examples concerning the anode of SOFCs are carbon deposition (already work in progress [76]) and sulfur poisoning. Moreover, application of the framework for modeling secondary-phase formation in other electrochemical systems, like PEFC or batteries is feasible, as demonstrated in Section 3.6 (work in progress [142–145]).

2) The model for nickel oxide formation (Chapter 4) can be applied for cells in (or in progress to) scientific and industrial applications, e.g., like the DLR hybrid power plant project [146]. After parameterization the model can be used as powerful tool for prediction of safe operation conditions and for adjustment of optimum working strategy (model predictive control).

3) The general implementation of the model used to describe the growth of a nickel oxide film (Chapter 5) allows a transfer to describe multiple similar processes. For example, it could be applied to describe the transport of species and radicals through the membrane of PEFC or formation and dissolution of the solid electrolyte interface (SEI) in lithium-ion batteries.

This thesis has presented a detailed description of nickel oxidation in solid oxide cells based on a numerical modeling and simulation approach. Results allow a detailed insight into the physiochemical processes causing electrode reoxidation under various operation conditions. The numerical prediction of safe operation conditions can be applied to prevent degradation by NiO formation in SOCs.

REFERENCES

[1]   "Bundesministerium für Wirtschaft und Technologie," "Bruttostromerzeugung in Deutschland 2011," *Ausgewählte Grafiken zum Thema Energieträger*, 2013. [Online]. Available: http://www.bmwi.de/DE/Themen/Energie/Energiedaten/energietraeger.html. [Accessed: 15-Apr-2013].

[2]   H.-M. Henning and A. Palzer, "100 % Erneuerbare Energien für Strom und Wärme in Deutschland." Fraunhofer-Institut für Solare Energiesysteme ISE, Freiburg, 2012.

[3]   S. Curtin, J. Gangi, E. Delmont, and F. Cells, "The Business Case for Fuel Cells: Why Top Companies are Purchasing Fuel Cells Today," Washington, D.C., 2010.

[4]   A. Hauch, S. D. Ebbesen, S. H. Jensen, and M. Mogensen, "Highly efficient high temperature electrolysis," *Journal of Materials Chemistry*, vol. 18, no. 20, pp. 2331-2340, 2008.

[5]   W. Kreuter and H. Hofmann, "Electrolysis: The important energy transformer in a world of sustainable energy," *International Journal of Hydrogen Energy*, vol. 23, no. 8, 1998.

[6]   P. Holtappels and R. Steinberger-Wilckens, "Realising Reliable, Durable, Energy Efficient and Cost Effective SOFC Systems (Real-SOFC)," *Fuel Cells*, vol. 9, no. 6, pp. 783-784, 2009.

[7]   W. G. Bessler, S. Gewies, and M. Vogler, "A new framework for physically based modeling of solid oxide fuel cells," *Electrochimica Acta*, vol. 53, no. 4, pp. 1782-1800, 2007.

[8]   J. P. Neidhardt, D. N. Fronczek, T. Jahnke, T. Danner, B. Horstmann, and W. G. Bessler, "A Flexible Framework for Modeling Multiple Solid, Liquid and Gaseous Phases in Batteries and Fuel Cells," *Journal of the Electrochemical Society*, vol. 159, no. 9, p. A1528-A1542, 2012.

[9]   J. P. Neidhardt and W. G. Bessler, "Competition of electrochemical and thermochemical nickel oxidation in SOFC and SOEC electrodes: Thermodynamic analysis, modeling, and simulation," *Journal of Power Sources*, p. submitted, 2013.

[10] J. P. Neidhardt, R. J. Kee, and W. G. Bessler, "Electrode reoxidation in solid-oxide cells: Detailed modeling of nickel oxide film growth," *13th International Symposium on Solid Oxide Fuel Cells (SOFC-XIII) (in prep.)*. Okinawa, Japan, Oct-2013.

[11] R. O'Hayre, S.-W. Cha, W. Colella, and F. B. Prinz, *Fuel Cell Fundamentals*, 2nd Ed. New York: John Wiley & Sons, 2009.

[12] R. Bove and S. Ubertini, *Modeling solid oxide fuel cells: methods, procedures and techniques*, vol. 1. Springer, 2008.

[13] E. Murray, T. Tsai, and S. Barnett, "A direct-methane fuel cell with a ceria-based anode," *Nature*, vol. 400, pp. 649-651, 1999.

[14] F. Bidrawn, G. Kim, G. Corre, J. T. S. Irvine, J. M. Vohs, and R. J. Gorte, "Efficient Reduction of CO2 in a Solid Oxide Electrolyzer," *Electrochemical and Solid-State Letters*, vol. 11, no. 9, p. B167, 2008.

[15] A. Atkinson et al., "Advanced anodes for high-temperature fuel cells," *Nature materials*, vol. 3, no. 1, pp. 17-27, 2004.

[16] W. . Zhu and S. . Deevi, "A review on the status of anode materials for solid oxide fuel cells," *Materials Science and Engineering: A*, vol. 362, no. 1–2, pp. 228-239, 2003.

[17] C. Sun, R. Hui, and J. Roller, "Cathode materials for solid oxide fuel cells: a review," *Journal of Solid State Electrochemistry*, vol. 14, no. 7, pp. 1125-1144, 2010.

[18] R. Knibbe, A. Hauch, J. Hjelm, S. D. Ebbesen, and M. Mogensen, "Durability of Solid Oxide Cells," *Green*, vol. 1, no. 2, pp. 141-169, 2011.

[19] E. D. Wachsman and K. T. Lee, "Lowering the temperature of solid oxide fuel cells.," *Science*, vol. 334, no. 6058, pp. 935-9, 2011.

[20] C. Graves, S. D. Ebbesen, M. Mogensen, and K. S. Lackner, "Sustainable hydrocarbon fuels by recycling CO2 and H2O with renewable or nuclear energy," *Renewable and Sustainable Energy Reviews*, vol. 15, no. 1, pp. 1-23, 2011.

[21] R. J. Kee, H. Zhu, and D. G. Goodwin, "Solid-oxide fuel cells with hydrocarbon fuels," *Proc. Combust. Inst.*, vol. 30, pp. 2379-2404, 2005.

[22] J. S. Newman and K. E. Thomas-Alyea, *Electrochemical systems*. Wiley-Interscience, 2004.

[23] A. Faghri and Y. Zhang, *Transport phenomena in multiphase systems*. Elsevier, 2006.

[24] B. J. McBride, M. J. Zehe, and S. Gordon, "NASA Glenn coefficients for calculating thermodynamic properties of individual species," *National Aeronautics and Space Administration, John H. Glenn Research Center at Lewis Field*, 2002. [Online]. Available: http://www.grc.nasa.gov/WWW/CEAWeb/ceaThermoBuild.htm.

[25] P. W. Atkins and J. De Paula, *Atkins' Physical chemistry*, 8. ed. Oxford [u.a.]: Oxford University Press, 2006.

[26] S. B. Adler and W. G. Bessler, "Elementary kinetic modeling of SOFC electrode reactions," in *Handbook of Fuel Cells—Fundamentals, Technology and Applications*, vol. 5, W. Vielstich, H. Yokokawa, and H. A. Gasteiger, Eds. Chichester, UK: John Wiley & Sons, 2009, pp. 441-462.

[27] M. Vogler, A. Bieberle-Hutter, L. Gauckler, J. Warnatz, and W. G. Bessler, "Modelling Study of Surface Reactions, Diffusion, and Spillover at a Ni/YSZ Patterned Anode," *Journal of the Electrochemical Society*, vol. 156, no. 5, p. B663-B672, 2009.

[28] V. Yurkiv, D. Starukhin, H.-R. Volpp, and W. G. Bessler, "Elementary Reaction Kinetics of the $CO/CO_2/Ni/YSZ$ Electrode," *Journal of The Electrochemical Society*, vol. 158, no. 1, p. B5, 2011.

[29] H. Zhu, R. J. Kee, V. M. Janardhanan, O. Deutschmann, and D. G. Goodwin, "Modeling elementary heterogeneous chemistry and electrochemistry in solid-oxide fuel cells," *Journal of the Electrochemical Society*, vol. 152, p. A2427-A2440, 2005.

[30] K. Christmann, *Introduction to surface physical chemistry*. Steinkopff, 1991.

[31] M. Shishkin and T. Ziegler, "Oxidation of H2, CH4, and CO molecules at the interface between Nickel and Yttria-Stabilized Zirconia: A theoretical study based on DFT," *The Journal of Physical Chemistry C*, vol. 113, no. 52, pp. 21667-21678, 2009.

[32] V. Yurkiv, A. Gorski, W. G. Bessler, and H.-R. Volpp, "Density functional theory study of heterogeneous CO oxidation over an oxygen-enriched yttria-stabilized zirconia surface," *Chemical Physics Letters*, vol. 543, pp. 213-217, 2012.

[33] U. Hornung, *Homogenization and porous media*. Springer, 1997.

[34] M. Matyka, A. Khalili, and Z. Koza, "Tortuosity-porosity relation in porous media flow," *Physical Review E*, vol. 78, no. 2, pp. 1-8, 2008.

[35] W. G. Bessler, "Electrochemistry and transport in solid oxide fuel cells," *Habilitation, University Heidelberg*, 2007.

[36] F. Tietz, D. Sebold, a. Brisse, and J. Schefold, "Degradation phenomena in a solid oxide electrolysis cell after 9000 h of operation," *Journal of Power Sources*, vol. 223, pp. 129-135, 2013.

[37] H. Yokokawa, "Overview of solid oxide fuel cell degradation," in *Handbook of Fuel Cells—Fundamentals, Technology and Applications*, John Wiley & Sons, 2009, pp. 923-932.

[38] A. Faes, A. Hessler-Wyser, A. Zryd, and Van herleJan, "A Review of RedOx Cycling of Solid Oxide Fuel Cells Anode," *Membranes*, vol. 2, no. 4, pp. 585-664, 2012.

[39] D. Sarantaridis and A. Atkinson, "Redox Cycling of Ni Based Solid Oxide Fuel Cell Anodes: A Review," *Fuel Cells*, vol. 7, no. 3, pp. 246-258, 2007.

[40] T. Klemenso, C. Chung, P. H. Larsen, and M. Mogensen, "The mechanism behind redox instability of anodes in high-temperature SOFCs," *Journal of the Electrochemical Society*, vol. 152, no. 11, p. A2186-A2192, 2005.

[41] A. Faes, A. Hessler-Wyser, D. Presvytes, C. G. Vayenas, and J. Van Herle, "Nickel-Zirconia Anode Degradation and Triple Phase Boundary Quantification from Microstructural Analysis," *Fuel Cells*, vol. 9, no. 6, pp. 841-851, 2009.

[42] M. Pihlatie, A. Kaiser, and M. Mogensen, "Redox stability of SOFC: Thermal analysis of Ni-YSZ composites," *Solid State Ionics*, vol. 180, no. 17, pp. 1100-1112, 2009.

[43] M. Ettler, H. Timmermann, J. Malzbender, A. Weber, and N. H. Menzler, "Durability of Ni anodes during reoxidation cycles," *Journal of Power Sources*, vol. 195, no. 17, pp. 5452-5467, 2010.

[44] D. Sarantaridis, R. A. Rudkin, and A. Atkinson, "Oxidation failure modes of anode-supported solid oxide fuel cells," *Journal of Power Sources*, vol. 180, no. 2, pp. 704-710, 2008.

[45] J. Laurencin, G. Delette, B. Morel, F. Lefebvre-Joud, and M. Dupeux, "Solid Oxide Fuel Cells damage mechanisms due to Ni-YSZ re-oxidation: Case of the Anode Supported Cell," *Journal of Power Sources*, vol. 192, no. 2, pp. 344-352, 2009.

[46] J. Malzbender, R. W. Steinbrech, and L. Singheiser, "A review of advanced techniques for characterising SOFC behaviour," *Fuel Cells*, vol. 9, no. 6, pp. 785-793, 2009.

[47] J. Yu, K. M. Rosso, and S. M. Bruemmer, "Charge and Ion Transport in NiO and Aspects of Ni Oxidation from First Principles," *Journal of Physical Chemistry C*, vol. 116, no. 2, pp. 1948-1954, 2012.

[48] T. Matsui, R. Kishida, J.-Y. Kim, H. Muroyama, and K. Eguchi, "Performance Deterioration of Ni–YSZ Anode Induced by Electrochemically Generated Steam in Solid Oxide Fuel Cells," *Journal of the Electrochemical Society*, vol. 157, no. 5, p. B776-B781, 2010.

[49] E. Ivers-Tiffée, H. Timmermann, A. Leonide, N. H. Menzler, and J. Malzbender, "Methane reforming kinetics, carbon deposition, and redox durability of Ni/8 yttria-stabilized zirconia (YSZ) anodes," in *Handbook of Fuel Cells—Fundamentals, Technology and Applications*, W. Vielstich, H. Yokokawa, and H. A. Gasteiger, Eds. Chichester, UK: John Wiley & Sons, 2009, pp. 933-955.

[50] X. Yang and J. T. S. Irvine, "(La0.75Sr0.25)0.95Mn0.5Cr0.5O3 as the cathode of solid oxide electrolysis cells for high temperature hydrogen production from steam," *Journal of Materials Chemistry*, vol. 18, no. 20, pp. 2349-2354, 2008.

[51] J. Deseure, J.-M. Klein, Y. Bultel, and L. Dessemond, "3-D Simulations of Charge and Mass Distribution in Tubular SOEC," *ECS Transactions*, vol. 7, no. 1, pp. 2031-2039, 2007.

[52] G. Stathis, D. Simwonis, F. Tietz, A. Moropoulou, and A. Naoumides, "Oxidation and resulting mechanical properties of Ni/8Y2O3-stabilized zirconia anode substrate for solid-oxide fuel cells," *Journal of Materials Research*, vol. 17, no. 5, pp. 951-958, 2002.

[53] C.-H. Wang, M.-C. Lee, T.-J. Huang, Y.-C. Chang, W.-X. Kao, and T.-N. Lin, "Breeding phenomenon of nickel in anode of solid oxide fuel cell via electrochemical reaction," *Electrochemistry Communications*, vol. 11, no. 7, pp. 1381-1384, 2009.

[54] T. Hatae, Y. Matsuzaki, and Y. Yamazaki, "Study on electrochemical re-oxidation of anode-supported solid oxide fuel cells using oxide ion current," *Solid State Ionics*, vol. 179, no. 7–8, pp. 274-281, 2008.

[55] H.-Y. Chen, H.-C. Yu, J. Scott Cronin, J. R. Wilson, S. a. Barnett, and K. Thornton, "Simulation of coarsening in three-phase solid oxide fuel cell anodes," *Journal of Power Sources*, vol. 196, no. 3, pp. 1333-1337, 2011.

[56] W. R. Wilcox, "Morphological stability, convection, graphite, and integral optics," in *Preparation and properties of solid state materials*, Vol. 4., New York: Dekker, 1979.

[57] M. N. Rahaman, *Sintering of ceramics*. Boca Raton, Fla.: CRC Press, 2008.

[58] L. Holzer et al., "Microstructure degradation of cermet anodes for solid oxide fuel cells: Quantification of nickel grain growth in dry and in humid atmospheres," *Journal of Power Sources*, vol. 196, no. 3, pp. 1279-1294, 2011.

[59] J. S. Cronin, J. R. Wilson, and S. a. Barnett, "Impact of pore microstructure evolution on polarization resistance of Ni-Yttria-stabilized zirconia fuel cell anodes," *Journal of Power Sources*, vol. 196, no. 5, pp. 2640-2643, 2011.

[60] Z. Jiao, N. Shikazono, and N. Kasagi, "Quantitative Characterization of SOFC Nickel-YSZ Anode Microstructure Degradation Based on Focused-Ion-Beam 3D-Reconstruction Technique," *Journal of the Electrochemical Society*, vol. 159, no. 3, p. B285-B291, 2012.

[61] J. Sehested, J. Gelten, I. Remediakis, H. Bengaard, and J. Nørskov, "Sintering of nickel steam-reforming catalysts: effects of temperature and steam and hydrogen pressures," *Journal of Catalysis*, vol. 223, no. 2, pp. 432-443, 2004.

[62] A. Hauch, S. D. Ebbesen, S. H. Jensen, and M. Mogensen, "Solid Oxide Electrolysis Cells: Microstructure and Degradation of the Ni/Yttria-Stabilized Zirconia Electrode," *Journal of the Electrochemical Society*, vol. 155, no. 11, p. B1184-B1193, 2008.

[63] Z. Jiao, N. Takagi, N. Shikazono, and N. Kasagi, "Study on local morphological changes of nickel in solid oxide fuel cell anode using porous Ni pellet electrode," *Journal of Power Sources*, vol. 196, no. 3, pp. 1019-1029, 2011.

[64]   G. Chen, G. Guan, Y. Kasai, and A. Abudula, "Nickel volatilization phenomenon on the Ni-CGO anode in a cathode-supported SOFC operated at low concentrations of H2," *International Journal of Hydrogen Energy*, vol. 37, no. 1, pp. 477-483, 2012.

[65]   H. Yokokawa, K. Yamaji, M. E. Brito, H. Kishimoto, and T. Horita, "General considerations on degradation of Solid Oxide Fuel Cell anodes and cathodes due to impurities in gases," *Journal of Power Sources*, vol. 196, no. 17, pp. 7070-7075, 2011.

[66]   G. J. Offer, J. Mermelstein, E. Brightman, and N. P. Brandon, "Thermodynamics and kinetics of the interaction of carbon and sulfur with solid oxide fuel cell anodes," *Journal of the American Ceramic Society*, vol. 92, no. 4, pp. 763-780, 2009.

[67]   H. Yokokawa et al., "Thermodynamic considerations on Cr poisoning in SOFC cathodes," *Solid State Ionics*, vol. 177, no. 35–36, pp. 3193-3198, 2006.

[68]   M. Mogensen, K. Jensen, M. Jørgensen, and S. Primdahl, "Progress in understanding SOFC electrodes," *Solid State Ionics*, vol. 150, pp. 123-129, 2002.

[69]   E. M. Ryan, W. Xu, X. Sun, and M. a. Khaleel, "A damage model for degradation in the electrodes of solid oxide fuel cells: Modeling the effects of sulfur and antimony in the anode," *Journal of Power Sources*, vol. 210, pp. 233-242, 2012.

[70]   D. Monder and K. Karan, "Ab Initio Adsorption Thermodynamics of H2S and H2 on Ni (111): The Importance of Thermal Corrections and Multiple Reaction Equilibria," *The Journal of Physical Chemistry C*, vol. 114, no. 51, pp. 22597-22602, 2010.

[71]   L. Maier, B. Schädel, K. Herrera Delgado, S. Tischer, and O. Deutschmann, "Steam Reforming of Methane Over Nickel: Development of a Multi-Step Surface Reaction Mechanism," *Topics in Catalysis*, vol. 54, no. 13–15, pp. 845-858, 2011.

[72]   T. Kim et al., "A study of carbon formation and prevention in hydrocarbon-fueled SOFC," *Journal of Power Sources*, vol. 155, no. 2, pp. 231-238, 2006.

[73]   J.-H. Koh, B.-S. Kang, H. C. Lim, and Y.-S. Yoo, "Thermodynamic Analysis of Carbon Deposition and Electrochemical Oxidation of Methane for SOFC Anodes," *Electrochemical and Solid-State Letters*, vol. 4, no. 2, p. A12, 2001.

[74]   K. Girona and J. Laurencin, "Carbon deposition in CH4/CO2 operated SOFC: Simulation and experimentation studies," *Journal of Power Sources*, vol. 210, pp. 381-391, 2012.

[75]   K. Nikooyeh, A. a. Jeje, and J. M. Hill, "3D modeling of anode-supported planar SOFC with internal reforming of methane," *Journal of Power Sources*, vol. 171, no. 2, pp. 601-609, 2007.

[76]   J. P. Neidhardt, V. Yurkiv, and W. G. Bessler, "Spatiotemporal simulation of nickel oxide and carbon phases formation in solid oxide fuel cells (SOFC)," *Fundamentals & Development of Fuel Cells Conference (FDFC 2013)*. Karlsruhe, Germany, Apr-2013.

[77] A. Hirano, M. Suzuki, and M. Ippommatsu, "Evaluation of a New Solid Oxide Fuel-Cell System by Nonisothermal Modeling," *Journal of the Electrochemical Society*, vol. 139, no. 10, pp. 2744-2751, 1992.

[78] N. F. Bessette, W. J. Wepfer, and J. Winnick, "A Mathematical-Model of a Solid Oxide Fuel-Cell," *Journal of the Electrochemical Society*, vol. 142, no. 11, pp. 3792-3800, 1995.

[79] J. Ferguson, J. Fiard, and R. Herbin, "Three-dimensional numerical simulation for various geometries of solid oxide fuel cells," *Journal of Power Sources*, vol. 58, no. 2, pp. 109-122, 1996.

[80] I. Raistrick, "Impedance studies of porous electrodes," *Electrochimica Acta*, vol. 35, no. 10, pp. 1579-1586, 1990.

[81] N. Nakagawa, C. Kuroda, and M. Ishida, "A new equivalent circuit for Pt/YSZ of a solid oxide electrolyte fuel cell: Relation between the model parameters and the interface characteristics," *Solid State Ionics*, vol. 41, pp. 2-5, 1990.

[82] J. Selman and Y. Lin, "Application of ac impedance in fuel cell research and development," *Electrochimica acta*, vol. 38, no. 14, pp. 2063-2073, 1993.

[83] S. B. Adler, J. A. Lane, and B. C. H. Steele, "Electrode kinetics of porous mixed-conducting oxygen electrodes," *Journal of the Electrochemical Society*, vol. 143, no. 11, pp. 3554-3564, 1996.

[84] P. Costamagna, P. Costa, and V. Antonucci, "Micro-modelling of solid oxide fuel cell electrodes," *Electrochimica Acta*, vol. 43, no. 3–4, pp. 375-394, 1998.

[85] S. Gewies and W. G. Bessler, "Physically Based Impedance Modeling of Ni/YSZ Cermet Anodes," *Journal of The Electrochemical Society*, vol. 155, no. 9, p. B937, 2008.

[86] W. Lehnert, J. Meusinger, and F. Thom, "Modelling of gas transport phenomena in SOFC anodes," *Journal of Power Sources*, vol. 87, no. 1–2, pp. 57-63, 2000.

[87] J. Golbert, C. Adjiman, and N. Brandon, "Microstructural modeling of solid oxide fuel cell anodes," *Industrial & Engineering Chemistry Research*, vol. 47, no. 20, pp. 7693-7699, 2008.

[88] M. Andersson, J. Yuan, and B. Sunden, "Review on modeling development for multiscale chemical reactions coupled transport phenomena in solid oxide fuel cells," *Applied Energy*, vol. 87, no. 5, pp. 1461-1476, 2010.

[89] S. Kakac, a Pramuanjaroenkij, and X. Zhou, "A review of numerical modeling of solid oxide fuel cells," *International Journal of Hydrogen Energy*, vol. 32, no. 7, pp. 761-786, 2007.

[90]   Q.-A. Huang, R. Hui, B. Wang, and J. Zhang, "A review of AC impedance modeling and validation in SOFC diagnosis," *Electrochimica Acta*, vol. 52, no. 28, pp. 8144-8164, 2007.

[91]   K. N. Grew and W. K. S. Chiu, "A review of modeling and simulation techniques across the length scales for the solid oxide fuel cell," *Journal of Power Sources*, vol. 199, pp. 1-13, 2012.

[92]   V. M. Janardhanan and O. Deutschmann, "Modeling of solid-oxide fuel cells," *Zeitschrift Fur Physikalische Chemie-International Journal of Research in Physical Chemistry & Chemical Physics*, vol. 221, no. 4, pp. 443-478, 2007.

[93]   Y. Zhang, C. Xia, and M. Ni, "Simulation of sintering kinetics and microstructure evolution of composite solid oxide fuel cells electrodes," *International Journal of Hydrogen Energy*, vol. 37, no. 4, pp. 3392-3402, 2012.

[94]   P. Tanasini et al., "Experimental and Theoretical Investigation of Degradation Mechanisms by Particle Coarsening in SOFC Electrodes," *Fuel Cells*, vol. 9, no. 5, pp. 740-752, 2009.

[95]   J.-M. Klein, Y. Bultel, M. Pons, and P. Ozil, "Modeling of a Solid Oxide Fuel Cell Fueled by Methane: Analysis of Carbon Deposition," *Journal of Fuel Cell Science and Technology*, vol. 4, no. 4, p. 425, 2007.

[96]   H. Kishimoto, T. Horita, K. Yamaji, M. E. Brito, Y.-P. Xiong, and H. Yokokawa, "Sulfur Poisoning on SOFC Ni Anodes: Thermodynamic Analyses within Local Equilibrium Anode Reaction Model," *Journal of The Electrochemical Society*, vol. 157, no. 6, p. B802, 2010.

[97]   J. Kuebler et al., "Simulation and Validation of Thermo-mechanical Stresses in Planar SOFCs," *Fuel Cells*, vol. 10, no. 6, pp. 1066-1073, 2010.

[98]   A. Atkinson and B. Sun, "Residual stress and thermal cycling of planar solid oxide fuel cells," *Materials Science and Technology*, vol. 23, no. 10, pp. 1135-1143, 2007.

[99]   A. Faes et al., "RedOx study of anode-supported solid oxide fuel cell," *Journal of Power Sources*, vol. 193, no. 1, pp. 55-64, 2009.

[100] J. Udagawa, P. Aguiar, and N. P. Brandon, "Hydrogen production through steam electrolysis: Model-based steady state performance of a cathode-supported intermediate temperature solid oxide electrolysis cell," *Journal of Power Sources*, vol. 166, no. 1, pp. 127-136, 2007.

[101] G. Hawkes, J. O'Brien, C. Stoots, and B. Hawkes, "3D CFD model of a multi-cell high-temperature electrolysis stack," *International Journal of Hydrogen Energy*, vol. 34, no. 9, pp. 4189-4197, 2009.

[102] D. Grondin, J. Deseure, A. Brisse, M. Zahid, and P. Ozil, "Simulation of a high temperature electrolyzer," *Journal of Applied Electrochemistry*, vol. 40, no. 5, pp. 933-941, 2010.

[103] A. V. Virkar, "Mechanism of oxygen electrode delamination in solid oxide electrolyzer cells," *International Journal of Hydrogen Energy*, vol. 35, no. 18, pp. 9527-9543, 2010.

[104] J. Ferziger and M. Peric, *Computational methods for fluid dynamics*. Berlin, Heidelberg: Springer, 1996.

[105] C.-D. Munz and T. Westermann, *Numerische Behandlung gewöhnlicher und partieller Differenzialgleichungen*. Berlin, Heidelberg: Springer, 2006.

[106] R. J. Kee, M. E. Coltrin, and P. Glarborg, "Numerical solution of stiff equations," in *Chemically reacting flow*, Hoboken, NJ: John Wiley & Sons, 2003.

[107] W. G. Bessler, S. Gewies, C. Willich, G. Schiller, and K. A. Friedrich, "Spatial Distribution of Electrochemical Performance in a Segmented SOFC: A Combined Modeling and Experimental Study," *Fuel Cells*, vol. 10, no. 3, pp. 411-418, 2010.

[108] D. G. Goodwin, *Cantera: An object-oriented software toolkit for chemical kinetics, thermodynamics, and transport processes*. Pasadena: Caltech, 2009.

[109] J. P. Neidhardt, T. Jahnke, D. N. Fronczek, T. Danner, B. Horstmann, and W. G. Bessler, "A flexible framework for modeling multiple solid, liquid and gaseous phases in batteries and fuel cells," *9th Symposium on Fuel Cell and Battery Modeling and Experimental Validation (ModVal 9)*. Campus Sursee, CH, Apr-2012.

[110] J. P. Neidhardt, D. N. Fronczek, T. Jahnke, T. Danner, B. Horstmann, and W. G. Bessler, "A flexible modeling framework for multi-phase management in SOFCs and other electrochemical cells," *10th European SOFC Forum (EFCF 2012)*. Lucerne, CH, Jun-2012.

[111] W. G. Bessler and S. Gewies, "Gas Concentration Impedance of Solid Oxide Fuel Cell Anodes," *Journal of the Electrochemical Society*, vol. 154, p. B548, 2007.

[112] P. Andrei, J. P. Zheng, M. Hendrickson, and E. J. Plichta, "Some Possible Approaches for Improving the Energy Density of Li-Air Batteries," *Journal of the Electrochemical Society*, vol. 157, no. 12, p. A1287-A1295, 2010.

[113] P. Deuflhard, E. Hairer, and J. Zugck, "One-Step and Extrapolation Methods for Differential-Algebraic Systems," *Numerische Mathematik*, vol. 51, no. 5, pp. 501-516, 1987.

[114] I. Berg, "muParser," *2005-2012*. [Online]. Available: http://muparser.sourceforge.net.

[115] H. Wu, X. Li, and P. Berg, "On the modeling of water transport in polymer electrolyte membrane fuel cells," *Electrochimica Acta*, vol. 54, no. 27, pp. 6913-6927, 2009.

[116] M. P. Eschenbach, R. Coulon, A. A. Franco, J. Kallo, and W. G. Bessler, "Multi-scale simulation of fuel cells: From the cell to the system," *Solid State Ionics*, vol. 192, no. 1, pp. 615-618, 2011.

[117] I. W. Eames, N. J. Marr, and H. Sabir, "The evaporation coefficient of water: A review," *International Journal of Heat and Mass Transfer*, vol. 40, no. 12, pp. 2963-2973, 1997.

[118] H. Yamin, A. Gorenshtein, J. Penciner, Y. Sternberg, and E. Peled, "Lithium sulfur battery oxidation/reduction mechanisms of polysulfides in THF solutions," *Journal of the Electrochemical Society*, vol. 135, no. 5, pp. 1045-1048, 1988.

[119] S. S. Sandhu, J. P. Fellner, and G. W. Brutchen, "Diffusion-limited model for a lithium/air battery with an organic electrolyte," *Journal of Power Sources*, vol. 164, no. 1, pp. 365-371, 2007.

[120] S. Sörgel et al., "Atomic Force Morphological and Electrical Investigation of Sulphur Cathodes," *Physical Chemistry Chemical Physics, submitted*, 2012.

[121] K. Kumaresan, Y. Mikhaylik, and R. E. White, "A mathematical model for a lithium-sulfur cell," *Journal of the Electrochemical Society*, vol. 155, no. 8, p. A576-A582, 2008.

[122] J. Shim, K. A. Striebel, and E. J. Cairns, "The Lithium/Sulfur Rechargeable Cell: Effects of Electrode Composition and Solvent on Cell Performance," *Journal of The Electrochemical Society*, vol. 149, no. 10, p. A1321-A1325, 2002.

[123] H. S. Ryu, H. J. Ahn, K. W. Kim, J. H. Ahn, J. Y. Lee, and E. J. Cairns, "Self-discharge of lithium–sulfur cells using stainless-steel current-collectors," *Journal of Power Sources*, vol. 140, no. 2, pp. 365-369, 2005.

[124] D. Marmorstein, T. H. Yu, K. A. Striebel, F. R. McLarnon, J. Hou, and E. J. Cairns, "Electrochemical performance of lithium/sulfur cells with three different polymer electrolytes," *Journal of Power Sources*, vol. 89, no. 2, pp. 219-226, 2000.

[125] G. Girishkumar, B. McCloskey, A. C. Luntz, S. Swanson, and W. Wilcke, "Lithium Air Battery: Promise and Challenges," *Journal of Physical Chemistry Letters*, vol. 1, no. 14, pp. 2193-2203, 2010.

[126] R. Padbury and X. Zhang, "Lithium-oxygen batteries--Limiting factors that affect performance," *Journal of Power Sources*, vol. 196, no. 10, pp. 4436–4444, 2011.

[127] W. Xu, J. Xiao, J. Zhang, D. Wang, and J.-G. Zhang, "Optimization of Nonaqueous Electrolytes for Primary Lithium/Air Batteries Operated in Ambient Environment," *Journal of The Electrochemical Society*, vol. 156, no. 10, p. A773-A779, 2009.

[128] S. A. Freunberger et al., "Reactions in the Rechargeable Lithium-O(2) Battery with Alkyl Carbonate Electrolytes," *Journal of the American Chemical Society*, vol. 133, no. 20, pp. 8040-8047, 2011.

[129] P. Albertus et al., "Identifying Capacity Limitations in the Li/Oxygen Battery Using Experiments and Modeling," *Journal of the Electrochemical Society*, vol. 158, no. 3, pp. 343-351, 2011.

[130] J. Neidhardt and W. G. Bessler, "Oxidation of nickel in solid oxide fuel cell anodes: A 2D kinetic modeling approach," *10th European SOFC Forum (EFCF 2012)*. Lucerne, CH, Jun-2012.

[131] V. Yurkiv, J. P. Neidhardt, and W. G. Bessler, "Current-voltage behaviour of SOFCs considering anode degradation," *10th Symposium for Fuel Cell and Battery Modelling and Experimental Validation (ModVal 10)*. Bad Boll, Germany, Mar-2013.

[132] J. P. Neidhardt, V. Yurkiv, and W. G. Bessler, "Prediction of secondary-phase formation and degradation in solid oxide fuel cell anodes," *2nd International Conference on Materials for Energy EnMat II*. Karlsruhe, Germany, May-2013.

[133] R. D. Holmes, H. S. C. O'Neill, and R. J. Arculus, "Standard Gibbs free energy of formation for Cu2O, NiO, CoO, and FexO: High resolution electrochemical measurements using zirconia solid electrolytes from 900-1400 K," *Geochimica et Cosmochimica Acta*, vol. 50, no. 11, pp. 2439-2452, 1986.

[134] A. Hagen et al., "A depth-resolved in-situ study of the reduction and oxidation of Ni-based anodes in solid oxide fuel cells," *Fuel Cells*, vol. 6, no. 5, pp. 361-366, 2006.

[135] C. Wagner, "Beitrag zur Theorie des Anlaufvorgangs," *Z. Phys. Chem. B*, vol. 21, no. 25, 1933.

[136] A. Atkinson, "Transport processes during the growth of oxide films at elevated temperature," *Reviews of Modern Physics*, vol. 57, no. 2, pp. 437-470, 1985.

[137] S. Chevalier, F. Desserrey, and J. P. Larpin, "Oxygen Transport during the High Temperature Oxidation of Pure Nickel," *Oxidation of Metals*, vol. 64, no. 3–4, pp. 219-234, 2005.

[138] P. Kofstad, "Defects and transport properties of metal oxides," *Oxidation of Metals*, vol. 44, no. 1–2, pp. 3-27, 1995.

[139] J. Park and C. Altstetter, "The diffusion and solubility of oxygen in solid nickel," *Metallurgical and Materials Transactions A*, vol. 18A, no. 1, pp. 43-50, 1987.

[140] A. Atkinson, R. Taylor, and A. Hughes, "A quantitative demonstration of the grain boundary diffusion mechanism for the oxidation of metals," *Philosophical Magazine A*, vol. 45, no. 5, pp. 823-833, 1982.

[141] P. Kofstad, *High-Temperature Oxidation of Metals*. New York: John Wiley & Sons, 1966.

[142] T. Jahnke and W. G. Bessler, "Modeling Ruthenium Dissolution in Direct-Methanol Fuel Cells," *Fundamentals & Development of Fuel Cells Conference (FDFC 2013)*. Karlsruhe, Germany, 2013.

[143] A. F. Hofmann, D. N. Fronczek, A. Latz, and W. G. Bessler, "Simulating the polysulfide shuttle effect: a thermodynamically consistent, fully reversible, numerical Li/S-

battery model," *10th Symposium for Fuel Cell and Battery Modelling and Experimental Validation (ModVal 10)*. Bad Boll, Germany, Mar-2013.

[144] B. Horstmann, T. Danner, and W. G. Bessler, "Continuum Modeling of Aqueous and Non-Aqueous Lithium/Oxygen Batteries," in *IMLB 2012*, 2012.

[145] N. Tanaka, C. Hellwig, and W. G. Bessler, "Investigation of a kinetic mechanism for runway thermal-electrochemistry in lithium-ion cells," in *Proceedings of the 19th International Conference on Solid State Ionics*, 2013.

[146] S. Seidler, M. Henke, J. Kallo, W. G. Bessler, U. Maier, and K. A. Friedrich, "Pressurized solid oxide fuel cells: Experimental studies and modeling," *Journal of Power Sources*, vol. 196, no. 17, pp. 7195-7202, 2011.

[147] A. Nyman, M. Behm, and G. Lindbergh, "Electrochemical characterisation and modelling of the mass transport phenomena in LiPF6–EC–EMC electrolyte," *Electrochimica Acta*, vol. 53, no. 22, pp. 6356-6365, 2008.

APPENDIX

Table 7. Definition of parameters for the polymer electrolyte fuel cell. Values are given for $T = 354$ K and $p = 101325$ Pa. Reverse reaction coefficients follow from thermodynamic consistency.

Cathode channel

Length × Width	0.9282×0.002 m
Control volumes	8×1

Species	Initial concentration
O_2	$0.17\ \text{mol·mol}^{-1}$
N_2	$0.68\ \text{mol·mol}^{-1}$
H_2O	$0.15\ \text{mol·mol}^{-1}$

Cathode

Thickness	30 μm
Control volumes	8×9

Bulk phases	Volume fraction (ε_0)	Species	Molar enthalpy	Molar entropy	Density
Pt/C	0.3	—	—	—	—
Nafion	0.3	H^+	$-100\ \text{kJ·mol}^{-1}$	$0\ \text{J·K}^{-1}\text{·mol}^{-1}$	—
Gas	0.4	See channel			
Water$^{(liquid)}$	$1 \cdot 10^{-7}$	$H_2O^{(liquid)}$	$-281.620\ \text{kJ·mol}^{-1}$ [24]	$82.8851\ \text{J·K}^{-1}\text{·mol}^{-1}$ [24]	$1000\ \text{kg·m}^{-3}$

Interfaces	Specific area (A_0)	Reactions	Forward rate	Activation energy
Pt/C-Nafion-Gas	$2.3 \cdot 10^6\ \text{m}^2\text{·m}^{-3}$	$4\,H^+ + O_2 + 4\,e^- \rightleftharpoons H_2O^{(liquid)}$	$1 \cdot 10^{26}\ \text{m}^{13}\text{·mol}^{-1}\text{·s}^{-1}$	$300\ \text{kJ·mol}^{-1}$
Water$^{(liquid)}$-Gas	$1\ \text{m}^2\text{·m}^3$	$H_2O^{(liquid)} \rightleftharpoons H_2O^{(gas)}$	$1.48 \cdot 10^4\ \text{K}^{0.5}\text{·m·s}^{-1}$	$42\ \text{kJ·mol}^{-1}$

Separator

Thickness	50 μm
Control volumes	8×9

Bulk phases	Volume fraction (ε_0)	Species
Nafion	1.0	See cathode

Anode

Thickness	0 μm (flat anode)
Control volumes	8×1

Bulk phases	Volume fraction (ε_0)	Species
Pt/C	0.3	—
Nafion	0.4	See cathode
Gas	0.3	See channel

Interfaces	Specific area (A_0)	Reactions	Forward rate	Activation energy
Pt/C-Nafion-Gas	$2.3 \cdot 10^6\ \text{m}^2\text{·m}^{-3}$	$H_2 \rightleftharpoons 2\,H^+ + 2\,e^-$	$1 \cdot 10^{51}\ \text{m}^{-1}\text{·s}^{-1}$	$300\ \text{kJ·mol}^{-1}$

Anode channel

Length × Width	—
Control volumes	1x1

Species	Initial concentration
H_2	$0.85\ \text{mol·mol}^{-1}$
H_2O	$0.15\ \text{mol·mol}^{-1}$

Table 8. Definition of parameters for the lithium-sulfur cell; converted from Kumaresan et al. [121]. Values are given for T = 298.15 K and p = 101325 Pa.

Cathode

Thickness	41 μm
Control volumes	1×4

Bulk phases	Volume fraction (ε_0)	Species	Density / Inital concentration	Diffusion coefficient
Sulfur	0.16	$S_8^{(solid)}$	$2.07 \cdot 10^3$ kg·m^{-3}	–
Carbon	0.062	C	$2.26 \cdot 10^3$ kg·m^{-3}	–
Electrolyte	0.778	$C_4H_6O_3$	$1.20 \cdot 10^3$ kg·m^{-3} / $1.023 \cdot 10^4$ mol·m^{-3}	–
		Li^+	$1.024 \cdot 10^3$ mol·m^{-3}	$1 \cdot 10^{-10}$ m^2·s^{-1}
		PF_6^-	$1.023 \cdot 10^3$ mol·m^{-3}	$4 \cdot 10^{-10}$ m^2·s^{-1}
		S^{2-}	$8.456 \cdot 10^{-10}$ mol·m^{-3}	$1 \cdot 10^{-10}$ m^2·s^{-1}
		S_2^{2-}	$5.348 \cdot 10^{-7}$ mol·m^{-3}	$1 \cdot 10^{-10}$ m^2·s^{-1}
		S_4^{2-}	$2.046 \cdot 10^{-2}$ mol·m^{-3}	$1 \cdot 10^{-10}$ m^2·s^{-1}
		S_6^{2-}	$3.314 \cdot 10^{-1}$ mol·m^{-3}	$6 \cdot 10^{-10}$ m^2·s^{-1}
		S_8^{2-}	$1.821 \cdot 10^{-1}$ mol·m^{-3}	$6 \cdot 10^{-10}$ m^2·s^{-1}
		$S_8^{(dissoluted)}$	$1.943 \cdot 10^1$ mol·m^{-3}	$1 \cdot 10^{-9}$ m^2·s^{-1}
		$Li_2S^{(solid)}$	1640 kg·m^{-3}	–
Lithium sulfide (Li_2S)	$1 \cdot 10^{-4}$			

Interfaces	Specific area (A_0)	Reactions	Forward rate	Reverse rate
Sulfur-Electrolyte	$1.0 \cdot 10^5$ m^2·m^{-3}	$S_8^{(solid)} \rightleftharpoons S_8^{(liquid)}$	$1.900 \cdot 10^{-2}$ m$^{-0.5}$·mol$^{0.5}$·s^{-1}	1 s^{-1}
Carbon-Electrolyte	$1.32 \cdot 10^5$ m^2·m^{-3}	$\tfrac{1}{2}\,S_8^{(liquid)} + e^- \rightleftharpoons \tfrac{1}{2}\,S_8^{2-}$	$7.725 \cdot 10^{13}$ m$^{-0.5}$·mol$^{0.5}$·s^{-1}	$2.940 \cdot 10^{-27}$ m$^{-0.5}$·mol$^{0.5}$·s^{-1}
		$\tfrac{3}{2}\,S_8^{2-} + e^- \rightleftharpoons 2\,S_6^{2-}$	$4.331 \cdot 10^{16}$ m·mol$^{-0.5}$·s^{-1}	$1.190 \cdot 10^{-23}$ m^4·mol^{-1}·s^{-1}
		$S_6^{2-} + e^- \rightleftharpoons \tfrac{3}{2}\,S_4^{2-}$	$3.193 \cdot 10^{14}$ s^{-1}	$4.191 \cdot 10^{-24}$ m·mol$^{-0.5}$·s^{-1}
		$\tfrac{1}{2}\,S_4^{2-} + e^- \rightleftharpoons S_2^{2-}$	$2.375 \cdot 10^{11}$ m$^{-0.5}$·mol$^{0.5}$·s^{-1}	$7.505 \cdot 10^{-24}$ s^{-1}
		$\tfrac{1}{2}\,S_2^{2-} + e^- \rightleftharpoons S^{2-}$	$4.655 \cdot 10^{12}$ m$^{-0.5}$·mol$^{0.5}$·s^{-1}	$4.738 \cdot 10^{-22}$ s^{-1}
Li_2S-Electrolyte	$1.0 \cdot 10^5$ m^2·m^{-3}	$2\,Li^+ + S^{2-} \rightleftharpoons Li_2S^{(solid)}$	$2.750 \cdot 10^{-5}$ m^6·mol^{-2}·s^{-1}	$8.250 \cdot 10^{-19}$ s^{-1}

Separator

Thickness	9 μm
Control volumes	1×5

Bulk phases	Volume fraction (ε_0)	Species
Electrolyte	1.0	See cathode

Anode

Thickness	100 μm
Control volumes	1×5

Bulk phases	Volume fraction (ε_0)	Species	Density / Inital concentration	Molar Gibbs energy
Lithium	0.63	Li	$5.34 \cdot 10^2$ kg·m^{-3}	0
Electrolyte	0.37	See cathode		

Interfaces	Specific area (A_0)	Reactions	Forward rate	Reverse rate
Lithium-Electrolyte	$1 \cdot 10^5$ m^2·m^{-3}	$Li \rightleftharpoons Li^+ + e^-$	$4.086 \cdot 10^{-9}$ m^{-5}·mol^{-2}·s^{-1}	1 m^{-2}·mol^2·s^{-1}

Table 9. Definition of parameters for the lithium-oxygen cell; converted from Andrei et al. [112]. Values are given for $T = 298.15$ K and $p = 101325$ Pa. Reverse reaction coefficients follow from thermodynamic consistency.

Cathode channel

	Length × Width	Value
Thickness	—	750 μm
Control volumes	1×1	1×35

Species	Initial concentration
O_2	$0.21\ \text{mol}\cdot\text{mol}^{-1}$
N_2	$0.79\ \text{mol}\cdot\text{mol}^{-1}$

Cathode

Control volumes: 1×5

Bulk phases	Volume fraction (ε_0)
Carbon	0.25
Electrolyte	0.75
Lithium peroxide (Li_2O_2)	0.0

Species	Molar Gibbs energy	Density / Inital concentration	Diffusion coefficient
C	0	$2.26\cdot10^{3}\ \text{kg}\cdot\text{m}^{-3}$	—
EC-EMC	—	$1.21\cdot10^{3}\ \text{kg}\cdot\text{m}^{-3}\ /\ 1.07\cdot10^{4}\ \text{mol}\cdot\text{m}^{-3}$	—
Li^+	0	$1.0\cdot10^{3}\ \text{mol}\cdot\text{m}^{-3}$	See [147]
PF_6^-	—	$1.0\cdot10^{3}\ \text{mol}\cdot\text{m}^{-3}$	See [147]
$O_2^{\text{(dissolved)}}$	−43 [127]	$1.62\ \text{mol}\cdot\text{m}^{-3}$	$7\cdot10^{-10}\ \text{m}^2\cdot\text{s}^{-1}$ [127]
Li_2O_2	−644	$2.14\cdot10^{3}\ \text{kg}\cdot\text{m}^{-3}$	—

Interfaces	Specific area (A_0)	Reactions	Forward rate
Carbon–Li_2O_2–Electrolyte	$8.66\cdot10^{7}\ \text{m}^2\cdot\text{m}^{-3}$	$2\,Li^+ + O_2^{\text{(dissolved)}} + 2\,e^- \rightleftarrows Li_2O_2$	$9.23\cdot10^{31}\ \text{m}^7\cdot\text{mol}^{-2}\cdot\text{s}^{-1}$
Carbon–Gas$^{\text{(cathode channel)}}$	—	$O_2^{\text{(gas)}} \rightleftarrows O_2^{\text{(dissolved)}}$	Assumed in equilibrium [127]

Separator

Thickness: 250 μm; Control volumes: 1×5

Bulk phases	Volume fraction (ε_0)	Species
Electrolyte	0.9	See cathode
Glass separator	0.1	—

Anode

Thickness: 0.01 μm; Control volumes: 1×1

Bulk phases	Volume fraction (ε_0)	Species	Molar Gibbs energy	Density / Inital concentration	Diffusion coefficient
Electrolyte	0.9				
Lithium	1.0	Li	0	$5.34\cdot10^{2}\ \text{kg}\cdot\text{m}^{-3}$	—

Interfaces	Specific area (A_0)	Reactions	Forward rate
Lithium–Electrolyte	$1\cdot10^{8}\ \text{m}^2\cdot\text{m}^{-3}$	$Li \rightleftarrows Li^+ + e^-$	$1.31\cdot10^{7}\ \text{m}\cdot\text{s}^{-1}$

LIST OF PUBLICATIONS

Reviewed papers

1) J. P. Neidhardt, D. N. Fronczek, T. Jahnke, T. Danner, B. Horstmann, and W. G. Bessler, "A Flexible Framework for Modeling Multiple Solid, Liquid and Gaseous Phases in Batteries and Fuel Cells," *Journal of the Electrochemical Society*, vol. 159, no. 9, p. A1528-A1542, 2012.

2) J. P. Neidhardt and W. G. Bessler, "Competition of electrochemical and thermochemical nickel oxidation in SOFC and SOEC electrodes: Thermodynamic analysis, modeling, and simulation," *Journal of Power Sources* (submitted)

Conference proceedings

1) J. Neidhardt, M. Henke, W.G. Bessler: "Kinetic modeling of nickel oxidation in SOFC anodes". SOFC XII – 219th ECS Meeting, Montreal, May 2011

2) J. P. Neidhardt, D. N. Fronczek, T. Jahnke, T. Danner, B. Horstmann, and W. G. Bessler, "A flexible modeling framework for multi-phase management in SOFCs and other electrochemical cells," in 10th European SOFC Forum (EFCF 2012), Lucerne, June 2012

3) J. P. Neidhardt and W. G. Bessler, "Oxidation of nickel in solid oxide fuel cell anodes: A 2D kinetic modeling approach," in 10th European SOFC Forum (EFCF 2012), Lucerne, June 2012

4) J.P. Neidhardt, V. Yurkiv and W.G. Bessler: "Spatiotemporal simulation of nickel oxide and carbon phases formation in solid oxide fuel cells (SOFC)". Fundamentals & Development of Fuel Cells Conference (FDFC 2013), Karlsruhe, April 2013

5) J. P. Neidhardt, R.J. Kee and W. G. Bessler, "Electrode reoxidation in solid-oxide cells: Detailed modeling of nickel oxide film growth," in 13th International Symposium on Solid Oxide Fuel Cells (SOFC-XIII), Okinawa, October 2013 (in prep.)

Conferences abstracts

1) J. Neidhardt and W.G. Bessler: "Spatially resolved modeling of nickel oxidation in SOFC anodes". 8th Symposium on Fuel Cell and Battery Modeling and Experimental Validation (ModVal 8), Bonn, April 2011

2) J. Neidhardt, V. Yurkiv, M. Henke, F. Leucht and W.G. Bessler: "Multi-scale modeling of solid oxide fuel cells: From patterned anodes to a hybrid power plant system". International Conference on Simulation Technology (SimTech 2011), Stuttgart, June 2011

3) J. P. Neidhardt, T. Jahnke, D. N. Fronczek, T. Danner, B. Horstmann, and W. G. Bessler, "A Flexible Framework for Modeling Multiple Solid, Liquid and Gaseous Phases in Batteries and Fuel Cells," 9th Symposium on Fuel Cell and Battery Modeling and Experimental Validation (ModVal 9), Campus Sursee, April 2012

4) V. Yurkiv, J. P. Neidhardt and W.G. Bessler: "Current-voltage behaviour of SOFCs considering anode degradation". 10th Symposium on Fuel Cell and Battery Modeling and Experimental Validation (ModVal 10), Bad Boll, March 2013

5) J. P. Neidhardt, V. Yurkiv and W.G. Bessler: "Prediction of secondary-phase formation and degradation in solid oxide fuel cell anodes". 2nd International Conference on Materials for Energy (EnMat II), Karlsruhe, May 2013

6) V. Yurkiv, J. P. Neidhardt and W.G. Bessler: "Modeling and Simulation the Influence of Solid Carbon and Nickel Oxide Formation on SOFC Performance and Degradation". Solid State Electrochemistry: Multiscale Modeling and Experimental Methods (SSE 2013), Heidelberg, July 2013

ACKNOWLEDGEMENTS

DECLARATION OF AUTHORSHIP

I hereby certify that the dissertation entitled

»Nickel oxidation in solid oxide cells: Modeling and simulation of multi-phase electrochemistry and multi-scale transport«

is entirely my own work except where otherwise indicated. Passages and ideas from other sources have been clearly indicated.

Ich versichere, dass ich die vorliegende Arbeit mit dem Titel

»Nickel oxidation in solid oxide cells: Modeling and simulation of multi-phase electrochemistry and multi-scale transport«

selbständig verfasst und keine anderen als die angegebenen Quellen und Hilfsmittel benutzt habe; aus fremden Quellen entnommene Passagen und Gedanken sind als solche kenntlich gemacht.

Name/Name: _____

Unterschrift/Signed: _____

Datum/Date: _____